Girum Yimer Yesuf

Influence of Subsoil Conditions on the Design and Performance of Flexible Pavements

Thesis for the degree of Philosophiae Doctor

Trondheim, September 2014

Norwegian University of Science and Technology
Faculty of Engineering Science and Technology
Department of Civil and Transport Engineering

NTNU – Trondheim
Norwegian University of
Science and Technology

NTNU
Norwegian University of Science and Technology

Thesis for the degree of Philosophiae Doctor

Faculty of Engineering Science and Technology
Department of Civil and Transport Engineering

ISBN 978-82-326-0450-0 (printed ver.)
ISBN 978-82-326-0451-7 (electronic ver.)
ISSN 1503-8181

Doctoral theses at NTNU, 2014:269

Printed by NTNU-trykk

The committee for the appraisal of this thesis comprised of the following members

Professor António Gomes Correia,
University of Minho, Portugal.

Associate professor Andrew Dawson,
University of Nottingham, United Kingdom.

Associate professor Helge Mork, (Administrator)
Norwegian University of Science and Technology, Norway.

Advisors during this study have been

Professor, Dr.-Ing. Inge Hoff, Department of Civil and Transport Engineering, Norwegian University of Science and Technology.

Professor, Dr.-Ing. Jan Vaslestad, Department of Mathematical Sciences and Technology, Norwegian University of Life Sciences.

Preface

This thesis is submitted to the Norwegian University of Science and Technology (NTNU) for partial fulfilment of the requirements for the degree of philosophiae doctor. This doctoral work has been carried out at the Department of Civil and Transport Engineering, NTNU, Trondheim, from August 2010 to July 2014.

This doctoral thesis is presented as a monograph. Additionally, four scientific publications were produced. Two papers were published on peer reviewed international conference proceedings, and two original journal manuscripts have been submitted.

Abstract

The effect of subsoil conditions is one of the prominent factors that control both the design and performance of flexible pavement structures. Despite having a wide range of empirical methods from measurements and experience, the quantification of the short-term and long-term physical processes of geo-materials in roads is not yet fully understood. Particularly, subgrade soils have not got the required attention in the characterization of pavement materials although they are known as the "foundation" of the pavement structure. This conception has raised — partly due to the notion that the stress from the traffic is low at the subgrade level — and partly, due to existence of a wide variety of soils, in contrast to standardized materials for asphalt, base, and sub-base layers. Low-traffic volume roads, however, have often thin asphalt layer, and the stress magnitude from the traffic loads can be significant at the subgrade level. In addition, subgrade soils are most susceptible to the variation of local and environmental conditions.

With the fact that the subgrade layer is an integral part of pavement analysis, this thesis aimed to address the main important issues of characterization of subgrade soils in mechanistic pavement design methods. The objectives of this research have been classified within three main themes: (1) to propose numerical models to characterise subgrade soils for practical mechanistic-empirical pavement design method, (2) to enhance the quantitative characterisation of subgrade soils — instead of the widely used qualitative characterizations in practice, (3) to use finite element method to optimise road design and maintenance practices.

The main contributions of this study are: *First*, an overview of research literature is provided on the existing methods and knowledge of characterization of subgrade soils in flexible pavement design. The geotechnical aspects in pavement design are outlined to identify the research needs and to formulate the main research questions. *Second*, a method for formulation and implementation of a nonlinear resilient modulus model is presented. The method in this study has been found to be more versatile than the existing methods for characterization of subgrade soils since it considers the effects of both confining pressure and deviator stress. The implications of this method were found to be important aspects of pavement design for low-traffic volume roads.

Third, a constitutive model is proposed to predict the long-term deformation of subgrade soils. The model is formulated based on the plastic strain from first loading cycle, and an additional parameter that accounts for the proximity of the applied stress to the static strength of the soil. The predicted results from the proposed model showed a good agreement with laboratory tests for deviator stress level up to 50% of the static strength of the soil. *Fourth*, based on finite element modelling of soil compaction, the lift thickness of fine-grained soils has been observed to be defined as a function of cohesion and friction angle. This study suggested the optimisation technique of lift thickness depending on the strength parameters of soils to improve the rolling strategy of soil compaction during road construction.

Finally, a finite element modelling technique is presented for prediction of spring thawing in frozen subgrade soils. Since there are no well-established methods for modelling of the thawing process, analytical solutions are used to validate the numerical methods for simplified boundary conditions. Further, the application of finite element method is extended to model multi-layer pavement structures with the thermal and physical properties of each layer and varying surface temperature. In this study, the thaw depth is observed to be linearly proportional to time for sinusoidal surface temperature variation — in contrast to the existing knowledge of thaw rate for homogeneous frozen layers where the thaw depth is proportional to the square root of time.

Acknowledgements

This thesis has enormously benefited from the support of several people from the conception of research project to its end. My journey as a PhD candidate has not only enriched my academic endeavour and research aspirations but also gave me the opportunity to know many individuals both professionally and personally. Nonetheless, this could not be possible without the research fund from the Norwegian Public Roads Administration (NPRA). I greatly acknowledge the financial support that I got from the "Varige veger" project at NPRA.

Next, I want to acknowledge my main supervisor Professor Inge Hoff. He was generous with time to have discussions from the start to the end of this research. I have been able to explore many interesting aspects of this research project under his guidance. Professor Hoff's constant support and confidence in my work have been vital for my success during my PhD study. His careful critique and commentary on my writings were crucial to the accomplishment of this work.

I would like to extend my deepest gratitude to my co-supervisor Professor Jan Vaslestad. I am grateful to know him as a colleague at NPRA Region East before I started my PhD study, and I have been able to collaborate with him and learnt a lot from his expertise. His academic and professional advice has always been inspirational. Professor Vaslestad was so keen to involve actively in the meetings and discussions which have tremendously helped me to see the success story of my research.

My stay (from August 2011 to October 2011) at Norwegian Public Roads Administration—*vegdirektoratet* in Trondheim gave me an in-depth understanding of the Norwegian practice of pavement design and performance evaluation. I want to thank all at the "vegteknologi" section for their kind hospitality. Leif Bakløkk, Dr.-Ing. Jostein Aksnes and Dr.-Ing. Rabbira Garba have actively involved in the research team for my project and gave me valuable comments in the first two years of my research work.

I would like to thank fellow PhD candidates and postdocs at the department of Civil and Transport Engineering with whom I had the opportunity to discuss the "PhD experience" and the unwritten rules in research life. Sara Anastasio, Ute Ehlers, and Anne Nuijten have always been cheerful for the progress of my

research. Anne Lalagüe helped me with French translation of the abstract for my first publication during my PhD study. Dr. Elena Kuznetsova has given me valuable feedback on Chapter 2 (section 2.3.2) and Chapter 6.

I owe my deepest gratitude to my wife, Hayat, for her love, care and support. She is the most wonderful person who came into my life. Her understanding and encouragement has made this work possible. Lastly, but not least, I thank my mom, dad, and siblings for their love and moral support.

List of symbols and abbreviations

Symbols

Notations		Definitions
c	:	Cohesion
C_c	:	Compression index
C_s	:	Swelling index
c_u, c_f	:	Volumetric heat capacity of the unfrozen and frozen soil respectively
c_s, c_w	:	Specific heat of the soil grains and water respectively
d	:	Cohesion value in Drucker-Prager Cap model in Abaqus
D_{ijkl}	:	Stiffness matrix
e	:	Mathematical constant ≈ 2.71828
e	:	Void ratio
erf	:	Error function
E	:	Young's modulus
f	:	Yield function
g	:	Plastic potential
I_1, I_2, I_3	:	Principal invariants of a tensor
J_2, J_3	:	Stress deviator invariants
K	:	Bulk modulus
k_u, k_f	:	Thermal conductivity of the unfrozen and frozen soil respectively
L	:	Latent heat of fusion
M_R	:	Resilient modulus
M	:	Ratio of yield stress in triaxial tension to triaxial compression
N	:	Number of traffic load repetitions (loading cycle)
p	:	Mean stress
p_a	:	Evolution parameter
p_a	:	Atmospheric pressure
q_*	:	Internal variable
q	:	Deviator stress
q_s	:	Static strength of the soil

R	:	A coefficient to define the Drucker-Prager Cap model yield surface in Abaqus
r	:	Third stress invariant
s_u	:	Undrained shear strength
Ste	:	Stefan number
T	:	Temperature
w	:	Water content (in percentage)

Greek letters

Notations		Definitions
σ_{ij}	:	Stress tensor
ε_{kl}	:	Strain tensor
ε_{p1}	:	Permanent strain in the axial direction
σ_d	:	Deviator stress
σ_{oct}	:	Octahedral normal stress
τ_{oct}	:	Octahedral shear stress
ν	:	Poisson's ratio
$\bar{\varepsilon}^p$	:	Accumulated effective plastic strain
ϕ	:	Friction angle
ψ	:	Dilation angle
β	:	Measure of friction angle for Drucker-Prager Cap model in Abaqus
η	:	Fiction angle measure for Drucker-Prager model
ξ	:	Cohesion multiplier for Drucker-Prager model
ρ	:	Density of a material
ρ_d	:	Dry density
α	:	A coefficient to define the Drucker-Prager Cap model yield surface
κ_u,κ_f	:	Thermal diffusivity
λ	:	A constant to define the rate of thawing
$d\lambda$	:	Plastic strain multiplier

Subscripts and superscripts

Notations		Definitions
e	:	Elastic
ep	:	Elastoplastic
f	:	Frozen
g	:	Ground
oct	:	Octahedral
i,j,k,l	:	Indexes in continuum mechanics
p	:	Plastic
s	:	Surface
u	:	Unfrozen
vol	:	Volumetric

Operations

Notations		Definitions
tr	:	Trace of a matrix
$\mathrm{A} \cdot \mathrm{B}$	:	Dot product of two tensors A and B
$\mathrm{A} \times \mathrm{B}$	:	Cross product of two tensors A and B
$\mathrm{A} \otimes \mathrm{B}$	:	Dyadic product of two tensors A and B
$sgn(x)$	:	Sign of a real number x
I	:	Identity matrix or unit matrix

Acronyms

AADT	:	Average Annual Daily Traffic
AASHTO	:	American Association of State Highway and Transportation Officials
AASHO	:	American Association of State Highway Officials
AC	:	Asphalt concrete
ASTM	:	American Society for Testing and Materials
CBR	:	California Bearing Ratio
CCC	:	Continuous Compaction Control
DCP	:	Dynamic Cone Penetrometer

FEM	:	Finite Element Method
FWD	:	Falling Weight Deflectometer
HMA	:	Hot mix asphalt
IC	:	Intelligent Compaction
IRI	:	International Roughness Index
NDT	:	Non-Destructive Testing
NTNU	:	Norwegian University of Science and Technology
NVDB	:	Nasjonal veg data bank (National Road Data Bank)
NPRA	:	Norwegian Public Roads Administration
PI	:	Plasticity Index
PLT	:	Plate Load Testing
PMS	:	Pavement Management System
SMA	:	Stone mastic asphalt
UMAT	:	User material (subroutine)

Table of contents

Preface ii

Abstract iii

Acknowledgements v

List of symbols and abbreviations vii

Table of contents xi

List of Figures xiv

List of Tables xviii

1 Introduction 1

1.1 Background 1
1.2 Motivation 4
1.3 Problem statement 5
1.4 Contributions of the research work 7
1.5 Scope and outline of the thesis 8
1.6 Publications 9

2 Literature review 11

2.1 Pavement design 11
2.1.1 Empirical pavement design method 15
2.1.2 Mechanistic-empirical design method 18
2.1.3 Finite element method 22
2.2 Pavement performance 23
2.2.1 Rutting 24
2.2.2 Cracking 27
2.2.3 Roughness 29
2.2.4 Surface friction 31
2.3 Bearing capacity 31
2.3.1 Compaction 32
2.3.2 Climatic factors 36
2.4 Behaviour of fine-grained soils under repeated loading 41
2.4.1 Resilient modulus 41
2.4.2 Permanent deformation 50
2.4.3 Permanent deformation models 51

2.4.4 Factors affecting permanent deformation 54
2.5 Chapter summary 57

3 Numerical implementation of nonlinear resilient modulus model 59

3.1 Stresses and strains in pavements 59
3.2 Finite element method (FEM) 60
3.3 Nonlinear resilient modulus of subgrade soil 61
3.3.1 Formulation of nonlinear numerical model 61
3.3.2 Determination of parameters 67
3.3.3 Numerical implementation, results and discussions 69
3.4 Chapter summary 76

4 Modelling of permanent deformation of subgrade soils 77

4.1 Deformation of subgrade soils 77
4.2 Formulation of the model 79
4.2.1 Determination of parameters 84
4.2.2 Numerical implementation 84
4.2.3 Deformation from the first load application 87
4.2.4 Repeated loading 90
4.3 Results and discussions 91
4.4 Chapter summary 97

5 Optimisation of effective depth of compaction of subgrade soils 99

5.1 Compaction of fine-grained soils 99
5.2 Finite element modelling 101
5.2.1 The soil model/Drucker-Prager Cap model 101
5.2.2 Geometric modelling 106
5.3 Results and discussions 108
5.4 Chapter summary 117

6 Prediction of thawing process in frozen subgrade soils 119

6.1 Spring thawing 119
6.2 Analytical solutions for thawing process 121
6.2.1 Thawing rate 121
6.2.2 Excess pore-water pressure 124
6.2.3 Limitation of analytical solutions 125
6.3 Finite element analysis 126
6.4 Thawing of homogeneous frozen layer 128
6.4.1 Analytical solution versus uncoupled finite element analysis 128
6.4.2 Analytical solution and finite element coupled analysis 131
6.4.3 Excess pore-water pressure 137

6.4.4 Weather data and thermal properties of pavement layers 141
6.4.5 Coupled finite element analysis for multi-layer system 143
6.5 Chapter summary 145

7 Conclusions and recommendations for future work 147

7.1 Conclusions on the research method 148
7.2 Conclusions on the specific research contributions 148
7.2.1 Nonlinear resilient modulus of subgrade soils 148
7.2.2 Long-term permanent deformation of subgrade soils 149
7.2.3 Effective depth of compaction of fine-grained soils 150
7.2.4 Thaw prediction in frozen subgrade soils 150
7.3 Recommendations for future work 151
7.4 Final remarks 152

References 153

Appendix A 166

Appendix B 171

List of Figures

Figure 2.1: Principles of flexible pavement design in Norway (a typical road section). Adapted from NPRA [84]..... 12
Figure 2.2: Design factors that affect pavement design. 13
Figure 2.3: Critical strain locations in a flexible pavement. 19
Figure 2.4: Relationship between rut depth and vertical elastic strain. Adapted from Odermatt *et al.* [85]..... 19
Figure 2.5: Methodology of mechanistic procedure for flexible pavement design. Adapted from Huang [49] (*Chapter 11, p. 473*) 21
Figure 2.6: Surface rutting with high degree of severity [81]. 25
Figure 2.7: a) Longitudinal cracking with medium degree of severity, and b) transverse cracking with high degree of severity [81]. 28
Figure 2.8: Fatigue cracking with high degree of severity [81]. 28
Figure 2.9: IRI roughness scale [101]..... 30
Figure 2.10: Relationship between dry density and water content in soils. Adapted from Holtz & Kovacs [46](*Chapter 5, p. 116*)..... 34
Figure 2.11: Effect of compaction effort on the compaction curve. Adapted from Lambe (1958a) as cited in Holtz & Kovacs [46] (*Chapter 5, p. 118*). 35
Figure 2.12: Amount of water remaining unfrozen water for various frozen soils. Adapted from Williams & Smith [114] (*Chapter 1, p. 7*)..... 37
Figure 2.13: Freezing sequence in a typical pavement profile, adapted from Kavanaugh [55]. Note that thickness of the layers is not to scale..... 38
Figure 2.14: Mechanism of thaw weakening [103]..... 40
Figure 2.15: Illustration of generalized stress dependent secant stiffness of soil... 42
Figure 2.16: Illustration of stress dependent resilient modulus for subgrade soils. 42
Figure 2.17: Octahedral planes in a principal coordinate system. 45
Figure 2.18: Illustration of constant compactive effort and constant dry density. Adapted based on the descriptions by Li & Selig [64]..... 46
Figure 2.19: Relation between resilient modulus and moisture content a) constant dry density, and b) constant compactive effort [64]. 47
Figure 2.20: Resilient modulus test results a) A-6 [AASHTO classification] soil b) A-7-6 [AASHTO classification] and A-6 soils [117]. 49
Figure 2.21: Effect of resilient modulus on loading frequency. Adapted from Horvli [47]. 50

Figure 2.22: Apparent shakedown envelope for compacted A-6 [AASHTO classification] cohesive soil under repeated loading. Adapted from Muhanna *et al.* [72]. 55
Figure 2.23: Effect of loading frequency on permanent deformation at 0.1Hz and 10Hz on Lade clay soils. Adapted from Horvli [47]. 56
Figure 3.1: Iterations to converge at each incremental stress. 63
Figure 3.2: Loading on a single axisymmetric element. 70
Figure 3.3: Comparison of linear and nonlinear subgrade stiffness. 71
Figure 3.4: Axisymmetric multi-layer geometry. 72
Figure 3.5: Response of low-traffic volume road section (AC thickness=40mm): a) vertical elastic strain distribution, b) vertical stress distribution, c) vertical elastic strain distribution, and d) vertical stress distribution. 74
Figure 3.6: Response of high-traffic volume road section (AC thickness=150mm): a) vertical elastic strain distribution, b) vertical stress distribution, c) vertical elastic strain distribution, and d) vertical stress distribution. 75
Figure 4.1: the Drucker-Prager yield surface in principal stress space. Adapted from Nordal [80]. 82
Figure 4.2: Alternative Drucker-Prager surfaces compared to Mohr-Coulomb. Adapted from Nordal [80]. 82
Figure 4.3: Determination cohesion and friction angle from conventional triaxial test. 84
Figure 4.4: Schematic presentation of the proposed constitutive model. 86
Figure 4.5: Geometric interpretation of return mapping scheme for hardening plasticity. Adapted from de-Souza-Neto *et al.* [31] (*Chapter 7, p. 197*) 88
Figure 4.6: Concept of repeated load applications assumed in this study. 91
Figure 4.7: Comparison of the proposed model in this study with test results reported in Li & Selig [65] for soil type $\rho d = 1440$ kg/m^3, $w = 28.7\%$, $qs = 159$kPa. 92
Figure 4.8: Change of soil parameters with water content. a) cohesion, and b) friction angle. Adapted from Ying *et al.* [122]. 94
Figure 4.9: Comparison of the proposed model in this study with test results reported in Li & Selig [65] for soil type $\rho d = 1470$ kg/m^3, $w = 27.6\%$, $qs = 193$kPa. 95
Figure 4.10: Effect of confining pressure on the accumulation of plastic strain at a deviator stress of 73.1kPa. 96

Figure 5.1: Principle of an approximate method for determining a lift thickness to achieve a minimum compacted relative density. Adapted from Dappolonia et al., as cited in Holtz & Kovacs [46] (*Chapter 5, p. 139*). 100
Figure 5.2: Typical yield surfaces of the Cap model in the deviatoric stress plane. Adapted from Abaqus FEA [104]. 103
Figure 5.3: Density dependent Drucker-Prager Cap model. Adapted from Abaqus FEA[104]. 103
Figure 5.4: Modified Drucker-Prager/Cap model: flow potential in the $p - t$ place. Adapted from Abaqus FEA [104]. 105
Figure 5.5: Isotropic consolidation test to determine hardening parameters. 106
Figure 5.6: Geometric model of the soil and roller. 107
Figure 5.7: View of compaction profile. 110
Figure 5.8: Stress components induced due to the load from the rolling roller at a depth of 7.5cm from the surface for a roller weight of 140kN. 110
Figure 5.9: a) pressure (or mean stress)(p) and shear stress (τ) at a depth of 7.5cm from the surface for a roller weight of 140kN, and b) the corresponding change of density. 111
Figure 5.10: Stress paths and evolution of the cap surface. 112
Figure 5.11: Compaction density profile for different weight of roller. 113
Figure 5.12: The effect of friction angle on soil compaction. 114
Figure 5.13: Effective compaction depth at different relative densities based on friction angle. 115
Figure 5.14: The effect of cohesion on soil compaction. 116
Figure 5.15: Effective compaction depth at different relative densities based on cohesion 116
Figure 6.1: Conceptual pavement stiffness variations due to freezing and thawing. Adapted from Erlingsson & Salour [37]. 120
Figure 6.2: The Neumann problem. Adapted from Nixon & McRoberts [78]. 122
Figure 6.3: Comparison of different solution methods at Tg= 0℃. 124
Figure 6.4: Specific heat, latent heat definition. Adapted from Abaqus FEA [104]. 127
Figure 6.5: Finite element mesh for one-dimensional thawing of a frozen soil layer. 129
Figure 6.6: Temperature distribution in one-dimensional thawing at different time steps (NT: Nodal temperature). 130
Figure 6.7: Comparison of analytical heat transfer analysis with FEM. Note that the FEM is this case is only heat transfer (uncoupled) analysis. 131

Figure 6.8: Finite element model: boundary conditions and predefined variables for the coupled analysis. Note that the geometric dimensions and meshes are similar to Figure 6.5. 136
Figure 6.9: Comparison of analytical solution (Neumann's solution at Tg = 0°C) with finite element analysis. 137
Figure 6.10: Pore-water pressure generated during thawing at a depth of 0.5m from surface using coupled analysis in Abaqus..... 139
Figure 6.11: Field measurements of excess pore-water pressure during the Vormsund test road project. Adapted from Nordal & Hansen [79] (p. 34). 139
Figure 6.12: Unfrozen volumetric moisture content in the subgrade soil (AASHTO soil classification: A-2-4), measured at a depth of 584mm from the pavement surface. Adapted from Janoo & Shepherd [52]. 140
Figure 6.13: Varying surface temperature from actual weather data for the coupled finite element analysis. 141
Figure 6.14: Finite element model with thermal and boundary conditions similar to a typical in situ pavement section..... 143
Figure 6.15: Rate of thawing of the frozen subgrade for field conditions. 145

List of Tables

Table 2.1: Examples of assumptions used to describe different design parameters. 14
Table 2.2: Classification of frost susceptibility [84]..... 17
Table 2.3: Bearing capacity classification of the subgrade layer [84]..... 17
Table 2.4: Different modes of rutting based on the descriptions presented in Dawson & Kolisoja [29]. 25
Table 2.5: Maximum allowable rut depth at network and sectional level in Norway [83]..... 27
Table 2.6: Maximum allowable rut depth and roughness at network level. 30
Table 2.7: Resilient modulus models for subgrade soils. 44
Table 3.1: Comparison of the pavement response on the top of subgrade for linear elastic and nonlinear elastic analyses..... 73
Table 4.1: Input parameters..... 92
Table 4.2: Input parameters..... 95
Table 5.1: Assumed input parameters for the Cap model. 109
Table 6.1: Assumed input data for analytical solution and uncoupled finite element analysis. 129
Table 6.2: Input parameters the coupled finite element analysis and analytical solution. 134
Table 6.3: Additional input parameters for coupled analysis in Abaqus. 135
Table 6.4: Input parameters for analytical solution and FEM. 138
Table 6.5: Excess pore-water pressure obtained from analytical solution..... 138
Table 6.6: Input parameters for varying surface temperature. 142
Table 6.7: Element type used in finite element analysis. 144
Table 6.8: Thermal input parameters for asphalt and aggregates. 144

Chapter 1

Introduction

This chapter introduces the general background, objectives and outline of the research work. The first section comprises a concise review of the historical development of road design. The motivation of this research is discussed in section 1.2. Section 1.3 describes the problem statement of the research, and the specific research questions are defined. The contributions of this research work will be summarised in section 1.4. Section 1.5 discusses the outline of this thesis, and the last section presents a list of scientific publications produced during the PhD study.

1.1 Background

Thousands of years ago, roads began to play a central role in the history of human civilization. Stone-paved streets were built in Ur in the Middle East and corduroy[1] roads had been constructed in Glastonbury in England as early as 4000 BC [60](*Chapter 3, p. 43*). The system of roads, built during the period of the Roman Empire, was the first recorded account of the construction of a network of roadways in human history. The success of building roads during the Roman era was achieved due to the notion of drainage. The importance of drainage has never been compromised since then. However, a better understanding of the properties of pavement materials led to a more efficient and economical design. Prior to the early 1920s, the thickness of pavement was purely based on experience and the same thickness of road section was used regardless of the type of subgrade soils

[1] Corduroy roads are roads on swampy ground, often made of logs laid transversely.

[49]. The empirical methods had then been improved to account for the effect of subgrade soils using soil classification methods and strength tests, mainly California Bearing Ratio (CBR) test. In recent years, the notion how to build roads has gone from fully empirical approach to semi-analytical methods in some countries.

The demand for a better design method has been increasing since the innovation of motor vehicles. It was the "AASHO road test" conducted by the American Association of State Highway and Officials (AASHO) in the late 1950s on flexible and rigid pavements in Ottawa, Illinois that boosted the knowledge of pavement design. The experience and results obtained from the AASHO road test were used to develop empirical design equations used in the American Association of State Highway and Transportation Officials (AASHTO) Guide for the Design of Pavement Structures [1]. Since then, emphasis was given on standardising test equipment and procedures, and controlling the quality of road materials. Consequently, many countries have adopted the AASHTO pavement design manual with some modifications to their local conditions. Likewise, the first comprehensive road test in Norway was the "Vormsund test road" in which a full scale test was done from 1958 to 1968. The test was primarily carried out to study frost action in the subgrade soils, providing a fundamental platform for the Norwegian pavement design practice. Nordal & Hansen [79] reported some of the results from the Vormsund test road.

The Norwegian pavement design manual [84] consists of three levels of design guidelines. The first method (Level 1) is an empirical method, based on index values and fixed load distribution coefficients of pavement layers, which are available in the design manual. In this method, the thickness of the asphalt and base layers are determined from the traffic data while the thickness of sub-base (or frost protection) layer is designed based on the bearing capacity index of the subgrade soils and traffic data. The second design method (Level 2) is similar to Level 1, except the load distribution coefficients of pavement layers are obtained from field and laboratory tests. The third one (Level 3), which is not implemented in the design code, is the mechanistic-empirical pavement design method.

The mechanistic view of design philosophy is relatively new in the mainstream pavement design practice. Some mechanistic pavement design programs have been developed using the elastic behaviour of the pavement materials for routine

pavement design (e.g. MMOPP[111] in Denmark, PMS-Objekt[113] in Sweden). Some pavement analysis programs have been developed based on finite element method (FEM) (e.g. DARWin-ME[3], ILLI-PAVE [109], MICH-PAVE [40]). General purpose finite element programs (such as Abaqus FEA, ANSYS) are used for advanced modelling techniques of pavements. However, the use of advanced finite element programs is mostly limited to research.

Pavement materials exhibit different kinds of behaviour. In modelling of materials in flexible pavements, two major categories exist: the bound and unbound layers. Among the bound layers, asphalt concrete shows rate dependency and creep behaviour, and the viscous behaviour is accounted in the constitutive models. For the unbound layers, i.e. subgrade and aggregates, elasto-plastic models are commonly used to formulate the load associated deformation. The behaviour of fine-grained soils such as silt and clay is highly affected by the amount water in soil pores. Particularly, subgrade soils are mostly prone to moisture variation in pavements. A slight change in the level of moisture in the subgrade soils is determinant on the overall behaviour, both on the stiffness and deformation properties. So, the characterization of subgrade soils must comprise both load-related and environmental factors. The theoretical aspects of pavement design calculated using mechanics are crucial, but do not stand alone to design pavements realistically. They should be combined with the empirical experience for a better understanding of the pavement materials. In the implementation of a mechanistic-empirical pavement design approach, substantial knowledge about pavement materials should be accumulated.

The structural and functional performances of flexible pavement sections are highly dependent on the subsoil conditions. When the subgrade soil and the overlying layers provide adequate support for the traffic loads, the pavement gives satisfactory service in the design period. In evaluation of pavement performance, different indexes are used to describe the extent of distresses, such as cracking, rutting, and roughness. The permanent deformation from one load repetition is very small. However, the gradual accumulation of plastic strains for a large number of load repetitions results in excessive rutting — a consequent failure of the pavement structure. It has been practically observed that a distressed pavement is often due to a combination of different factors, rather than just one cause. Yet, rutting is considered as one of the most critical parameters that strongly affect the pavement performance. Other distresses such as cracking and roughness are often associated to rutting.

1.2 Motivation

The knowledge of soil mechanics is profound, both empirically and analytically. Despite tremendous challenges on the characterization of real soil behaviour, the advent of new modelling techniques such as the finite element method (FEM) and finite difference method (FDM) enables an in-depth study on deformation and failure mechanisms of different soils. Moreover, coupled analysis methods provide to a more reliable prediction on the behaviour of soils at different conditions.

Unlike in the mainstream geotechnical engineering, geotechnical aspects in pavement engineering has not benefited from the state-of-the-art/practice of soil characterization. The application of soil mechanics principles to design of pavement foundations has lagged some way behind the knowledge accumulated through research [16]. Some of the factors that contribute to the limitation of application of geotechnical knowledge in pavement engineering in practice are:

- The magnitude of stress from traffic loading is highly reduced at the subgrade level. More emphasis is usually given to the asphalt and base-course layers. However, subgrade soils often have weak strength so that even a small magnitude of stress may cause substantial deformation. Especially, low-traffic volume roads are designed with thin asphalt layer, and the stress at the subgrade level may increase the degree of mobilization in subgrade soils.
- The performance of subgrade soils is controlled by many factors such as the type of soil, level of compaction, equilibrium moisture content and drainage. To formulate a constitutive relationship comprising all these factors is a difficult task. In addition, subgrade soils vary greatly so that the scope of soil investigation and testing plan may not consider the actual ground condition at a specific road section.
- The failure mechanism of subgrade soils is complicated. Conventional rate-independent elasto-plastic soil models are applied only for monotonic loading. In contrast, the accumulation of plastic strains is due to many loading cycles (thousands to millions of load repetitions). In the mainstream geotechnics, there are new developments of the modeling aspects of cyclic loading. However, these models are effective for few loading cycles and are not realistic for pavement design.

Despite the limitations mentioned above, innovation of new testing methods and availability of design and analysis programs on personal computers have led road engineers to new ideas and design approaches. In order to adopt the new methods, we need a fundamental understanding of their merits and limitations. Besides, various factors associated to the methods must be well known and assimilated in the research community and industry. In this way, the "research only" methods can be implemented in practice.

1.3 Problem statement

The main aim of this research is to present characterization of subgrade soils in flexible pavements. FEM is used to model different subgrade conditions for load-related and environmental factors. A comparative view of the methods and results obtained in this research with the existing knowledge and practice is discussed in the subsequent chapters. The overall perspective of this study broadly consists of three points, namely mechanistic pavement design methods, qualitative and quantitative characterization of pavement materials and use of FEM for optimization techniques based on soil parameters.

Towards mechanistic pavement design methods:

The mechanistic-empirical pavement design method is gaining popularity in the last few decades. Some countries have developed their own mechanistic-empirical program based on their own design code. Linear elastic material model is often used for the subgrade layer to analyse the critical strains. Nonetheless, experimental tests have clearly shown the nonlinear behaviour of resilient modulus of subgrade soils. A generalized model that accounts for the nonlinear behaviour of materials is vital for reliable analysis of the actual pavement response. In addition to the critical strains, rutting models are relevant to account for the long-term performance in mechanistic models. The existing rutting models are empirical. Hence, mechanistic rutting models based on relevant soil parameters must be developed.

From qualitative to quantitative characterization:

The characterization of pavement materials is widely empirical. A qualitative expression is often used. For example, the types of soils which are frost

susceptible are known, but the quantitative description of the physical phenomenon is not well described. The bearing capacity range of subgrade soils is distinctly outlined. However, the deformation properties are not explicitly presented in existing empirical methods. With the development of material and performance prediction models, the extent of influence of individual design parameters should be studied.

Use of FEM for analysis and optimization techniques:

A considerable improvement of finite element modelling techniques has undergone over the last few years. This includes advanced constitutive material models, advanced soil-structure interaction modelling and coupled analysis. By using a proper material model and boundary conditions, full scale field conditions can be modelled using numerical methods. Therefore, the effect of material parameters and different boundary conditions are used to optimize the design and performance of pavements.

Specific research questions

- The mechanistic-empirical pavement design method considers strain criteria to determine the thickness of pavement layers. The method requires the stiffness of each layer. *How does the strength of subgrade soils control the overall pavement response?* The stiffness of unbound layers depends on the stress level. The stress level on the subgrade is small and the response is often assumed to be linear elastic. *Is there a significant effect on the design requirements due to the nonlinear behaviour of subgrade soils?*
- The measured rut at the surface of flexible pavements is due to permanent deformations of the asphalt layer, base and sub-base course, and subgrade. The existing models for rut prediction of subgrade soils are entirely empirical. *How can we use the framework of elasto-plasticity for prediction of plastic strain associated to the repeated loadings from the traffic?*
- Compaction is an important step during construction of roads to strengthen the bearing capacity of road foundation. Conventionally, a

"lift thickness[2]" is specified by the road authorities. This lift thickness is generally based on experience. The level of compaction of subgrade soils is dependent on the "conditions" of the soils, for instance the moisture level at the time of compaction. The overall behaviour of the soil, in this case is represented by the well-known soil parameters such as the "cohesion" and "friction angle". *How can we optimise the effective depth of compaction and rolling strategies as a function of the soil parameters?*

- In the thawing mechanism of frozen subgrade soils, accumulated knowledge is available based on experimental studies. The analytical solutions consider only a step increment of temperature. In reality, the change of surface temperature is gradual. *What would be the rate of thawing in frozen subgrade soils if we include the daily variation of surface temperature and the thermal behaviour of pavement layers?* The solution can be obtained from coupled analysis of thermal–consolidation analysis in a full scale finite element model.

1.4 Contributions of the research work

The findings of this research work have been reported in publications. The summary of contributions from this study is presented as follows:

- The effect on nonlinear resilient modulus of subgrade soils on pavement design is presented. A constitutive model that accounts the effect of nonlinear behaviour of subgrade soils is implemented in user material subroutine (UMAT) in Abaqus FEA. (Yesuf [120])
- A constitutive model is proposed to predict the accumulation of permanent strains for subgrade soils. The deformation from the first loading cycle is incorporated in the elasto-plastic theoretical framework based on the Drucker-Prager yield criterion. The proximity of the deviator stress to the static strength of the subgrade soil is considered to predict the amount of incremental plastic strains at each loading cycle. The model has been implemented in UMAT and the validation of the model with test results available in the literature is presented. (Yesuf & Hoff [121])

[2] Lift thickness is a technical term used to describe the thickness of the layer required to achieve the target compaction density.

- A numerical analysis is presented to optimize the "lift thickness" during compaction of fine-grained soils. The existing field compaction methods consider the same lift thickness for a range of fine-grained soils. In this study, it is presented that the actual "lift thickness" varies based on the cohesion and friction angle of the soil. Hence, the rolling strategy can be adjusted and the compaction practice can be improved. (Yesuf *et al.* [118])
- A numerical modelling technique for the thawing process of frozen subgrade soils is presented. Thermal boundary conditions are included in the model to simulate the actual variation of surface temperature. Based on the method presented in this study, the spring thawing period can be predicted more accurately than the existing methods. This approach helps to optimize road management and maintenance strategies in cold climate regions.(Yesuf *et al.* [119])

The commercial finite element software, Abaqus FEA, has been used for analysis and modelling. For simulation of the compaction process and the coupled analysis of the thawing process, the commercially available material models in the software package are used. For the analysis nonlinear resilient modulus and permanent deformation, user material subroutines are written using FORTRAN programming language.

1.5 Scope and outline of the thesis

Design and performance prediction of flexible pavements require the characterization of all pavement layers. The scope of this study is mainly to present the geotechnical aspects of fine-grained soils for pavement design and long-term performance. Finite element modelling techniques are adopted as the main research method. FEM is used to evaluate different conditions in pavements such as stress stress-strain analysis, nonlinear behaviour, coupled analysis, and user-defined rutting models. For the required input data in the numerical analysis, relevant literature is referred.

This thesis is organized into seven chapters. The remainder of Chapter 1 focuses on the overview of each chapter and list of publications. Chapter 2 deals with the literature review of the research project with the emphasis on the geotechnical aspects of subgrade soils in flexible pavement design. Chapter 3 discusses the

numerical implementation of nonlinear resilient modulus model. Furthermore, the practical implications of nonlinear behaviour of subgrade soils in pavement design are presented.

Chapter 4 is devoted to the development of a constitutive model to predict the accumulated permanent strains in subgrade soils. The validation of the model is presented using experimental results available in the literature. Chapter 5 presents the optimisation techniques of effective depth of soil compaction. In Chapter 6, analytical and numerical methods are used to model the thawing process and development of excess pore-water pressure in subgrade soils. The last chapter, Chapter 7, contains conclusions and suggestions for further research. The appendices present an additional note and published papers.

1.6 Publications

During this PhD study, two conference papers were published on peer-reviewed conference proceedings, and two journal papers have been submitted. The list of publications is shown below:

1. Yesuf, G.Y., I. Hoff, and J. Vaslestad (2013) Development of excess pore-water pressure in thawing process of frozen subgrade soils: Based on analytical solutions and finite element method. *Proceedings of the 18th International Conference on Soil Mechanics and Geotechnical Engineering,* September 2-6, 2013, Paris, France, Page 857-860.
2. Yesuf, G.Y., I. Hoff, and J. Vaslestad (2013) Optimization of Effective Depth of Compaction for Fine-Grained Soils. *Proceedings of the 3rd International Conference – GEOMATE 2013 Geotechnique, Construction materials and Environment,* November 13-15 2013, Nagoya, Japan, Page 333-338.
3. Yesuf, G.Y. and I. Hoff (2014) Finite Element Modelling for Prediction of Permanent Deformation of Subgrade Soils. *Road Materials and Pavement Design*, (under peer review).
4. Yesuf, G.Y. (2014) Implications of Nonlinear Behaviour of Subgrade Soils in Flexible Pavement Design. *International Journal of Pavement Engineering* (Submitted).

Chapter 2

Literature review

In this chapter, the fundamental characterizations of subgrade soils in flexible pavement design are presented. The existing and current practices of analysis and design methods are thoroughly explained. The first section discusses the basic principles of different methods of pavement design. It also explains the design considerations of subgrade soils in each method. Section 2.2 presents the qualitative and quantitative descriptions of pavement performance. Then, considerations of bearing capacity in the design and performance of flexible pavements are discussed in section 2.3. Section 2.4 describes an in-depth view of the effect of load related and environmental factors on the response of subgrade soils. In addition, material and performance models with the emphasis of subgrade soils are presented. Finally, section 2.5 summarises the main themes of this chapter.

2.1 Pavement design

Flexible pavements are the most widely used transportation infrastructures all around the world. The choice of flexible pavements depends on different factors such as the design period, initial cost, traffic, ground conditions, and environmental factors. Long-term considerations, for example lifetime cost and maintenance budget are also important factors to be taken into account. Huang [49] described that the main concept behind design of conventional flexible pavement is to provide layered systems with stiffer materials on the top where the intensity of stress is high and inferior materials (in terms of strength and quality) at the bottom where the stress intensity is low. A typical flexible

pavement section is composed of asphalt concrete layer, bounded and/or unbounded base layer, sub-base and subgrade layers. Figure 2.1 illustrates the conventional road design in Norway.

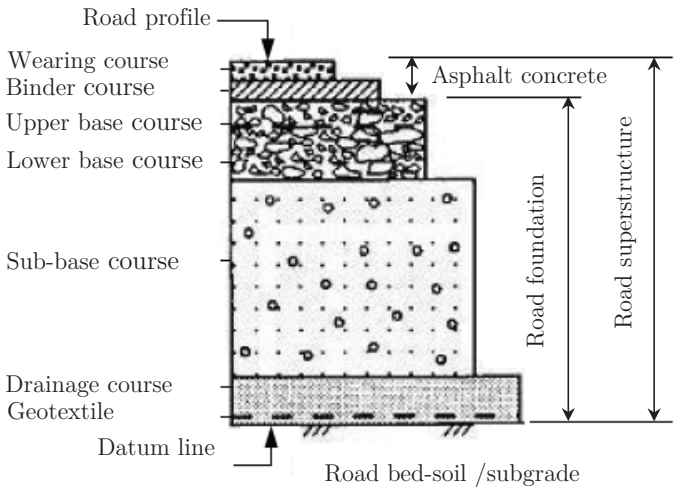

Figure 2.1: Principles of flexible pavement design in Norway (a typical road section). Adapted from NPRA [84].

The type and thickness of pavement layers are optimized to fulfil both structural and economical requirements based on the availability of local construction materials. The wearing course indicated in Figure 2.1 is made of dense graded hot mix asphalt (HMA) that has high resistance again deformation due to traffic loads. It can also be stone mastic asphalt (SMA) on high-volume roads to increase the resistance against wearing of studied tires. At the same time, it provides a smooth skid resistant surface and protects water from entering into the underlying layers and subgrade. The binder course comprises larger aggregates and less bitumen to achieve an economical design. Moreover, the compaction process will be effective if two layers (wearing and binder course) are provided instead of one thick HMA layer.

The base course layer is composed of untreated or stabilized aggregates. In some cases, base courses are made from variety of HMA mixes when a stiffer base layer is required, for instance for roads built on weak subgrades. The sub-base course layer usually consists of aggregates. In addition to its structural support, the sub-base course provides an improved drainage and protects frost action in roads. Due

to this, it is interchangeably known as a "*frost protection*" layer in Norway. The subgrade is an in situ soil or a selected material compacted to the desirable density near to optimum moisture content. In practice, geotextiles are used to separate the sub-base layers from the subgrade, mainly to prevent the fines from entering to the upper layers and also to avoid loss of aggregates to the soil. During construction of roads on soft soils, it can be necessary to use geotextiles as a reinforcement to be able to place the sub-base layer on the weak layer.

During pavement design, there are three fundamental design parameters: material characteristics, traffic loading and environmental factors. These design parameters must be incorporated in the pavement design tool to obtain a reliable response of the pavement structure (Figure 2.2). However, the theoretical framework of including every aspect of the influencing factors has not been yet feasible, at least in practice. One of the methods to alleviate such difficulties is to analyse the effect of individual factor and the combined effect of two or more factors when it is possible. Table 2.1 presents some examples on the assumptions used to develop a fairly practical method to characterize pavement materials.

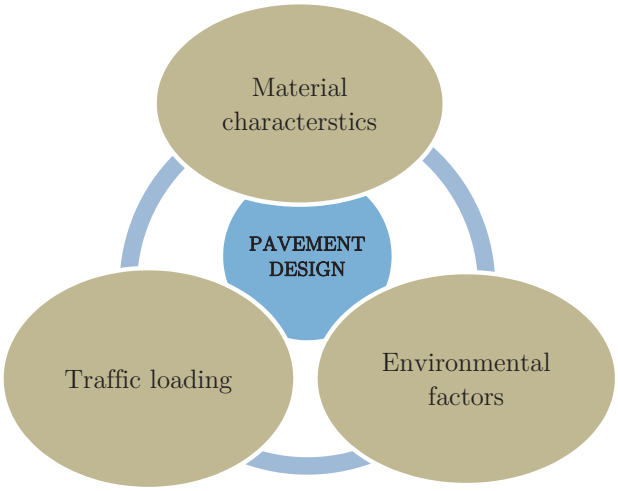

Figure 2.2: Design factors that affect pavement design.

Table 2.1: Examples of assumptions used to describe different design parameters.

Type of external parameters	In reality	In practice	Possible consequences
Material characteristics	Materials are non-homogeneous, fundamental behaviour of soils/aggregates depends on the interaction at a particle level.	Each pavement layer is assumed to be homogeneous. Continuum elements are assumed to be sufficient for finite element models.	Parameters are not properly estimated, especially for aggregates.
Traffic loading	The stress induced from each vehicle is different; it depends on total vehicle load, the axle configuration and tire pressure.	Traffic loads are converted to equivalent standard axle load.	Leads to conservative design. Probabilistic methods estimating traffic loads give more realistic design load parameters
Environmental factors	The moisture content in subgrade soils varies seasonally. In cold climate regions, the strength of soils is also a function of temperature variation(in the freezing and thawing mechanism)	A reduction coefficient is used to account the effect of reduction of strength of the soil due to thaw weakening or change of moisture content.	Deterioration of low-traffic volume roads in cold climate regions due to adverse weakening of bearing capacity than normally expected.

Three types of pavement design methods are presented in this study, namely empirical method, mechanistic-empirical method, and finite element method (FEM). Each method is discussed as follows.

2.1.1 Empirical pavement design method

The knowledge of pavement design has been widely established based on empirical correlations; commonly based on laboratory and full-scale tests, long-term observations of pavement performance, and experience. Even nowadays, empirical pavement design methods are widely used in many countries. The fundamental platform of empirical pavement design method was obtained from the "*AASHO road test*" which resulted in the American Association of State Highway and Transportation Officials (AASHTO) road design manual guide. The basic design equation for flexible pavements in the AASHTO road design manual [1] is presented in Equation [2.1] :

$$\log_{10}(W_{18}) = Z_R \times S_0 + 9.36 \times \log_{10}(SN+1) - 0.20 + \frac{\log_{10}\left[\frac{\Delta PSI}{4.2-1.5}\right]}{0.4 + \frac{1094}{(SN+1)^{5.19}}} + 2.32 \times \log_{10}(M_R) - 8.07 \quad [2.1]$$

Where W_{18} is predicted number of 18kip (80kN) equivalent single axle load applications, Z_R is standard normal deviate corresponding to the level of reliability, S_0 is combined standard error of the traffic prediction and performance prediction; ΔPSI is difference between the initial design serviceability index (p_0) and the design terminal serviceability index (p_t); M_R is the resilient modulus (in psi); SN indicates the structural number of the total pavement thickness, as shown in Equation [2.2].

$$SN = a_1D_1 + a_1D_1m_2 + a_1D_1m_2 \quad [2.2]$$

Where a_i is i^{th} layer coefficient, D_i is i^{th} layer thickness; m_i is i^{th} layer drainage coefficient.

The empirical equation in the AASHTO method shows the different factors that are considered for design, for instance traffic, pavement performance (serviceability), road bed soil (subgrade), and drainage coefficients. The subgrade layer is characterized by its resilient modulus. This method was prevailing from empirical design context and has been widely used for pavement design in practice. The main limitation associated to this method is that it cannot be universally used without calibration of the coefficients to local conditions.

The Norwegian pavement design method [84] provides standard tables and equations for the thickness of pavement layers depending on traffic data, ground condition and influences of climate. The three main requirements to ensure the quality for the selection of road materials are sufficient bearing capacity, non-susceptibility to frost and good drainage. The traffic data is used to determine the type and thickness of the asphalt layer. The choice of base course and frost protection layers depends on the traffic data and the ground conditions. Two factors are considered to characterize subgrade soils, namely frost susceptibility and bearing capacity. The frost susceptibility categories depend on the percentage of fine materials. It is shown in Table 2.2 that when there is large portion of very fine particles such as clays, the permeability of the soil is greatly reduced and the soil may not be highly frost susceptible.

Coarse-grained soils such as sand and gravel are highly permeable and have low suction potential. Hence, they are considered as little or non-susceptible to frost depending on the amount of fines. Silt and silty-clay soils have a highly optimized grain structures that provide favourable conditions for both suction and permeability which are the major components for the formation of ice-layers in soils. Table 2.3 shows the choice of bearing capacity groups depending on the material type and frost susceptibility in the Norwegian pavement design method. For obtaining the thickness of frost protection layer, fine-grained soils (clay and silt) are further categorized depending on their undrained shear strength.

Table 2.2: Classification of frost susceptibility [84].

Frost susceptibility groups	Materials < 22.4 mm		
	<2μm	<20μm	<200μm
None susceptible (T1)		< 3	
Little susceptible (T2)		3 - 12	
Medium susceptible (T3)	*	> 12	<50
Highly susceptible (T4)	< 40	> 12	>50

*Soils with more than 40% less than < 2μm are categorized as T3.

Table 2.3: Bearing capacity classification of the subgrade layer [84].

Underground material (Subgrade type)	Frost susceptibility	Bearing capacity group
Rock cut, stone fill	T1	1
Gravel, ($C_u \geq 15$)	T1	2
Gravel, ($C_u < 15$)	T1	3
Rock cut, stone fill	T2	3
Sand, ($C_u \geq 15$)	T1	3
Sand, ($C_u < 15$)	T1	4
Gravel, sand, moraine	T2	4
Gravel, sand, moraine	T3	5
Clay, silt, moraine	T4	6
Peat**		7

**Bearing capacity group 7 requires special considerations, ground improvement is required.

C_u is coefficient of uniformity ($C_u = D_{60}/D_{10}$) where D_{60} is the grain diameter at 60% passing, and D_{10} is the grain diameter at 10% passing.

The empirical pavement design method has been used for many decades, and is well known among road engineers. The main components of empirical equations are based on field observations. Morever, additional parameters can be developed and incoporated into the emprical methods to account for the variability in material characterization, traffic loading and climatic factors. Nonethless, such methods are developed based on specific road materials and soil types. Besides, there is no profound understanding of the mechanics of pavement materials and the relationship between the design factors considered and their outcomes. The consequence of such assumptions limits empirical methods from being directly

used to other places where nature of the design factors is different. In order to alleviate this problem, a mechanistic-empirical method is introduced where the mechanics of materials is used to some extent in combination with empirical data.

2.1.2 Mechanistic-empirical design method

Mechanistic design approach explains the deformation behaviour of materials and different mathematical models are used to describe this phenomenon. Huang [49](*Chapter 1, p. 3*) explained the concept of mechanistic-empirical method as "method of design which is based on the mechanics of materials that relates an input such as a wheel load to an output or pavement response such as stress or strain. The response values are used to predict distress from laboratory tests and field-performance data. Dependence on observed performance is necessary because theory alone has not proven sufficient to design pavements realistically".

The basic assumption of mechanistic-empirical method is based on layered elastic approach, in which each pavement layer is considered as homogeneous. For multi-layer system of pavement analysis, further assumptions are carried out, such as pavement layers extend infinitely in the horizontal direction, the bottom layer extends infinitely downward, and materials are not stressed beyond their elastic ranges. Figure 2.3 shows the location of critical strains in a conventional flexible pavement. In the same Figure, point "a" represents the location where the total deformation of all pavement layers is measured. The amount of total deformation is directly used to quantify the amount of rut and roughness of the road surface which are the major components for road maintenance decision.

The critical horizontal tensile strain is obtained at point "b" in Figure 2.3. Based on the value of the tensile strain, the total number of load repetitions causing fatigue failure is estimated using pavement performance models. Again, referring to Figure 2.3, at point "c", the vertical elastic compressive strain on the top of the sub-base layer is used to predict the total number of load repetitions based on rutting models. On the top of the subgrade, at point "d", the vertical elastic strain is obtained to predict the maximum allowable standard load repetitions from subgrade rutting models.

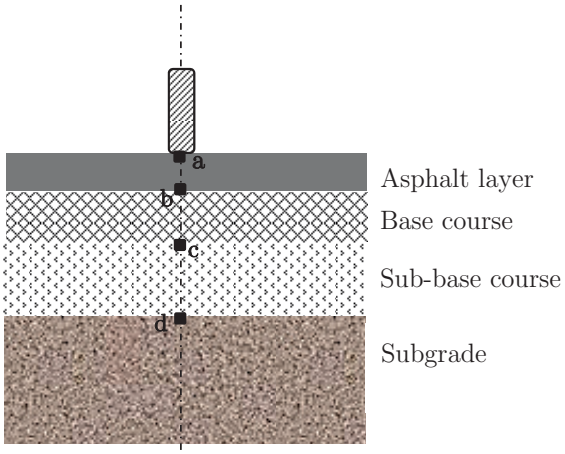

Figure 2.3: Critical strain locations in a flexible pavement.

The principle of limiting the vertical elastic strain on the top of the subgrade layer is based on the fact that plastic strains are proportional to elastic strain in pavement layers. When the elastic strain on the subgrade is limited, the elastic strains in other components above the subgrade will also be controlled. Consequently, the magnitude of permanent deformation on the pavement surface will be controlled [49]. Odermatt *et al.* [85] presented full-scale test measurements based on heavy vehicle simulator as illustrated in Figure 2.4. The results clearly indicated that the rut depth measurements have been consistently proportional to the dynamic vertical subgrade strain.

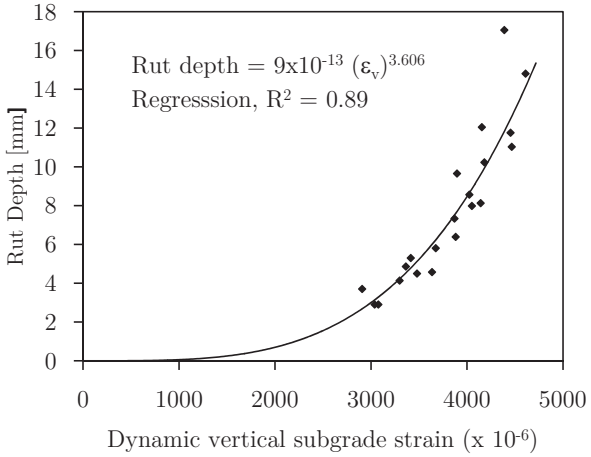

Figure 2.4: Relationship between rut depth and vertical elastic strain. Adapted from Odermatt *et al.* [85].

The generalized methodology for adopting mechanistic-empirical method [49] is outlined in Figure 2.5, where the pavement configuration is subjected to design iterations for a given traffic, material and climatic data and distress models. The type and property of pavement layers are changed if changing of the pavement configuration does not satisfy the design requirement. Though a conventional mechanistic-empirical model has not been adopted yet, different road agencies have developed their own programs based on their design standards and local conditions [3],[111],[113].

Mechanistic-empirical design programs provide the possibility to extrapolate from limited data, such as changing of load types, environmental factors and aging of materials. In this way, pavement materials are utilized more effectively than the methods used in empirical approach. In addition, the actual strength of pavement materials can be obtained from back-calculation of field tests. In combination with pavement performance models, the reliability of pavement design is improved.

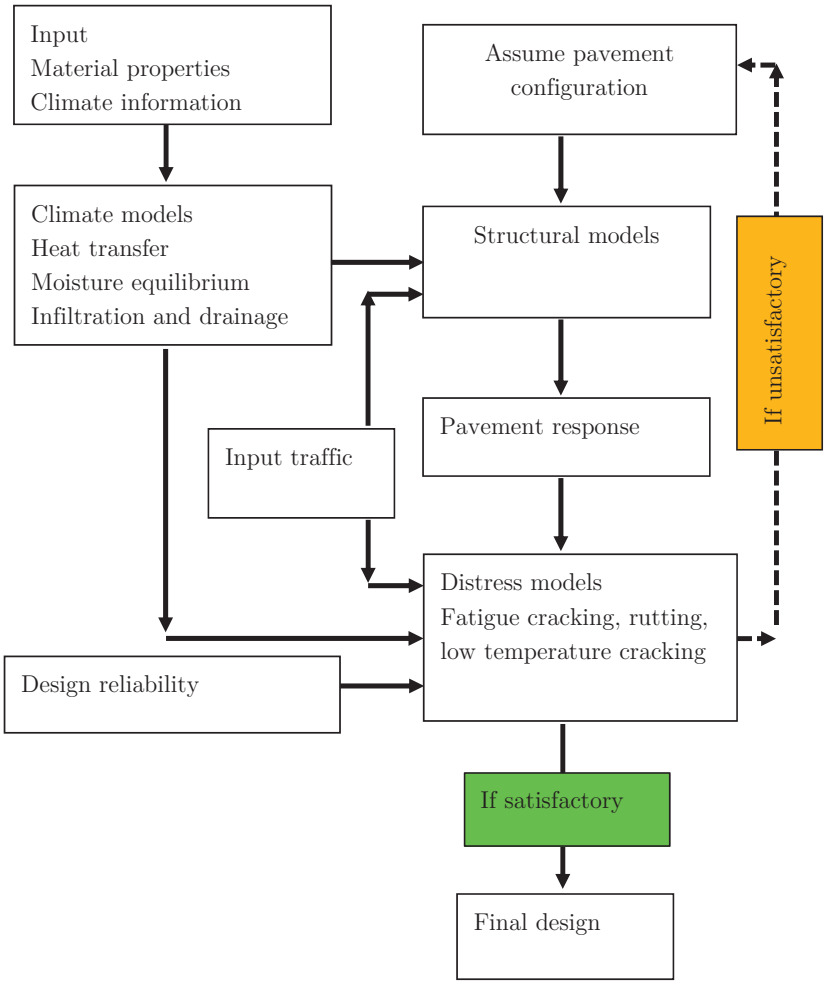

Figure 2.5: Methodology of mechanistic procedure for flexible pavement design. Adapted from Huang [49] (*Chapter 11, p. 473*)

Even though mechanistic-empirical methods give a more realistic design approach than purely empirical one, there are some limitations associated to them. The material models of mechanistic-empirical methods are based on elasticity theory and they consider only the elastic response of pavement materials. For instance, limiting the rutting in pavements based on the subgrade strain criterion does not consider the actual load-associated plastic strains; rather, it is based on performance prediction models. Hence, new constitutive models based on the concept plasticity theory should be developed to capture the accumulation of load-induced plastic strains more appropriately. At the same time, the knowledge of finite element method is the main platform for developing new models and applying them in practice.

2.1.3 Finite element method

Finite Element Method (FEM) has been widely used for wide variety of engineering problems. Finite element method is defined as [27](*Chapter 1, p.1*) "a method for numerical solution of field conditions to determine the spatial distribution of one or more dependent variables". Any boundary value problem in FEM is governed by kinematics, equilibrium and constitutive behaviour. Kinematics defines the relationship between displacement and strain. The equilibrium equations must fulfil that the externally applied loads are equal to the sum of the internal element forces. Kinematics and equilibrium are universally applied to any material, and the constitutive law characterizes the behaviour of a particular material.

In FEM, individual finite elements can be visualized as small pieces of a structure. The elements are then connected at each node to form an approximate system of equations for the whole structure. The particular arrangement of elements is called a "mesh". The mesh is represented numerically by a system of algebraic equations to be solved for unknowns at nodes. The solution for nodal quantities when combined with the assumed field in any given element, completely determines the spatial variation of the field in that element. Thus the field quantity over the entire structure is approximated element by element, in piecewise fashion [27].

There are some finite element programs for specific purpose of analysis and design of pavements. Road agencies at different countries have developed their own

version of finite element programs. The most widely known programs are: MICH-PAVE (Michigan State University and Michigan Department of Transportation, USA); Mn-PAVE (Minnesota Department of Transportation, USA); ILLI-PAVE (University of Illinois, USA). These programs are based on an axisymmetric model and pavement response (displacements, stresses, and strains) is calculated from a single circular wheel load. Each layer in the pavement cross-section is assumed to extend infinitely in the horizontal direction and the last layer (usually the subgrade) is assumed to be infinitely deep.

On the other hand, there are different commercially available advanced finite element programs. Some of the widely known general purpose programs are Abaqus FEA, ANSYS, LS-DYNA, and Nastran. All these programs provide advanced finite element modelling features. In this PhD study, Abaqus is used. Abaqus was originally released as "ABAQUS" in 1978 by Hibbitt, Karlsson & Sorensen, Inc. Nowadays, it is known by the name "Abaqus FEA", and is acquired by Dassault Systèmes. This program has a wide range of material modelling capability and is one of the robust programs in solving nonlinear material behaviour. Modelling options are available for dynamic contact problems (such as modelling of rolling wheel on a pavement), and new features of coupled analysis (such as modelling of heat transfer and consolidation in soils). Most importantly, the program provides the possibility to use user subroutines for any material models developed by the user in a relative easy way.

2.2 Pavement performance

Pavement performance is defined by Lytton [66] as the evaluation "for how pavements change their condition or serve their intended function with accumulating use". The term performance is contextual, i.e. its meaning differs at project and network level. It also depends on the public acceptance and changes over time. For example, the value of roughness index might be accepted some years ago, but may not be good enough now. The network level performance evaluation also varies depending on the district, province and country. Performance evaluation at broader network level (such as at a province or national level) is mainly for selection of optimal maintenance strategies, evaluation and proposal of road policy, and funding. Project level models are more detailed, and they are used in analysis and design of pavements.

Performance models are generally categorized in to two groups [66]: deterministic and probabilistic models. Deterministic models predict the life of the pavement and the level of distress, while probabilistic models predict the distribution of the events. There are different types deterministic models, namely primary response models, structural performance models, functional performance models and damage models. The primary response models predict the direct effect of traffic loads and environmental factors, such as stress, strain and deformation. Structural performance models measures the pavement condition (pavement condition index), while functional performance models are used to evaluate the serviceability of the pavement (e.g. present serviceability index (PSI)) based on driving comfort and traffic safety. In this study, the main modes of distress which are used in deterministic models are discussed.

2.2.1 Rutting

The definition of "rut" in pavement engineering is the surface depression in the wheel path (Figure 2.6). The main sources of rutting in flexible pavements are permanent deformation of pavement layers and wear of pavement surface. The permanent deformation from a single load cycle is very small. However, the accumulation over many load repetitions (i.e. thousands to millions) leads to a visible and appreciable amount of rut on the pavement surface. The permanent deformation of pavement layers, in particular subgrade soils, will be briefly discussed in section 2.4.2. Although all pavement layers contribute for rut formation, it is always the rut measurements on the surface of the pavement that are used in Pavement Management System (PMS). The magnitude of rut at the surface does not tell us the explicit contribution of each layer, but the major causes and responsible layers can sometimes be obtained based on the geometry/characteristics of the surface rut (see Table 2.4).

Figure 2.6: Surface rutting with high degree of severity [81].

Table 2.4: Different modes of rutting based on the descriptions presented in Dawson & Kolisoja [29].

Classification of rutting	Rut geometry/ characteristics	Major causes	Responsible layers
Mode 0	Narrow depression in the road surface, mostly near the wheel path.	Insufficient compaction	Asphalt layer
Mode 1	Narrow ruts with net cracking on the bottom of the wheel path.	Large plastic shear strains, dilation	Granular material layer
Mode 2	A broad rut with slight heave remote from the wheel.	Weak subgrade	Subgrade layer
Mode 3	Sharp shaped ruts, with rut distances similar to vehicle wheel spacing.	Tire wear; studded tires	Wearing course

Rutting of subgrade soils is often associated to inadequate structural design and heavy traffic axle load. If the HMA surface layer is of poor quality (due to poor mix design or improper construction), rutting can be confined to the top 50 to 70mm of the pavement [42]. Rutting of pavements due to a studded tire is a common phenomenon in cold-climate regions where tires with metal studs are used to increase traction on slippery roads (usually ice during winter). The direct impact of rutting due to studded tires is on the asphalt surface. The extent of surface rut due to studded tire can be reduced by using aggregates that have high resistance against abrasion. However, the rutting on the surface can impair the surface drainage and water may transport through the cracks which consequently affects the deformation behaviour of the unbound layers.

The primary concern of rutting is safety consideration such as the potential for hydroplaning and maintenance problems [1] (p. I-27). In order to outline a preventive maintenance strategies, Hicks *et al.* [42] proposed three severity levels for ruts on the basis of the potential for hydroplaning and wet-weather accidents.

- Rut depth less than 6mm (low severity): Problems with hydroplaning and wet-weather accidents are unlikely.
- Rut depth between 6mm and 12mm (medium severity): Inadequate cross slope can lead to hydroplaning and wet-weather accidents.
- Rut depth exceeding 12mm (high severity): The potential for hydroplaning and wet-weather accidents is increased.

Nearly all pavement performance measurements are based upon observations or measuring at the surface of the pavement. Nowadays state-of-the-art automated equipment is used to collect pavement performance data as a main input of PMS in road agencies. NPRA uses a modern laser scanner technology for measuring the pavement surface characteristics such as the rut depth, roughness and cross-sectional profile [112]. In the Norwegian PMS, threshold values of rut depth, roughness and friction are used to carry out a corrective road maintenance planning. The threshold values depend on the type of road sections (sectional or network level), the road category and the amount of Average Annual Daily Traffic (AADT).

Based on the Norwegian road operation and maintenance manual [83], maximum allowable limit of rut depth is shown in Table 2.5. Although Hicks *et al.* [42] suggested a threshold value of 12mm to cause severe conditions, road agencies usually consider higher values of rut depth limit for maintenance decision. For

example, the Norwegian maintenance guideline [83] allows the critical maximum rut depth as high as 25mm. This is majorly to optimise planning of maintenance strategies.

Table 2.5: Maximum allowable rut depth at network and sectional level in Norway [83].

AADT	Rut depth (mm)			
	Network level[1]		Road section[2]	
	Trunk	Main	Trunk	Main
0-300	17.5	18.5	25	25
301-1500		18.0		25
1501-5000	17.0	17.5	25	25
>5000	16.5	17.0	25	25

[1]90% of the road network belongs to the specified AADT category.
[2]10% the road section is measured during autumn after repaving.

2.2.2 Cracking

Cracks in flexible pavements occur due to the tensile strains (tensile stresses). Cracks can be load-related or non-load related. Non-load related cracks are usually caused by temperature variation. In some cases, swelling of subgrade soils (for example, expansive soils in Tropical countries and frost action in cold climate regions) causes upward bulge on the pavement surface, which results in surface cracking. A more conventional way to evaluate cracks is based on their pattern of cracking; such as longitudinal and transverse cracking, alligator or fatigue cracking, and block cracking. Longitudinal cracks (Figure 2.7a) are parallel to the pavement centreline while transverse cracks (Figure 2.6b) extend across the centreline. These cracks are usually non-load associated. The possible causes can be shrinkage of asphalt surface due to low temperatures, asphalt hardening or reflective cracks caused by cracks beneath the asphalt surface. The causes of longitudinal cracks can also be poor joint construction [49]. Premature failure may happen if the joints are on the wheel path (particularly for multi-lane) roads.

(a) (b)

Figure 2.7: a) Longitudinal cracking with medium degree of severity, and b) transverse cracking with high degree of severity [81].

Figure 2.8: Fatigue cracking with high degree of severity [81].

Fatigue cracking (Figure 2.8) is a series of interconnecting cracks caused by the fatigue failure of an asphalt surface or a stabilized base under repeated traffic loading. In thin pavements, cracking initiates at the bottom of the bound layer where the tensile stress is highest and propagates to the surface, which is commonly known as "bottom-up" fatigue cracking. On the contrary, the cracks in thick pavements are most likely initiate from the top surface due to localized high tensile stresses resulting from tire-pavement interaction and asphalt binder aging. This type of cracking is called "top-down" cracking. The initial patterns, in either case, might be longitudinal cracking.

Fatigue cracking is the consequence of longitudinal and transversal cracking. When there is inadequate structural support due to spring thawing and poor drainage or inadequate compaction, the repeated loads aggravate the formation of

many-sided sharp-angled pieces that develop into a pattern resembling the back of an alligator or crocodile [89]. Interconnected cracks that divide the pavement into rectangular pieces are known as block cracking.

The major problems of cracking in pavements are infiltration and roughness. The cracks on the surface of the pavement accelerate the moisture infiltration to base and subgrade layers. As a consequence, the bearing capacity is reduced and additional cracks are induced as a result. If corrective measures are not taken in time, potholes will eventually develop and a complete failure of the pavement surface may happen.

2.2.3 Roughness

Pavement roughness is an expression of the condition or irregularities on the pavement surface that highly affect the ride quality of a vehicle which is directly related to vehicle delay cost, fuel consumption and maintenance cost [88]. Although rut depth and cracking are the direct physical measurements to evaluate the extent of distress, it is the roughness that provides the major correlation variable to compute the pavement serviceability index [49].

Nowadays, the quantitative description of roughness widely used, is International Roughness Index (IRI). IRI is defined by the ratio of the accumulated suspension motion to the distance travelled obtained from a mathematical model of a standard quarter car at a speed of 80km/h [49]. The unit of measurement of IRI is mm/km or in/mile. The scale of roughness (IRI ranges) for different classes of roads [101] is shown in Figure 2.9. There is no absolute perfection of roughness even for new pavements. In practice, high class roads that allow high traffic speed and airport runways have (or must have) the lowest possible IRI. In the contrary, damaged pavements and unpaved roads have high IRI values. Table 2.6 shows the maximum allowable roughness in the Norwegian PMS. Similar to rutting, the limit of roughness for maintenance planning depends on the road category, and traffic volume.

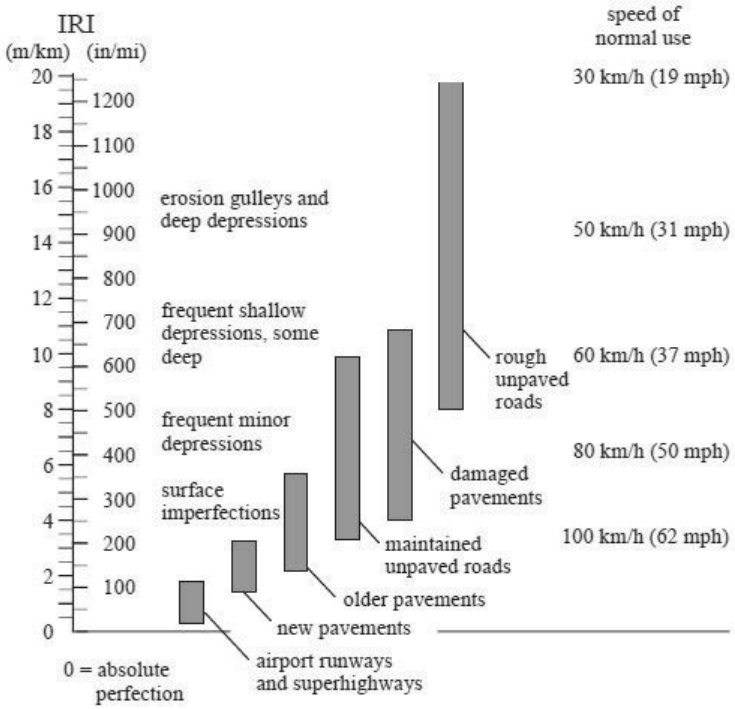

Figure 2.9: IRI roughness scale [101].

Table 2.6: Maximum allowable rut depth and roughness at network level.

AADT	Roughness (IRI)			
	Network level[1]		Road section[2]	
	Trunk roads	Main roads	Trunk roads	Main roads
0-300	3.5	6.0	5.0	7.0
301-1500		5.0		6.0
1501-5000	3.0	4.0	4.5	5.1
>5000	2.5	3.0	4.0	4.6

[1]90% of the road network belongs to the specified AADT category.
[2]10% the road section is measured during autumn after repaving.

2.2.4 Surface friction

Another important aspect of road performance is surface friction. Surface friction is mainly a safety issue and it depends on the tire and pavement surface characteristics. There is no direct relation between surface friction and ground conditions. However, an indirect effect of other pavement distresses on surface friction is eminent. For example, rutting is influenced by the subsoil conditions and the ice or water retained in the surface ruts significantly affects the surface friction between the tire and pavement surface.

2.3 Bearing capacity

The prospect of bearing capacity in pavements has two main contexts. The first context insures that the pavement section is sufficient enough to avoid any shear failure. In this case, the definition of bearing capacity in pavement engineering is similar to that of geotechnical engineering. The cohesion and friction angle of subgrade soils and other pavement components are considered. In practice, pavements are designed with high safety factor against localized shear failures, because the strength of pavement layers is usually significantly higher than the bearing capacity. Nonetheless, the principle of bearing capacity concept against shear failure is usually the primary consideration in the design of unpaved roads [86],[48].

In the second and main context, bearing capacity is related to the long-term performance of the pavement, i.e. pavement should be designed for riding comfort than for barely preventing shear failures [49] (*Chapter 1, p.2*). This is the main aspect of bearing capacity in flexible pavements. Road performance models are used to estimate the total number of allowable load repetitions that the pavement can operate without structural and functional failures. The performance models are related to the strains in the pavement layers and the adequacy of the pavement layer is obtained based on deflection measurements where the stiffness of individual layers is back-calculated. Field tests are carried out using non-destructive testing such as Falling Weight Deflectometer (FWD) and Plate Load Testing (PLT).

In Norway, the bearing capacity of road subgrades is determined from two methods [83]: deformation measurements and dug-up samples. FWD is used to

determine the deflection of a road under falling load. The deflection is used as an expression of the road's bearing capacity, where Equation [2.3] is used for paved roads [82].

$$B = 11\left[\frac{\left(\frac{110p}{G_1 - G_2}\right)^{0.5}}{200}\right]^{0.6}\left(\frac{50}{AADT}\right)^{0.072} \quad [2.3]$$

Where B is a bearing capacity index, $AADT$ is the average annual daily traffic for heavy vehicles, p is the contact pressure (in MPa), G_1 is the deflection at the centre of the load (in mm), G_2 is the deflection at 20cm from the centre of the load (in mm).

One of the main challenges in pavement engineering regarding to bearing capacity is "*how to measure it?*" One of the strategies commonly used in road construction is to select appropriate materials for standardized layer thickness and the quality of these materials is ensured during road construction. Additionally, bearing capacity is considered as a relative measure used to identify weak parts of a section and it is not easy to measure it quantitatively. Due to this fact, the research interest is mainly on understanding the factors that affect the bearing capacity, rather than developing a particular model to quantity it. In the following sections, the two most important aspects of bearing capacity in subgrade soils are discussed: compaction, and climatic factors.

2.3.1 Compaction

Compaction is a mechanical stabilization or densification of unbound materials such as soils and aggregates. Soils are often weak and highly compressible and compaction is the cheapest alternative to enhance the strength. Early in 1930s, Proctor[94] was the pioneer in developing the fundamental principles of compaction in cohesive soils. He outlined that compaction is a function of four variables, namely dry density, water content, compaction effort and type of soil.

The relationship between the dry density and the moisture content during compaction process is shown in Figure 2.10. As the water content increases starting from low water content during compaction, the particles develop larger and larger water films around them. The water acts like a lubricant and makes the particles to move easily. Eventually, the particles reorient into a new state

(denser configuration). In the process, a particular water content is obtained above which the density does not increase any further. This particular water content is the "optimum water content" and the corresponding dry density is the "maximum dry density". Increasing the water content beyond the optimum point leads the dry density to reduce since water starts to replace soil particles [46] (*Chapter 5, p.116*).

In addition to the moisture content, the dry density obtained from compaction largely depends on the type of compaction and the compactive effort. Static pressure and kneading are effective method of compaction in cohesive soils. The compaction effort is affected by "drum" type (for example sheep-foot drums are more effective than smooth drums for cohesive soils to create small shearing zones), the weight of the roller, and the number of passes. In non-cohesive soils, dynamic compaction is highly effective. This type of compaction is applied by a combined action of vibrating or oscillating roller drum and weight of the machine. The factors that affect the compaction effort, in this case, are the amplitude of vibration (displacement of the roller drum), the frequency and roller's travel speed.

The effect of compaction effort is presented in Figure 2.11 and explained by Holtz & Kovacs [46] (*Chapter 5, p. 117-118*) that "at the same compactive effort, with increasing water content, the soil fabric becomes increasingly oriented. At dry of optimum, the soils are always flocculated, whereas wet of optimum the fabric at point C is more oriented than at point A. If the compactive effort is increased, the soil tends to become more oriented, even dry of optimum. The sample at point E is more oriented that at point A. Wet of optimum, the fabric at point D will be somewhat more oriented that at point C, although the effect is less significant than dry of optimum".

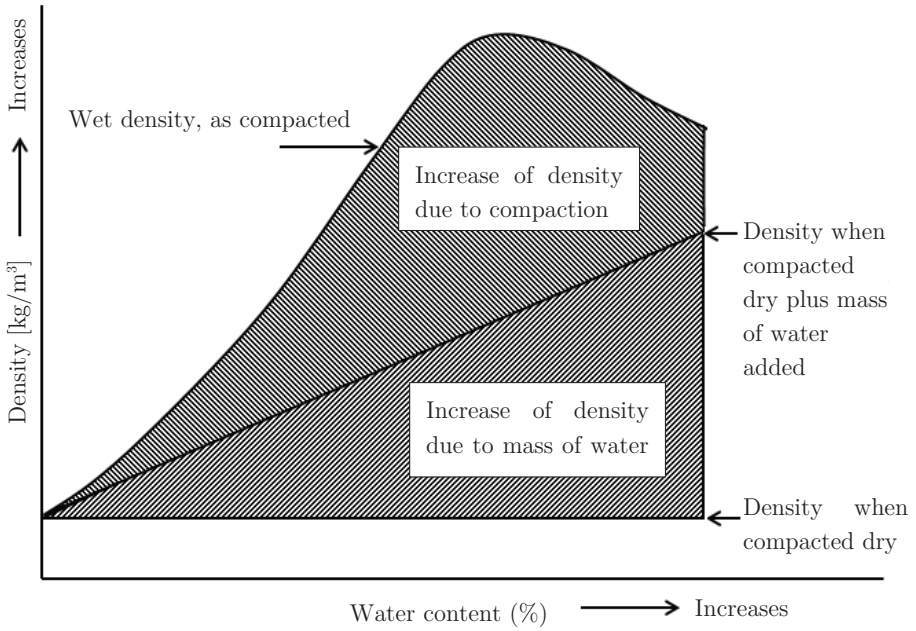

Figure 2.10: Relationship between dry density and water content in soils. Adapted from Holtz & Kovacs [46](*Chapter 5, p. 116*).

The maximum dry density and the optimum moisture content of different types of soils are determined following standardized testing procedures and equipment [9],[10]. For performance based specification of field compaction a certain degree of compaction based on the laboratory test results is considered. For example, the contractor must achieve a compacted field dry density of 90-95% of the maximum dry density determined in the laboratory either the standard or modified Proctor test. The most common methods for measurement of field compaction are Sand Cone method [7], Nuclear Method [8], Rubber Balloon method [11].

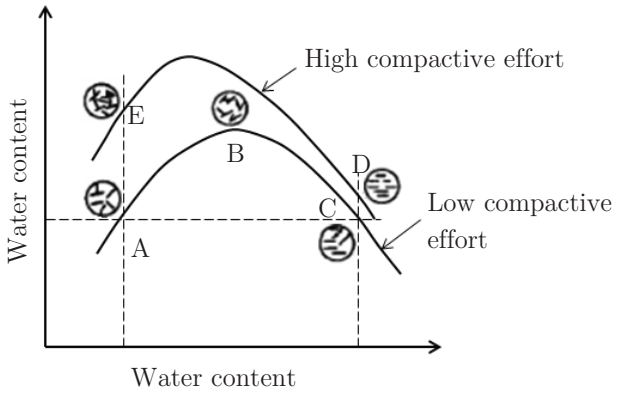

Figure 2.11: Effect of compaction effort on the compaction curve. Adapted from Lambe (1958a) as cited in Holtz & Kovacs [46] (*Chapter 5, p. 118*).

In recent years, Intelligent Compaction (IC) or Continuous Compaction Control (CCC) has been a research interest in controlling compaction during road construction [92],[14]. The IC method uses modern rollers equipped with an integrated measurement system, on-board computer reporting system, Global Positioning System (GPS) based mapping and optional feedback control [24]. The system controls different compaction parameters for the roller such as drum vibration, amplitude, frequency, and working roller speed. The output parameter in IC is soil modulus which is calculated continuously on the basis of the monitored drum acceleration [14]. Soil modulus is a design parameter and provides a better characterization of pavement materials than dry density.

Another important factor in field compaction is the choice of "lift thickness". Lift height refers to the depth of the soil layer, over the previously compacted layer. It affects both machine performance and compaction cost. Road agencies usually specify the limit for lift thickness. The choice of lift thickness depends on the soil type, the compaction method/type and the compaction effort. The latter two factors have been the main considerations in practice. For instance, similar lift heights are considered for a range of fine-grained soils, and only the compaction method is varied. Based on numerical analysis of a roller compaction, Yesuf *et al.* [118] presented that the actual lift thickness can be chosen as a function of soil parameters, such as the cohesion and friction angle. The detailed descriptions of the study are discussed in Chapter 5.

2.3.2 Climatic factors

Climate is one of the major factors that affect design and performance of pavements. Subgrade soils — being beneath the pavement structure, are most susceptible to moisture variation due to their exposure to precipitation, impaired drainage and fluctuation of the ground water table. Moreover, the strength and deformation of fine-grained soils is highly influenced by the water content in the soil. In cold climate regions, temperature also plays a critical role in the freezing and thawing of soils in roads. This phenomenon affects the performance of pavements in two ways. First, the volume to the soil generally increases during freezing. Terzaghi *et al.* [107] reported that the volume increase associated with the freezing of a closed system[3] is ranging between about 3% and 5% of the total volume. Eventually, this process may cause a non-uniform heave on the pavement surface.

Second, the water generated during thawing period reduces the strength of subgrade soils, resulting in a reduction of bearing capacity of roads. The extent of damage on the pavement surface due to freezing and subsequent thawing of subgrade soils depends on many factors such as the thermal gradient, availability of water in the sub-soil layers, frost susceptibility of the soil, consolidation coefficient, permeability and drainage conditions. In the following sections, the pre-conditions, the physical process and consequences of both frost heave and spring thawing are discussed.

Frost heave

The three conditions necessary for ice segregation (frost heave) are frost susceptible soils, freezing temperature and availability of water. Ice segregation does not occur in the absence of one of the three conditions. The process of ice segregation depends on the interaction of heat and water flow through the mass of mineral and organic particles that make up the soil [55]. All water in the soil pore may not be fully frozen. The amount of unfrozen water varies with the type of soil, soil particle surface characteristics, the gradation of the soil and the temperature (see Figure 2.12). In general, finer soils contain larger amounts of unfrozen water at a given subfreezing temperature than coarser soils and for a

[3] A freezing system is called "closed-sytem" when there is no additional water except the available water in the soil.

given soil the unfrozen water content decreases with lower subfreezing temperatures. Moisture movement in the frozen zone makes insignificant contributions to frost heave. In the contrary, the moisture movement induced by negative pore pressures developed in the freezing zone has a major impact on the magnitude of frost heave [55],[114].

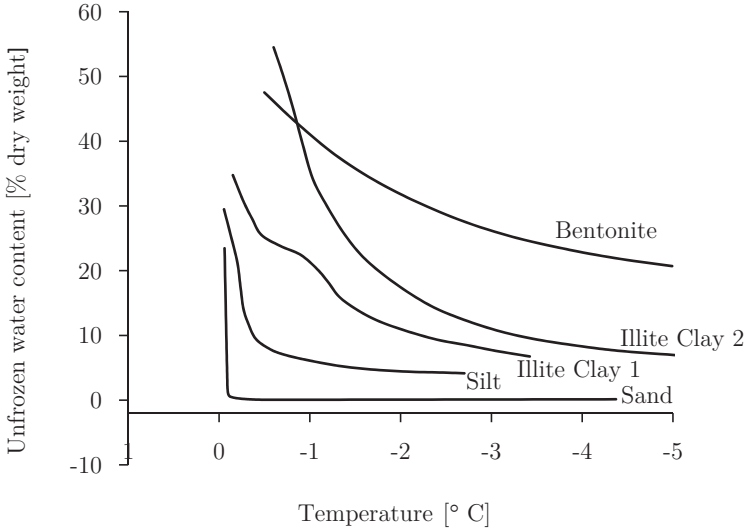

Figure 2.12: Amount of water remaining unfrozen water for various frozen soils. Adapted from Williams & Smith [114] (*Chapter 1, p. 7*).

Ice lenses develop only in fine-grained soils. During freezing the formation of ice results in water being confined progressively in a small space since the free energy of water falls as freezing takes place, causing cryosuction — migration of water to the freezing zone [107] (*Chapter 4, p. 50*). In perfectly uniform soils, ice lenses do not develop unless the grains are smaller than 0.01mm. Fairly uniform soils must contain at least 10.0% of grains smaller than 0.02mm. The formation of ice lenses in mixed-grained soils requires that at least 3.0% of the total aggregate is less than 0.02mm [115] (also Table 2.2 in section 2.1.1).

Kavanaugh [55] defined the boundary conditions of the freezing zone as lower and upper boundaries as illustrated in Figure 2.13. The lower boundary is characterized by the depth at which the temperature is equal to the freezing point

of the bulk water in the soil. This temperature is generally within one or two tenth of a degree below 0.0°C, depending on the chemical content of the water in the soil. The upper boundary in frost susceptible subgrade is defined as the bottom of growing ice lens where the negative pore pressure causes moisture movement to the ice lens.

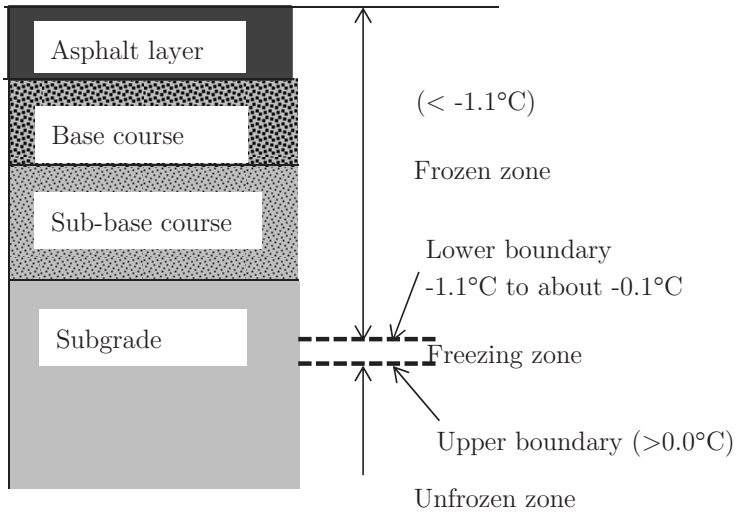

Figure 2.13: Freezing sequence in a typical pavement profile, adapted from Kavanaugh [55]. Note that thickness of the layers is not to scale.

The in situ pore-water will increase in volume by about 9% on freezing. This expansion does not necessarily lead to 9% increase in the voids of saturated sand or gravel since part of the water may be expelled during freezing. For saturated silt and silty sand, the effects of freezing depend on the rate at which the temperature is lowered. A sudden change in temperature leads the water to freeze in situ while for gradual change in temperature, a large part of the frozen water accumulates in the form of layers of clear ice oriented parallel to the surface exposed to the freezing temperature [5].

In cold climate regions, the effect of frost is one of the prime consideration for choosing the type and thickness of pavement layers. This is achieved by ensuring missing of one of the preconditions for the formation of ice in soils. For example,

- Providing non-frost susceptible subgrade soils and limiting the amount of percentage of fines in upper unbound layers, i.e. base and sub-base layers.
- Providing adequate thickness of frost protection layers to intercept the capillary flow. In engineering practice, frost protection layers are provided when the vertical distance between the water table and the frost line is smaller than the height of capillary rise in the soil [107]. The practical approach in many road agencies is developed from experience. The requirement for frost protection layer in Norway depends on the type of subgrade soil, the traffic class [84].
- To provide adequate drainage.

The practical consideration of frost susceptibility of road materials (particularly subgrade soils) is based on the percentage of fines. A more realistic classification of frost susceptibility by Konrad [59] suggested that there are three levels of sophistication in estimating the frost susceptibility of soils. The first level is primarily based on the percentage of soil finer than a specified particle size, which is commonly used in practical pavement design. In the second level, a more comprehensive information is required, i.e. grain-size distribution supplemented by tests addressing the soil-water interaction such as capillary rise, hydraulic conductivity of unfrozen soil, water-retention curve, and other properties of the soil such as Atterberg limits, specific surface area and clay content. The third level is based on evaluation of frost susceptibility based on direct measurements of frost heaving in the laboratory or in the field.

The immediate consequences of freezing and frost heave are mainly attributed to surface roughness. The severity of roughness on the pavement surface depends on the extent of differential heave. The effect of roughness on pavement performance is discussed in section 2.2.3. The strength of frozen subgrade soils is tremendously high and there is no concern of load associated deformation in pavement layers. During spring thawing, the segregated frozen ice starts melting and the strength of the subgrade soils is substantially reduced. This phenomenon is a major cause for weakening of bearing capacity in cold climate regions. The mechanisms and physical phenomenon of spring thawing is presented as follows.

Thawing

Thawing is a reversed process of freezing. Similar to freezing, the physical process of thawing is governed by heat transfer and thermal properties of soils. In contrary to freezing, energy (latent heat) is absorbed when the ice melts and turns to liquid. A pavement structure will be most susceptible to breakup during the period when excess water cannot drain downward through the still-frozen soil. The thawing process in roads can be from top downward or from bottom upward or both, depending on the pavement surface temperature [87]. A sudden spring thaw usually leads the melting almost entirely from the surface downward. If the rate of generation of water exceeds the discharge capacity of the soil, excess pore pressure will develop which can lead to failure of foundations and slopes [71].

Simonsen & Isacsson [103] illustrated the mechanisms of deterioration of a pavement structure due to spring thawing in Figure 2.14. Figure 2.14a shows that the bearing capacity of the subgrade is high as long as the thaw depth has not reached the subgrade. When the subgrade begins to thaw (Figure 2.14b), the excess pore-water pressure causes a significant reduction on the strength of subgrade soils. Consequently, the weak subgrade is deformed either due to reconsolidation and plastic deformation induced from the traffic loads. Then, the settlements propagate through the road structure (Figure 2.14c). At the late period of the spring thawing (Figure 2.14d), repeated loadings cause substantial deformation, which becomes a consequent failure of the pavement structure.

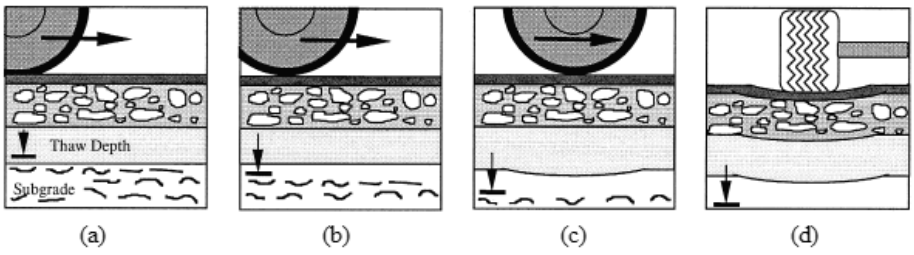

Figure 2.14: Mechanism of thaw weakening [103].

The factors affecting the development of thaw weakening can be divided as loading, environmental and design related factors [4]. The load related factors are the magnitude, amount and frequency of axle loads and the magnitude of tire pressures. The environmental factors comprise weather and hydrological factors including temperature, groundwater level, precipitation and amount of frost.

Design related factors are related to the road structure, drainage and subgrade conditions. Doré & Zubeck [33] states that thaw weakening of a typical pavement layer is essentially a function of three major factors: the amount of frost heave, the rate at which the layer is thawing, and the rate at which the layer consolidates.

2.4 Behaviour of fine-grained soils under repeated loading

Subgrade soils under pavements are subjected to cyclic traffic loading. The stiffness and strength of such soils is characterized in a better way when the loading conditions and the number of repetitions are properly assumed. Most cyclic characterizations of fine-grained soils in the mainstream geotechnical engineering (for example loading from earthquake and offshore structures) mainly focus on high loading frequency. The results obtained from such tests cannot be directly applied to the soils beneath a pavement. In this section, the behaviour of subgrade soils due to repeated loading is presented.

2.4.1 Resilient modulus

In the current practice of mechanistic-empirical pavement design [73], the state-of-the-art material characterization of subgrade soils includes the resilient modulus to measure the subgrade stiffness. The resilient modulus measures the elastic property of soil. It is obtained from the ratio of stress to stain for rapidly applied loads, like those experienced by pavements. The repeated load application to determine the resilient modulus is thought to more accurately simulate actual traffic loading, in contrary to CBR test.

Figure 2.15 illustrates the generalized stress dependent secant stiffness of a typical soil from a conventional triaxial testing. It is important to note that the secant modulus in this case is the ratio of the deviator stress to the total strain. In contrary, it is shown in Figure 2.16 that the resilient modulus is computed from the ratio of the deviator stress to the elastic strain component. The resilient modulus is normally obtained after few loading cycles since it is believed that the initial measurements are not representative due to sample disturbance and contact problems during cyclic triaxial testing.

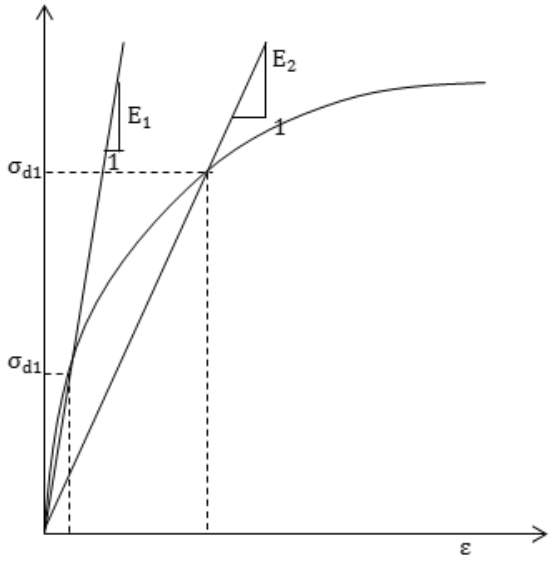

Figure 2.15: Illustration of generalized stress dependent secant stiffness of soil.

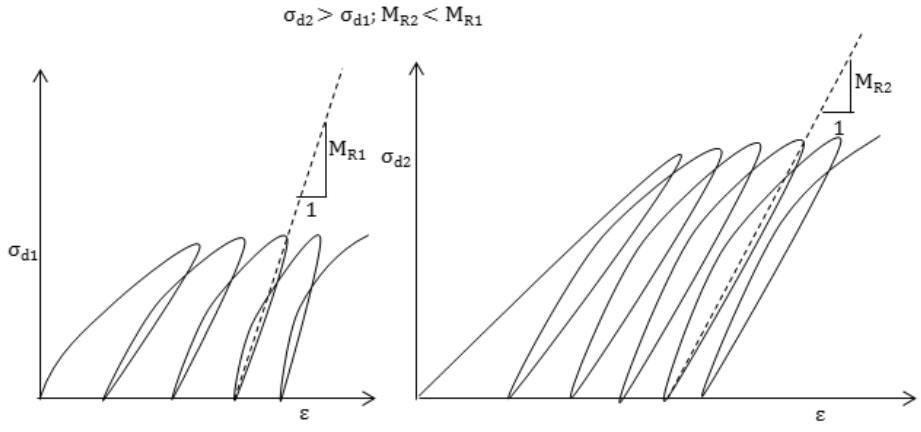

Figure 2.16: Illustration of stress dependent resilient modulus for subgrade soils.

Resilient modulus is directly used for the design of flexible pavements as it indicates a basic material property which can be used in mechanistic analysis for road design [1]. There are different methods to obtain the resilient modulus of soils and aggregates for pavement design. The well-known methods are listed as follows.

1. Laboratory repeated load resilient modulus tests: this is a direct measurement of resilient modulus [2].
2. Back-calculation of Non-Destructive Testing (NDT) data, for instance Falling Weight Deflectometer (FWD) and Plate Load Testing (PLT).
3. Correlations with other material parameters, for example using correlation models with CBR, Resistance R-Value, Dynamic Cone Penetrometer (DCP), Plasticity Index (PI) and gradation, and AASHTO layer coefficient [73].
4. Using approximated values resilient modulus values based on the classification of the soil from pavement management database.

It must be further noted that the resilient modulus values obtained from the first method listed above are the most representative for pavement design. The degree of uncertainty is fairly acceptable for the second method. The accuracy in the third and fourth methods is very doubtful, but still provides an overview for engineering judgement.

Resilient modulus models

Various constitutive models for subgrade soils have been proposed by different researchers (see Table 2.7). The models are based on laboratory testing in which non-linear elastic coefficients and exponents of the constitutive model are determined by using linear and non-linear regression analyses.

Table 2.7: Resilient modulus models for subgrade soils.

Model	Proposed by
$M_R = k_1 + k_3(k_2 - \sigma_d) \quad \sigma_d < k_2$ $M_R = k_1 - k_4(\sigma_d - k_2) \quad \sigma_d > k_2$ Also named as "Bilinear model" Where k_2 is the deviator stress at which the slope of M_R versus σ_d changes. k_1, k_2, k_3 and k_4 are model parameters depending on the type and physical state of the soil.	Thompson and Elliot (1976), as cited by Li & Selig [64].
$M_R = k_5 p_a \left(\frac{\sigma_d}{p_a}\right)^{k_6}$; also named as "Power model" Where k_5 and k_6 are model parameters, σ_d is the deviator stress, and p_a is atmospheric pressure.	Moossazadeh & Witczak (1981), as cited by Drumm *et al.* [34]
$M_R = k_7 p_a \left(\frac{\theta}{p_a}\right)^{k_8} \left(\frac{\sigma_d}{p_a}\right)^{k_9}$; also named as "Universal model", where k_7, k_8 and k_9 are model parameters, θ is the bulk stress, σ_d is the deviator stress, and p_a is atmospheric pressure.	Witczak and Uzan (1988), as cited by Andrei *et al.* [6]
$M_R = k_{10} p_a \left(\frac{\sigma_{oct}}{p_a}\right)^{k_{11}} \left(\frac{\tau_{oct}}{p_a}\right)^{k_{12}}$; also named as "Octahedral stress state model", where k_{10}, k_{11} and k_{12} are model parameters, σ_{oct} is the first stress invariant, τ_{oct} is the deviator stress, and p_a is atmospheric pressure.	Mohammad *et al.* [69]
$M_R = k_{13} p_a \left(\frac{I_1}{p_a}\right)^{k_{14}} \left(\frac{\tau_{oct}}{p_a} + 1\right)^{k_{15}}$; where k_{13}, k_{14} and k_{15} are model parameters, I_1 is the first stress invariant, τ_{oct} is the octahedral shear stress and p_a is atmospheric pressure.	NCHRP [73]

It is evident in Table 2.7 that the models consisting of mean and deviatoric stress components provide better prediction. Since the hydrostatic stress alone does not cause yielding, a material plane called "octahedral plane" can be found where the normal component makes equal angles with each of the principal stress axes. As illustrated in Figure 2.17, for an arbitrary stress tensor (T_{oct}), the normal stress component to the shaded surface (ABC) is called octahedral normal stress (σ_{oct}) and the shear component on the same surface is called octahedral shear stress (τ_{oct}). The octahedral surface is an interest because some materials begin to yield

when the octahedral shear stress reaches a critical value, i.e. the octahedral shear stress of the material. Hence the definition of resilient modulus as a function of the octahedral stress components captures the stress dependency. Mohammad *et al.* [69] reported that the octahedral stress model appears to predict well the resilient modulus of fine-grained subgrade soils. Equations [2.4] and [2.5] show the computation of the octahedral stress components from a generalized non-principal three-dimensional stresses.

$$\sigma_{oct} = \frac{1}{3}(\sigma_{11} + \sigma_{22} + \sigma_{33}) \quad [2.4]$$

$$\tau_{oct} = \frac{1}{3}\left[(\sigma_{11} - \sigma_{22})^2 + (\sigma_{11} - \sigma_{33})^2 + (\sigma_{22} - \sigma_{33})^2 + 6(\tau_{12}^2 + \tau_{13}^2 + \tau_{23}^2)\right]^{1/2} \quad [2.5]$$

Where $\sigma_{11}, \sigma_{22}, \sigma_{33}$ are the normal stress components and $\tau_{12}, \tau_{13}, \tau_{23}$ are the shear stress components for any arbitrary set of coordinate axes in $1-$, $2-$, and $3-$ directions.

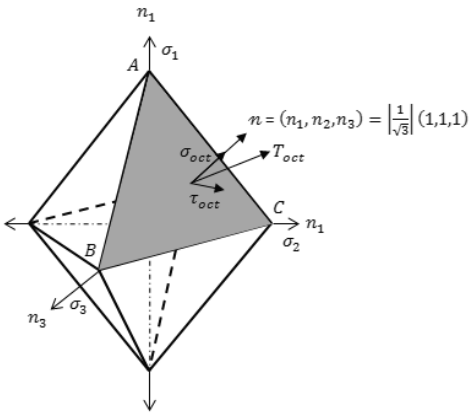

Figure 2.17: Octahedral planes in a principal coordinate system.

Factors affecting the resilient modulus

The desire of using resilient modulus as a design parameter requires understanding of different factors that affect its behaviour. The resilient modulus of subgrade soils depends on the type of soil, load-related and environmental factors. Some of the factors are listed as follows.

a) Water content and dry density

Fine-grained soils exhibit high moisture sensitivity. This is due to the existence of small pores in the soil that create an apparent suction-induced effective stress which will be lost when the soil is saturated. At high water content, the effective contact area of soil grains is reduced, decreasing the resistance of the soil against shear stresses. In coarse-grained subgrade soils, the moisture sensitivity depends on the amount and nature of the fine contents.

Li & Selig [64] studied the effect of water content and dry density on resilient modulus using test data available in literature. The resilient modulus tests were carried out on specimens prepared on two different methods (either constant dry density or constant compactive effort) as shown in Figure 2.18, mainly to evaluate the effect of both water content and dry density. The relationship between the resilient modulus for the constant dry density is presented in Figure 2.19a whereas Figure 2.19b shows the results from constant compactive effort.

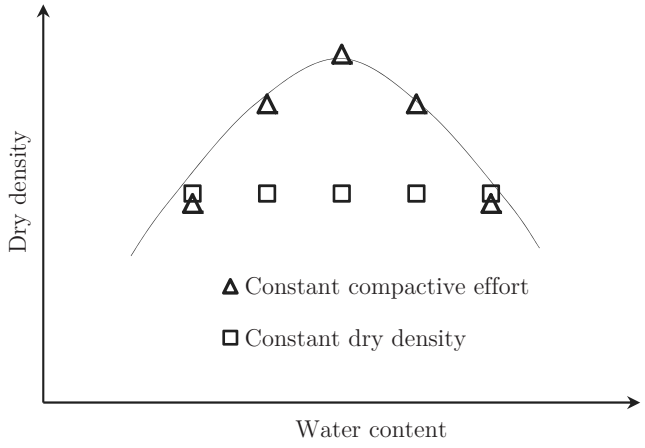

Figure 2.18: Illustration of constant compactive effort and constant dry density. Adapted based on the descriptions by Li & Selig [64].

At low water content, high value of resilient modulus is obtained from both methods. However, for constant compactive effort, a decrease in water content is accompanied by a decrease of dry density, resulting in less increase of resilient modulus [see Figure 2.19b]. In contrary, higher values of resilient modulus were obtained for the same range of water content for the samples prepared with

constant dry density [see Figure 2.19a]. At high water content (above the optimum), an increase of water content results in decrease of dry density for constant compactive effort due to the offsetting influence of dry density on resilient modulus than an increase of water content along the path of constant dry density [64].

It is shown that the increase of water content generally leads to a significant decrease of resilient modulus. For example, in Figure 2.19a, an increase of water content from the 4% below optimum to 4% above optimum (total change of 8%) leads to about 85% reduction of resilient modulus. Another study by Andrei *et al.* [6] showed 50 to 70% reduction in resilient modulus when the water content was increased 3-5% from the optimum conditions. The resilient modulus tends to increase with increasing dry density at lower moisture content and decreases with increasing dry density at higher moisture content.

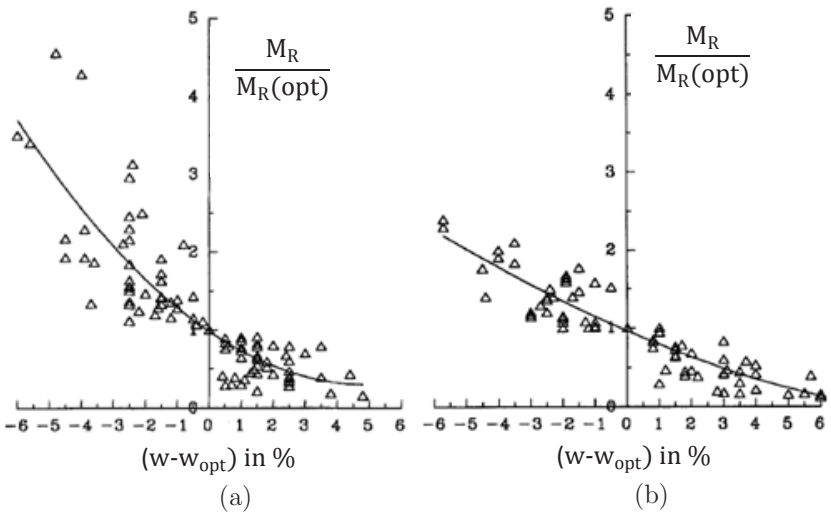

Figure 2.19: Relation between resilient modulus and moisture content a) constant dry density, and b) constant compactive effort [64].

b) Stress level

The resilient modulus of subgrade soils is dependent on the confining pressure and deviator stress. Although the response of the soil primarily depends on the type of the soil and the level of moisture content, the resilient modulus for fine-grained soils was observed to increase when the confining stress is increasing, and decrease when the deviator stress is increasing [28],[108]. For purely cohesive soils, the full strength of the soil is in cohesion, and only increase of deviator stress leads to failure. In this case, the principal stress ratio is not important. For cohesive soils with some friction, the probability of failure increases with increases in either the deviator stress or the principal stress ratio. Therefore, a more rational loading sequence is to decrease both the principal stresses while maintaining a constant deviator stress [6]. This approach was used in the standard method of test for determining resilient modulus of soils [2].

c) Compaction and thixotropy

Soils that are compacted statically have higher resilient modulus that those prepared by kneading compaction. Thixotropy is the phenomenon that describes gaining of strength of the soils which has been lost during remoulding with no change in volume or water content. Soils compacted at high degree of saturation (wet side of optimum water content) exhibited higher strength when the samples are allowed to rest before the test [61].

d) Suction

For unsaturated soils, there exists a relationship between the resilient modulus and moisture suction. Suction controlled laboratory tests [117] indicated that the resilient modulus increases when deviator stress increases for 450kPa initial matric suction. In the contrary, the resilient modulus decreases as the deviator stress increases for low value of initial matric suction, such as 50kPa as shown in Figure 2.20.

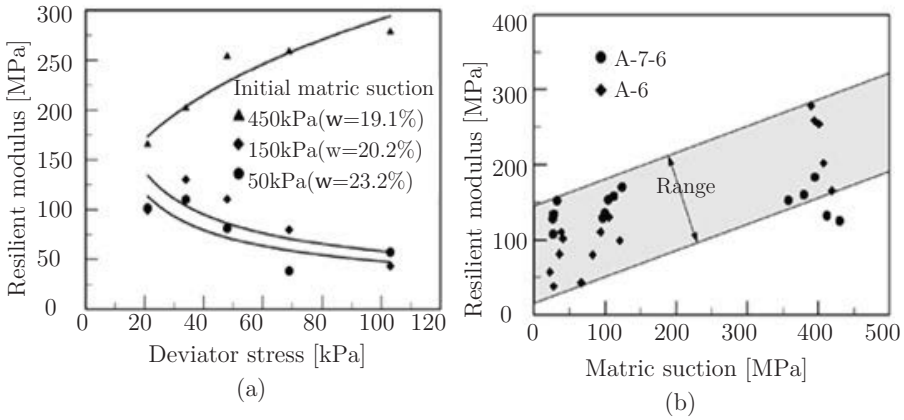

Figure 2.20: Resilient modulus test results a) A-6 [AASHTO classification] soil b) A-7-6 [AASHTO classification] and A-6 soils [117].

Yang *et al.* [117] noted that the resilient modulus obtained by the suction controlled resilient modulus tests are consistent with those obtained by the conventional resilient modulus test. The suction-controlled tests, however, provides better insights that can help in interpreting the test results.

e) Loading frequency

Horvli [47] conducted triaxial tests on undisturbed 54mm diameter clay samples on three different loading frequencies: 0.1Hz, 1Hz, and 10Hz. The resilient modulus, showed dependency on the loading frequency at lower degree of mobilization. In this range, the resilient modulus increases as the loading frequency increases. A fast repetition of loads makes the soil stiffer similar to the behaviour of visco-elastic materials. In the contrary, a unique value of resilient modulus (which is independent of the loading frequency) is obtained when the soil is fully mobilized. When the repeated loading is continued, the soil structure is modified to some extent and the visco-elastic behaviour is diminished. Consequently, at this phase, the resilient modulus exhibits rate-independency. The degree of mobilization of subgrade soils in the field is low. So, the loading frequency can be an important factor in testing of road materials. A loading time of 0.1sec and cycle duration of 1 to 3.1sec is used in the AASHTO standard [2] for determining resilient modulus of soil and aggregate materials. The NCHRP Research Digest [75] recommends 0.1sec loading time followed by a rest period of

0.9sec for base/sub-base materials and 0.2sec loading time followed by a rest period of 0.8sec duration for subgrade soils.

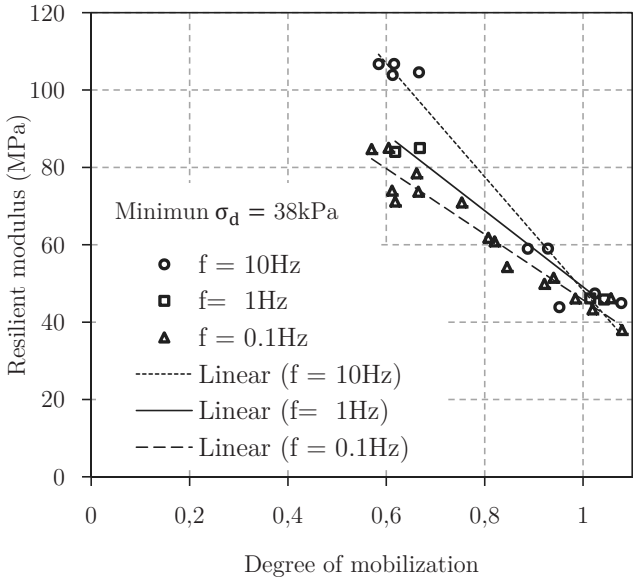

Figure 2.21: Effect of resilient modulus on loading frequency. Adapted from Horvli [47].

2.4.2 Permanent deformation

The subgrade layer is the "foundation" of pavement structures. It deforms under heavy traffic loads and propagates to the overlying pavement structures. Deformation of subgrade soils has two components, namely elastic and plastic. The elastic part is recoverable and accounts for the resilient behaviour. The plastic or permanent deformation is non-recoverable and it accumulates during each load repetition. The deformation mechanisms of coarse-grained soils are governed by rearrangement and/or crushing of particles which lead to frictional sliding and volumetric compaction of particles, and shear deformation. The extent of deformation is affected by the type of compaction, grain-size distribution, grain shape, moisture content and amount of fines [62],[45].

In fine-grained soils such as clay and silt, consolidation and shear deformation are the dominant mode of deformation and their behaviour is affected by the stress history and moisture content for undisturbed soils and on the extent of compaction as well as on the moisture content for compacted cohesive subgrade soils [47],[16],[15],[36],[96],[97].

2.4.3 Permanent deformation models

An abundant experience is obtained on laboratory testing of permanent deformation of pavement materials. However, there is no unique constitutively defined analytical model for estimating the accumulation of permanent strains for subgrade soils. Existing models for prediction of permanent deformation are categorized as empirical/analytical and advanced constitutive models.

a) Empirical/analytical models

Different researchers have used different approaches for the characterization of permanent deformation of subgrade soils in pavements. Existing models are formulated in one of the following methods.

- Modelling of permanent strain and the number of cycles.
- Modelling of permanent strain and stresses.
- Modelling of permanent strain based on shakedown theory.

The first method has been widely used for both subgrade soils and unbound base and sub-base aggregates. The most widely known empirical model in this category is the power model, which is proposed by Monismith *et al.* [70], as shown in Equation [2.6].

$$\varepsilon_{p1(N)} = AN^{b} \qquad [2.6]$$

Where ε_{p1} is the plastic strain in the axial direction, N is the number of load repetitions, A and b are material parameters (regression coefficients from test data).

The exponent b in Equation [2.6] is relatively stable and is mainly dependent on the soil type. Stress state and soil physical state such as density and moisture

content do not significantly change the value of b. Parameter A, on the contrary, depends on the state conditions such as the applied stress, moisture content and density. The benefit of the power model is its simplicity. One of the major limitations of this model is that an explicit form of the stress state is not included. Alternatively, Li & Selig [65] developed an improved model with a reasonable quantification of the influence of the stress state. The extended power model is shown in Equation [2.7] where the effect of the stress is included.

$$\varepsilon_{p1(N)} = a \left(\frac{\sigma_d}{\sigma_s}\right)^m N^b \qquad [2.7]$$

Where σ_d is the deviatoric stress, σ_s is the soil static strength; N is the number of loading repetitions, and a, m, b are material constants depending on the soil type.

With some additional parameters, Chai & Miura [22] presented modification of Li and Selig's model as shown in Equation [2.8]; where σ_{s0} is the initial static deviator stress and a, m, n, b are material constants depending on the soil type. The initial static deviator stress is the calculated stress distribution in the subsoil after a road embankment construction is completed.

$$\varepsilon_{p1(N)} = a \left(\frac{\sigma_d}{\sigma_s}\right)^m \left(1 + \frac{\sigma_{s0}}{\sigma_s}\right)^n N^b \qquad [2.8]$$

Equation [2.9] shows a four-parameter permanent strain model proposed by Puppala *et al.* [97]. This model incorporates the individual effect of confining and deviator stresses.

$$\varepsilon_{p1} = \alpha_1 N^{\alpha_2} \left(\frac{\sigma_{oct}}{P_{ref}}\right)^{\alpha_3} \left(\frac{\tau_{oct}}{P_{ref}}\right)^{\alpha_4} \qquad [2.9]$$

Where $\alpha_1, \alpha_2, \alpha_3$ and α_4 are model constants determined from laboratory tests, σ_{oct} and τ_{oct} are the octahedral normal and shear stresses respectively, and P_{ref} is the reference stress.

The analytical/empirical models are quite simple to apply and they can easily be incorporated in the mechanistic-empirical pavement design methods. The model

proposed by Puppala *et al.* [97] appears to be more realistic since the fundamental stress components for the development of plastic strains, i.e. the effect of mean stress and shear stress is included in the model. However, all models proposed by different researchers appeared to fit the experimental results they derived from — which is a typical feature of empirical models. These models cannot be directly applied to soils other than they are formulated.

In the shakedown theory, a pavement is liable to show progressive accumulation of plastic strains under repeated loading if the magnitude of the applied load exceeds a limiting value (i.e. the shakedown load). Gradually, the pavement goes to an incremental collapse or gradual failure [63]. If the applied load is lower than the shakedown limit, the growth of plastic strains will level off and the pavement is said to have attained a state of shakedown by means of adaptation to the loads. The response of the pavement is then assumed to be totally resilient under additional load applications.

b) Advanced constitutive models

In recent years, finite element modelling techniques and constitutive models have been used for modelling of materials. Particularly, in geotechnical engineering, new modelling concepts based on isotropic and kinematic hardening mechanisms have been used to simulate cyclic loading applications in geo-materials [67],[98]. Such models are, however, appealing to few numbers of loading cycles and very large computation time is required to simulate the repeated load applications similar to traffic loads on pavements. Besides, extensive laboratory tests are required to determine the model parameters.

With the emphasis of pavement design, Bonaquist & Witczak [13] used the flow theory of plasticity theory based on the Drucker-Prager yield criterion to predict the incremental strain. Yesuf & Hoff [121] have proposed a numerical model using the Drucker-Prager yield criterion for the first load cycle, and proximity of deviator stress to static failure limit to predict the amount of incremental plastic strains at each loading cycle. The detail description and development of the constitutive model is presented in Chapter 4.

2.4.4 Factors affecting permanent deformation

The major primary factors that affect the deformation properties of fine-grained soils are moisture content and magnitude of deviator stress. Other factors such as density, confining pressure, duration and frequency of the deviator stress have lesser effect on the permanent deformation as compared to the primary factors.

a) Deviator stress

The accumulation of permanent strains is highly dependent on the deviator stress level, almost for all types of subgrade soils. The proximity of the deviator stress level to the static failure controls the rate at which plastic strain accumulates [72],[30]. There exists distinct stress level (critical level of repeated deviator stress) at which the response of soils behaves differently. Excessive deformation may happen if the applied load exceeds the critical limit. For stress below the critical level, a non-failure equilibrium state is reached after many cycles of repeated loading. The critical stress level generally varies depending on the soil type. It was estimated to be 50% of the static shear strength for Ottawa area Champlain Sea clay [68] and 83% for Mexico City clay soils [32].

The ratio of deviator stress to static strength of the soil is directly related to the apparent shakedown limit [72]. The rate of accumulation of plastic strain increases as the stress ratio level approaches to the apparent shakedown limit (as shown in Figure 2.22). In the unstable regions, very large deformation may occur. The figure also illustrates the rapid change of the shakedown limit in the wet side of optimum moisture content.

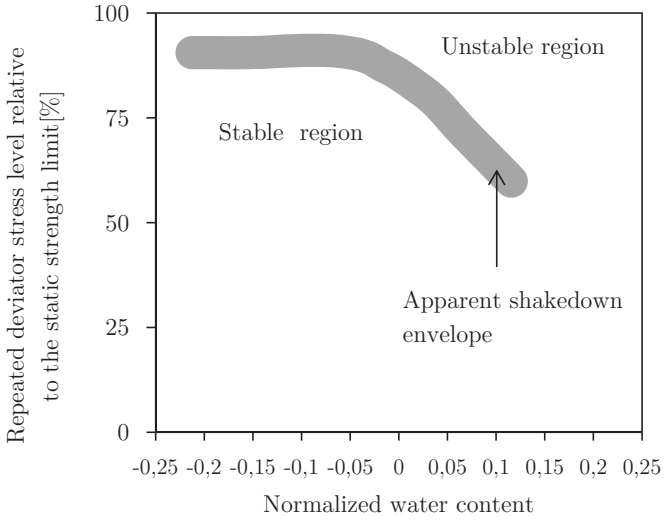

Figure 2.22: Apparent shakedown envelope for compacted A-6 [AASHTO classification] cohesive soil under repeated loading. Adapted from Muhanna *et al.* [72].

b) Loading frequency

Triaxial tests conducted by Seed *et al.* (as cited by Elliott *et al.* [35]) indicated that subgrade soils without thixotropic properties were observed to be independent of the loading frequency (for loading rate within 3 to 20 repetitions per minute) provided that the applied stress is small enough not to change the soil structure and density. Test results [47] on Norwegian subgrade soils (Lade clay) showed that the permanent deformation for 0.1Hz and 10Hz loadings resulted in difference on the plastic strains depending on the degree of mobilization (see Figure 2.23). A pronounced effect of loading frequency on the plastic strains was observed at high degree of mobilization.

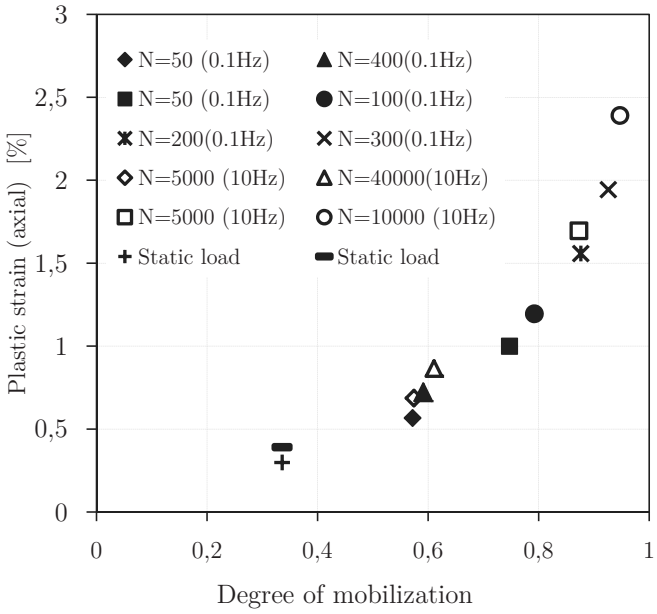

Figure 2.23: Effect of loading frequency on permanent deformation at 0.1Hz and 10Hz on Lade clay soils. Adapted from Horvli [47].

c) Stress history

The effect of stress history on the permanent deformation of fine-grained soils was studied by Brown *et al.* [15]. Based on test results from cyclic triaxial tests (up to 10^6 load cycles), it was observed that permanent deformation is dependent on the over-consolidation ratio, and the rate of increment depends on the confining stress level during the test.

d) Stress rotation

The stress state in pavement layers due to traffic loading varies as the vehicle approaches and departs. In unbound layers, the vertical and horizontal stresses are positive while the shear stress is reversed as the load passes. Considering a small element of soil in the pavement, as the rolling wheel approaches, the horizontal shear stress is the major stress component. At the time when the wheel is directly over the element, the major stress component is the vertical stress and

as the wheel travels away from the element, the major stress component becomes a horizontal shear stress with the opposite sign to the initial shear stress. The effect of principal stress rotation on the permanent deformation of pavement materials is not yet well understood, due to complexity of testing methods for continuous directional change of the principal stresses.

The development of Hollow Cylinder test at the University of Nottingham has provided the possibility to see the effect of stress rotation [23],[43],[17]. Results from large scale rutting tests [23] showed that the permanent vertical deformation of a granular base subjected to a moving wheel load was at least three times higher than the one subjected to a repeated vertical load with the same magnitude. Inam *et al.* [51] reported test results on base-course materials using multi-ring apparatus that cyclic plastic deformation considerably increases due to the rotation of the principal stress axis under repeated axial and shear loading tests. The research emphasis on the effect of stress rotation is mainly for base-course and sub-base aggregates. The extent of rotation of principal stress at the subgrade level is low.

2.5 Chapter summary

The main geotechnical aspects in perspective of flexible pavement design have been presented. Most of the knowledge in this regard is accumulated empirically and qualitatively. Empirical pavement design is still widely used. Most of the efforts, for long time, have been ensuring the quality of road materials during construction. In recent years, the development of mechanistic pavement design methods has attracted the research interest in developing models and use of finite element methods for the analysis and design of flexible pavements. Mechanistic-empirical pavement design method reasonably shows versatility to capture the variation of material parameters, environmental factors and loading conditions. Upon developing new methods for pavement design, the experience and knowledge obtained from empirical methods remains to be an important ingredient, providing an in-depth view how different factors affect the design parameters.

Chapter 3

Numerical implementation of nonlinear resilient modulus model

This chapter discusses the stresses and strains in flexible pavements. First, the stresses and critical stains considered in mechanistic-empirical pavement design method are discussed in section 3.1. Section 3.2 deals with the applications of finite element method for analysis of pavement structures. In section 3.3, a method to implement a nonlinear subgrade model is introduced and its implication on the computation of stresses and critical strains is briefly discussed. Finally, section 3.4 summarises of the main points of this chapter.

3.1 Stresses and strains in pavements

Stress (in mechanics) is a physical quantity. It measures the extent of the internal forces when neighbouring particles of a continuous material exert force on each other. Particularly in flexible pavements, the distribution of stresses depends on the relative stiffness of each layer. The highest magnitude of stress from a traffic load is obtained on the surface of the pavement. The stress, then, reduces at the subgrade level due to stiffer overlying layers and distribution of pressure from the load over a large area as the depth increases. A very important aspect of stress analysis in pavement is, hence, *how to measure it in each layer?*

Previously, the Boussinesq's equations were the commonly used analytical methods for computing stresses and deformations in elastic half-space composed

of homogeneous, isotropic and linear elastic material. Since a typical pavement section consists of different materials, Burmister ([20],[19],[18]) presented analytical solutions for multi-layered systems, overcoming the limitations of Boussinesq's method. Alternatively, the equivalent thickness method (also known as the Odemark's method), provides an approximate solution of stresses, strains and displacements of multi-layered systems. This method converts multi-layers into one layer (equivalent thickness).

The multi-layer stress analysis methods based on analytical methods are only approximate solutions. Moreover, they impose limitations on nonlinear analysis methods and different loading and boundary conditions. Finite element modelling is the commonly used method to alleviate the limitations of analytical solutions.

3.2 Finite element method (FEM)

Nowadays, FEM is widely used for stress and strain analyses of many engineering applications. The concepts, development and applications of FEM are available elsewhere in literature (e.g. [27],[31],[102]). In this particular study, only the prevailing concepts and methods related to the analysis of pavement structures are presented. In the mechanistic-empirical pavement design method, the linear elastic material model is often used to obtain stress distribution and the associated strains for a standard axle load. The constitutive relation of stress-strain equation of a linear elastic material is expressed by Equation [3.1].

$$\sigma_{ij} = D_{ijkl} \cdot \varepsilon_{kl} \qquad [3.1]$$

Where σ_{ij} is the stress tensor, ε_{kl} is the strain tensor, and D_{ijkl} is the stiffness matrix.

D_{ijkl} is a fourth order tensor with 81 independent elastic constants, and σ_{ij} and ε_{kl} are symmetric tensors. Owing to the symmetry of σ_{ij} and ε_{kl}, the stiffness matrix has minor symmetries where $D_{ijkl} = D_{jikl} = D_{ijlk}$. Then, the number of unknowns reduces from 81 to 36. Considering a major symmetry, i.e. $D_{ijkl} = D_{klij}$, the number of unknowns reduces again from 36 to 21. A special case of isotropic materials remains with only two unknowns, namely the Young's modulus (E) and Poisson's ratio (ν). Then, the generalized constitutive equation (in index notation) relating the elastic stress to elastic strain is shown in Equation [3.2].

$$\sigma_{ij} = \frac{E}{1+\upsilon}\left(\frac{\nu}{1-2\upsilon}\varepsilon_{kk}\mathbf{I} + \varepsilon_{ij}\right) \quad [3.2]$$

Where σ_{ij} and ε_{ij} are the components of stress and strain tensor respectively, E is the Young's modulus, ν is the Poisson's ratio, $\varepsilon_{kk} = \varepsilon_v$ is the volumetric strain, and $\mathbf{I}$ is identity tensor.

In mechanistic-empirical pavement design, the pavement response is evaluated at different locations along the depth of the pavement section as discussed in Section 2.1.2. The most commonly used design criteria are the horizontal tensile stain at bottom of the asphalt layer and the vertical compressive strain on the top of the subgrade.

3.3 Nonlinear resilient modulus of subgrade soil

The common practice in mechanistic-empirical pavement design is to consider a constant material stiffness for each layer in pavements based on the linear-elastic model. Though this method appears appealing compared to empirical methods, the actual material behaviour is not captured, especially for increased traffic loads. The elastic stiffness of subgrade soils is often obtained from resilient modulus testing. Laboratory tests on subgrade soils have showed dependency of resilient modulus on stress level as discussed in Section 2.4.1. In the following section, a stress-dependent constitutive model is formulated for subgrade soils and the implications on practical pavement design are presented.

3.3.1 Formulation of nonlinear numerical model

The bilinear subgrade model proposed by Thompson and Elliot (as cited by Li & Selig [64]) (refer Table 2.7 in Chapter 2) has been used to incorporate the nonlinear behaviour of subgrade soils [40],[58]. The bilinear model considers mainly the effect of deviator stress and this constitutive relationship does not represent the behaviour of wide range of subgrade soils. The "Octahedral stress state model" shown in Table 2.7 was found to be capable of predicting the

nonlinear resilient modulus of fine-grained soils [69],[95]. The is presented in Equation [3.3].

$$M_R(\sigma_{oct}, \tau_{oct}) = k_1 p_a \left(\frac{\sigma_{oct}}{p_a}\right)^{k_2} \left(\frac{\tau_{oct}}{p_a}\right)^{k_3} \quad [3.3]$$

Where k_1, k_2 and k_3 are material constants, p_a is the reference pressure, σ_{oct} is the octahedral normal stress, and τ_{oct} is the octahedral shear stress.

The nonlinear behaviour of road materials, particularly for granular materials has been widely studied elsewhere (e.g. [44],[58],[105],[76]). In this study, the numerical implementation technique based on consistent tangent stiffness from Taciroglu [105] is adopted. The formulation of the nonlinear modulus is based on the Octahedral stress model referred in Equation [3.3] and the definition of octahedral strain invariants is consistent with Chen & Han [25] (*Chapter 3: p. 129*). The generalized constitutive equation relating the elastic stress to elastic strain has been shown in Equation [3.2]. Substituting E by M_R, Equation [3.4] is obtained.

$$\sigma_{ij} = \frac{M_R}{1+\nu}\left(\frac{\nu}{1-2\nu}\varepsilon_{kk}\mathbf{I} + \varepsilon_{ij}\right) \quad [3.4]$$

Considering $\widetilde{M}_r = M_r(\sigma_{oct}, \tau_{oct})/(1+\upsilon)$, Equation [3.4] is rewritten as:

$$\sigma_{ij} = \widetilde{M}_R\left(\frac{\upsilon}{1-2\upsilon}\varepsilon_v\mathbf{I} + \varepsilon_{ij}\right) \quad [3.5]$$

For a given load increment, the stress state is obtained from the nonlinear function in Equation [3.6] by solving the roots for $g(\sigma_{ij}) = 0$.

$$g(\sigma_{ij}) = \sigma_{ij} - \widetilde{M}_R\left(\frac{\nu}{1-2\nu}\varepsilon_v\mathbf{I} + \varepsilon_{ij}\right) \quad [3.6]$$

Where $g(\sigma_{ij})$ is a nonlinear function which needs numerical iteration to converge.

It is illustrated in Figure 3.1 that for each load step, a number of iterations are required so that the solution converges at point A where the actual stress is equal to the predicted stress. So, the formulation of consistent tangent modulus must ensure the convergence of the solution in a few iterations.

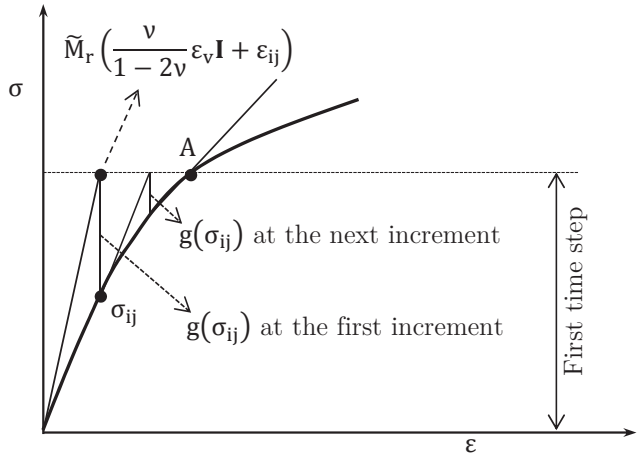

Figure 3.1: Iterations to converge at each incremental stress.

Decomposing Equation [3.6] into bulk and deviatoric parts, i.e. $g^{dev} = g - 1/3(tr\, g)\mathbf{I}$, where $tr\, g = 0$ and $g^{dev} = 0$ are considered to satisfy the condition $g(\sigma_{ij}) = 0$. Consequently, the expressions in Equation [3.7] are obtained.

$$p = \bar{\nu}\widetilde{M}_R(\sigma_{oct}, \tau_{oct})\varepsilon_v\,; \quad \bar{\nu} = \frac{\nu}{1-2\nu} + \frac{1}{3} = \frac{1+\nu}{3(1-2\nu)}$$

$$\sigma_{ij}^{dev} = \widetilde{M}_R(\sigma_{oct}, \tau_{oct})\varepsilon_{ij}^{dev} \qquad [3.7]$$

The octahedral shear strain and octahedral shear stress can alternatively be presented in Equation [3.8].

$$\gamma_{oct}^2 = \frac{1}{3}tr\left[\left(\varepsilon_{ij}^{dev}\right)^2\right] = \frac{4}{3}\varepsilon_{ij}^{dev}\varepsilon_{ij}^{dev}$$

$$\tau_{oct}^2 = \frac{1}{3}tr\left[\left(\sigma_{ij}^{dev}\right)^2\right] = \frac{1}{3}\sigma_{ij}^{dev}\sigma_{ij}^{dev} \qquad [3.8]$$

The conditions that fulfil $tr\,\mathrm{g} = 0$ are also valid for $tr\left[\left(\mathrm{g}^{\mathrm{dev}}\right)^2\right] = 0$. Hence, the octahedral stress components in Equation [3.9] are derived.

$$\begin{aligned}\sigma_{oct} &= \overline{\alpha}\widetilde{M}_R(\sigma_{oct},\tau_{oct})|\varepsilon_v| \\ \tau_{oct} &= \widetilde{M}_R(\sigma_{oct},\tau_{oct})\frac{\gamma_{oct}}{2}\end{aligned} \qquad [3.9]$$

Substituting Equation [3.3] to Equation [3.9], the octahedral stresses are defined in Equation [3.10].

$$\begin{aligned}\sigma_{oct} &= \overline{\nu}\frac{1}{1+\nu}k_1 p_a\left(\frac{\sigma_{oct}}{p_a}\right)^{k_2}\left(\frac{\tau_{oct}}{p_a}\right)^{k_3}|\varepsilon_v| \\ \tau_{oct} &= \frac{1}{1+\nu}k_1 p_a\left(\frac{\sigma_{oct}}{p_a}\right)^{k_2}\left(\frac{\tau_{oct}}{p_a}\right)^{k_3}\frac{\gamma_{oct}}{2}\end{aligned} \qquad [3.10]$$

From the ratio of the octahedral normal stress to octahedral shear stress in Equation [3.10], we get $\sigma_{oct} = (2\overline{\upsilon}|\varepsilon_v|\tau_{oct})/\gamma_{oct}$ and $\tau_{oct} = (\sigma_{oct}\gamma_{oct})/(2\overline{\upsilon}|\varepsilon_v|)$. These expressions are substituted again in Equation [3.10] to obtain the expressions in Equation [3.11].

$$\begin{aligned}\sigma_{oct} &= \left[\frac{k_1}{1+\nu}\,\frac{(2\overline{\upsilon}|\varepsilon_v|)^{1-k_3}(\gamma_{oct}/2)^{k_3}}{p_a^{k_2+k_3-1}}\right]^{\frac{1}{1-k_2-k_3}} \\ \tau_{oct} &= \left[\frac{k_1}{2(1+\nu)}\,\frac{(2\overline{\upsilon}|\varepsilon_v|)^{k_2}(\gamma_{oct})^{1-k_2}}{p_a^{k_2+k_3-1}}\right]^{\frac{1}{1-k_2-k_3}}\end{aligned} \qquad [3.11]$$

Substituting Equation [3.11] in Equation [3.3], and defining $\mu = \frac{1}{1-k_2-k_3}$, Equation [3.12] is obtained where the resilient modulus is defined as a function strain components.

$$M_R(\sigma_{oct},\tau_{oct}) = \widehat{M}_R(\varepsilon_v,\gamma_{oct}) = \left[\frac{k_1(\overline{\nu}|\varepsilon_v|)^{k_2}(\gamma_{oct}/2)^{k_3}}{(1+\nu)^{k_2+k_3}\;p_a{}^{k_2+k_3-1}}\right]^{\mu} \qquad [3.12]$$

Where $\widehat{M}_R$ represents the resilient modulus as a function of the strain components.

Defining $\bar{M}_R = \widehat{M}_R(\varepsilon_v, \gamma_{oct})/(1+\nu)$, the stress-strain constitutive relationship is rewritten in Equation [3.13].

$$\sigma_{ij} = \frac{\widehat{M}_r(\varepsilon_v, \gamma_{oct})}{1+\nu}\left(\frac{\nu}{1-2\nu}\varepsilon_v \mathbf{I} + \varepsilon_{ij}\right) = \bar{M}_R(\varepsilon_{ij})\left(\nu\varepsilon_v \mathbf{I} + \varepsilon_{ij}\right) \quad [3.13]$$

The material tangent stiffness (Equation [3.13]) can be directly obtained from partial derivative of the stress tensor with respect to the strain tensor. In this case, the stiffness is measured from small increments of stress and strain. Hence, a unique value of stiffness is obtained at different stress states.

$$\frac{\partial \sigma_{ij}}{\partial \varepsilon_{ij}} = \bar{M}_R\left(1 + \frac{\nu}{1-2\nu}\mathbf{I} \otimes \mathbf{I}\right) + \left(\bar{\nu}\varepsilon_v \mathbf{I} + \varepsilon_{ij}\right) \otimes \nabla_{\varepsilon_{ij}} \bar{M}_R \quad [3.14]$$

And,

$$\nabla_{\varepsilon_{ij}} \bar{M}_R(\varepsilon_{ij}) = \frac{\partial \bar{M}_R}{\partial |\varepsilon_v|}\frac{\partial |\varepsilon_v|}{\partial \varepsilon_{ij}} + \frac{\partial \bar{M}_R}{\partial \gamma_{oct}}\frac{\partial \gamma_{oct}}{\partial \varepsilon_{ij}} \quad [3.15]$$

Noting that $\varepsilon_v = tr(\varepsilon_{ij})$; $\partial \mathrm{tr}(\varepsilon_{ij})/\partial \varepsilon_{ij} = \mathbf{I}$; and $\gamma_{oct}^2 = \frac{4}{3}\varepsilon_{ij}^{dev}\varepsilon_{ij}^{dev}$

$$\frac{\partial |\varepsilon_v|}{\partial \varepsilon_{ij}} = \frac{\partial |\varepsilon_v|}{\partial \varepsilon_v}\frac{\partial \varepsilon_v}{\partial \varepsilon_{ij}} = sgn(\varepsilon_v)\mathbf{I}\,; \quad \frac{\partial \gamma_{oct}}{\partial \varepsilon_{ij}} = \frac{4}{3}\frac{\varepsilon_{ij}^{dev}}{\gamma_{oct}} \quad [3.16]$$

Where sgn represents the sign of the volumetric strain: $sgn(\varepsilon_v)$= -1 if ε_v<0, $sgn(\varepsilon_v)$= 1 if ε_v>0.

Substituting the expressions in Equation [3.16] into Equation [3.15] and observing that $|\varepsilon_v| * sgn(\varepsilon_v) = \varepsilon_v$:

$$\nabla_{\varepsilon_{ij}} \bar{M}_R(\varepsilon_{ij}) = \mu \bar{M}_R\left(\frac{k_2}{\varepsilon_v}\mathbf{I} + \frac{4k_3}{3\gamma_{oct}^2}\varepsilon_{ij}^{dev}\right) \quad [3.17]$$

Substituting Equation [3.17] into Equation [3.14],

$$\frac{\partial \sigma_{ij}}{\partial \varepsilon_{kl}} = \bar{M}_R\left(1+\frac{\nu}{1-2\nu}\mathbf{I}\otimes\mathbf{I}\right)+\left(\frac{\nu}{1-2\nu}\varepsilon_v\mathbf{I}+\varepsilon_{kl}\right)\otimes\ \mu\bar{M}_R\left(\frac{k_2}{\varepsilon_v}\ \mathbf{I}+\frac{4k_3}{3\gamma_{oct}^2}\varepsilon_{kl}^{dev}\right)$$

$$= \bar{M}_R\Big[1+\tfrac{\nu}{1-2\nu}\mathbf{I}\otimes\mathbf{I}+\tfrac{\nu}{1-2\nu}\varepsilon_v\mathbf{I}\otimes\mu\tfrac{k_2}{\varepsilon_v}\ \mathbf{I}\ +\tfrac{\upsilon}{1-2\upsilon}\varepsilon_v\mathbf{I}\otimes\mu\tfrac{4k_3}{3\gamma_{oct}^2}\varepsilon_{kl}^{dev}+ \varepsilon_{kl}\otimes\mu\tfrac{k_2}{\varepsilon_v}\ \mathbf{I}+\varepsilon_{kl}\otimes\mu\tfrac{4k_3}{3\gamma_{oct}^2}\varepsilon_{kl}^{dev}\Big]$$

$$= \bar{M}_R\left[1+\frac{\nu}{1-2\nu}\mathbf{I}\otimes\mathbf{I}+\frac{\nu}{1-2\nu}\varepsilon_v\mathbf{I}\otimes\mu\frac{k_2}{\varepsilon_v}\ \mathbf{I}\ +\frac{\upsilon}{1-2\upsilon}\varepsilon_v\mathbf{I}\otimes\mu\frac{4k_3}{3\gamma_{oct}^2}\varepsilon_{kl}^{dev}\right.$$
$$\left.+({\varepsilon_{kl}}^{dev}\ +\ \frac{1}{3}\varepsilon_v\mathbf{I})\otimes\mu\frac{k_2}{\varepsilon_v}\ \mathbf{I}+({\varepsilon_{kl}}^{dev}+\frac{1}{3}\varepsilon_v\mathbf{I})\otimes\mu\frac{4k_3}{3\gamma_{oct}^2}\varepsilon_{kl}^{dev}\right] \qquad [3.18]$$

$$= \bar{M}_R\Big[1+\tfrac{\nu}{1-2\upsilon}\mathbf{I}\otimes\mathbf{I}+\tfrac{\nu}{1-2\upsilon}\varepsilon_v\mathbf{I}\otimes\mu\tfrac{k_2}{\varepsilon_v}\ \mathbf{I}\ +\tfrac{\nu}{1-2\nu}\varepsilon_v\mathbf{I}\otimes\mu\tfrac{4k_3}{3\gamma_{oct}^2}\varepsilon_{kl}^{dev}+ {\varepsilon_{kl}}^{dev}\otimes\mu\tfrac{k_2}{\varepsilon_v}\ \mathbf{I}+\tfrac{1}{3}\varepsilon_v\mathbf{I}\otimes\mu\tfrac{k_2}{\varepsilon_v}\ \mathbf{I}\ +{\varepsilon_{kl}}^{dev}\otimes\mu\tfrac{4k_3}{3\gamma_{oct}^2}\varepsilon_{kl}^{dev}+\ \tfrac{1}{3}\varepsilon_v\mathbf{I}\otimes\mu\tfrac{4k_3}{3\gamma_{oct}^2}\varepsilon_{kl}^{dev}\Big]$$

Rearranging the last expression in Equation [3.18] and recalling a previous definition, $\bar{\nu}=\frac{\nu}{1-2\nu}+\frac{1}{3}$, we finally get Equation [3.19], where the consistent tangent stiffness is defined as a function of strain invariants.

$$\frac{\partial \sigma_{ij}}{\partial \varepsilon_{kl}} = \bar{M}_R\left[1+\left(\mu k_2\bar{\nu}\ +\frac{\nu}{1-2\nu}\right)(\mathbf{I}\otimes\mathbf{I})+\left(\bar{\nu}\,\varepsilon_v\mu\frac{4k_3}{3\gamma_{oct}^2}\right)\left(\mathbf{I}\otimes\varepsilon_{kl}^{dev}\right)\right.$$
$$\left.+\left(\mu\frac{k_2}{\varepsilon_v}\right)({\varepsilon_{kl}}^{dev}\otimes\ \mathbf{I})\ +\left(\mu\frac{4k_3}{3\gamma_{oct}^2}\right)(\ \varepsilon_{kl}^{dev}\otimes\ \varepsilon_{kl}^{dev})\right] \qquad [3.19]$$

There might be a question that why this long and cumbersome mathematical derivation is required when we can simply define the stiffness as a function of stress. The answer will be straightforward. In numerical modelling of finite element analysis, a small increment of strain is assumed first, and then the stress increment is computed. If a proper consistent tangent modulus is not used, the solution may not converge. For numerical analysis of nonlinear resilient modulus of subgrade soils, Equation [3.19] ensures that the solution converges for traffic load applications.

3.3.2 Determination of parameters

The coefficients of the resilient modulus model in Equation [3.3] are obtained using multiple regression analysis. Assuming a linear function of a dependent variable (y) and explanatory variables $(x_1, x_2, x_3 \dots x_n)$, the expression in Equation [3.20] is obtained.

$$y_i = a_0 + a_1 x_{i1} + a_2 x_{i2} + \cdots + a_n x_{in} + \xi_i \qquad [3.20]$$

For m observations of one dependent variable and n independent variables, y_i is the i^{th} observation of the dependent variable and x_{ij} is the i^{th} observation of the j^{th} independent variable where $j = 1,2,3, \dots, n$. The values a_j represent the parameters to be estimated. ξ_i is the i^{th} independent identically distributed normal error. To obtain the coefficients $a_0, a_1, a_2 \dots a_n$, the overall difference (Q) between the tested y_i values and the predicted y values is kept to minimum as shown in Equations [3.21] and [3.22].

$$Q = \sum_{j=1}^{n} \left[y_i - \left(a_0 + a_1 x_{1j} + a_2 x_{2j} + \cdots + a_n x_{mj} \right) \right]^2 \qquad [3.21]$$

$$\frac{\partial Q}{\partial a_i} \equiv 0 \; ; \; i = 0,1,2, \cdots, n \qquad [3.22]$$

Then,

$$\frac{\partial Q}{\partial a_0} = \sum_{j=1}^{n} 2 * \left[y_i - \left(a_0 + a_1 x_{1j} + a_2 x_{2j} + \cdots + a_n x_{nj} \right) \right] * (-1) \equiv 0$$

$$\text{for } k = 0$$

$$\frac{\partial Q}{\partial a_k} = \sum_{j=1}^{n} 2 * \left[y_i - \left(a_0 + a_1 x_{1j} + a_2 x_{2j} + \cdots + a_n x_{nj} \right) \right] * \left(-x_{kj} \right) \equiv 0 \qquad [3.23]$$

$$\text{for } k = 1,2, \cdots, n$$

Solving Equation [3.23], Equation [3.24] is formulated.

$$A^T A \begin{bmatrix} a_0 \\ a_1 \\ \vdots \\ a_n \end{bmatrix} = A^T \begin{bmatrix} y_1 \\ y_2 \\ \vdots \\ y_j \end{bmatrix}; \qquad A = \begin{bmatrix} 1 & x_{11} & x_{21} & \cdots & x_{j1} \\ 1 & x_{12} & x_{22} & \cdots & x_{j2} \\ \vdots & \vdots & \vdots & & \vdots \\ 1 & x_{1n} & x_{21} & \cdots & x_{jn} \end{bmatrix} \quad [3.24]$$

The confidence in the coefficients is obtained from linear regression in Equation [3.25].

$$R^2 = 1 - \frac{Q}{\sum_{i=1}^{n} \left(y_i - \frac{1}{n} \sum_{i=1}^{n} y_i \right)^2} \quad [3.25]$$

The model expressed in Equation [3.3] has to be transferred into a linear equation in order to apply a linear regression analysis. Equation [3.26] shows the linearization process by using a logarithmic function for the i^{th} resilient modulus test.

$$\log(M_{R,i}) = \log(k_1 p_a) + k_2 \log\left(\frac{\sigma_{oct,i}}{p_a}\right) + k_2 \log\left(\frac{\tau_{oct,i}}{p_a}\right) \quad [3.26]$$

Relating Equation [3.26] and Equation [3.20], and we get:

$$y_i = \log(M_{R,i}); \; a_0 = \log(k_1 p_a); \; a_1 = k_2; \; a_2 = k_3 \quad [3.27]$$

Then, the values of model coefficients are obtained using Equation [3.24].

$$A^T A \begin{bmatrix} \log(k_1 p_a) \\ k_2 \\ k_3 \end{bmatrix} = A^T \begin{bmatrix} \log(M_{R,1}) \\ \log(M_{R,2}) \\ \vdots \\ \log(M_{R,n}) \end{bmatrix} \quad [3.28]$$

$$A = \begin{bmatrix} 1 & \log\left(\frac{\sigma_{oct,1}}{p_a}\right) & \log\left(\frac{\tau_{oct,1}}{p_a}\right) \\ 1 & \log\left(\frac{\sigma_{oct,2}}{p_a}\right) & \log\left(\frac{\tau_{oct,2}}{p_a}\right) \\ \vdots & \vdots & \vdots \\ 1 & \log\left(\frac{\sigma_{oct,n}}{p_a}\right) & \log\left(\frac{\tau_{oct,n}}{p_a}\right) \end{bmatrix} \quad [3.29]$$

For numerical analysis using the newly implemented consistent tangent stiffness (Equation [3.19]), the coefficients of the octahedral stress model are obtained from experimental data of silty clay soil reported by Mohammad *et al.* [69]: $k_1 = 1585.0, k_2 = 0.47, k_3 = -0.24$ (optimum moisture content, 15.2%; dry density 1819kg/m^3; and regression of data $R^2 = 0.99$).

3.3.3 Numerical implementation, results and discussions

Equation [3.19] comprises well-structured tensor products and scalar quantities — it can easily be implemented in the numerical constitutive model to update the material stiffness (or Jacobian in Abaqus FEA/UMAT). Four parameters are required to define the nonlinear elastic model, namely Poisson's ratio (ν), and material constants k_1, k_2, k_3 to define Equation [3.19]. Since the effect of variation of subgrade stiffness on the horizontal strain beneath the asphalt layer is insignificant, the nonlinear behaviour of subgrade layer in this study is emphasized only on the vertical elastic strain on the top of the subgrade layer. A single axisymmetric element (Abaqus designation: CAX8 - 8-node bilinear axisymmetric quadrilateral) shown in Figure 3.2 is used for the numerical analyses to verify the nonlinear elastic constitutive model.

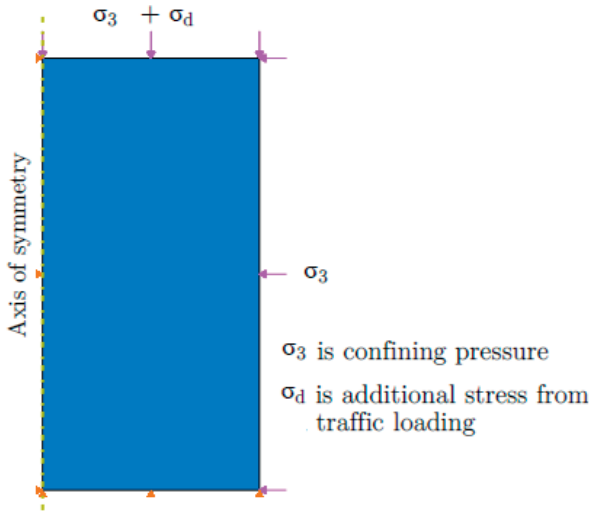

Figure 3.2: Loading on a single axisymmetric element.

The vertical elastic strains obtained from linear elastic and nonlinear elastic models are presented in Figure 3.3. For a confining pressure of 20kPa, the stiffness at different levels of additional vertical stresses is computed using the nonlinear model with model parameters obtained from Mohammad *et al.* [69]: $k_1 = 1585.0, k_2 = 0.47, k_3 = -0.24$. Then, different values of resilient modulus are obtained at different deviator stress levels, i.e. 190MPa at 5kPa; 166MPa at 10kPa; 150MPa at 20kPa; 141MPa at 40kPa. A linear elastic analysis is carried out using each resilient modulus value. The nonlinear model developed in this study is used for the same load applications similar to the linear elastic analysis and the validation is shown in Figure 3.3.

As can be seen in Figure 3.3, the effect of nonlinearity is prominent when the stress level increases. It is shown that the nonlinear model is versatile to capture the strain corresponding to the actual stiffness at a particular stress level. To illustrate the implication of subgrade nonlinearity for practical pavement design methods, a case study is presented on axisymmetric multilayer pavement structure (shown in Figure 3.4).

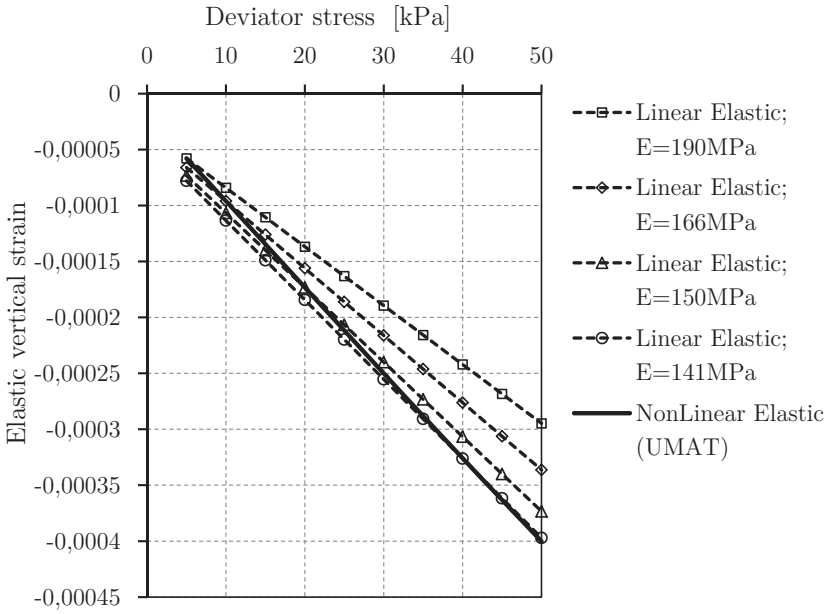

Figure 3.3: Comparison of linear and nonlinear subgrade stiffness.

A circular contact area with radius 13.3cm is obtained from maximum allowed tire pressure of 900kPa and maximum allowable axle load of 100kN (in Norway). A linear elastic model is assumed for the asphalt layer, base course, and subbase layer (asphalt layer E=3000MPa, ν=0.35; base course: E=500MPa, ν=0.35; subbase: E=200MPa, ν=0.35). The nonlinear elastic model parameters for the subgrade are: ν=0.4, k_1=1585.0, k_2=0.47, k_3=-0.24. For the linear elastic model an average secant stiffness (E=150MPa) is assumed. The base course and subbase thickness is kept constant, and two different thickness of the AC layer are used. To simulate the high-traffic volume road section, 15cm-thick asphalt layer is modelled, and for the case of low-traffic volume road section, a 4cm-thick asphalt is considered.

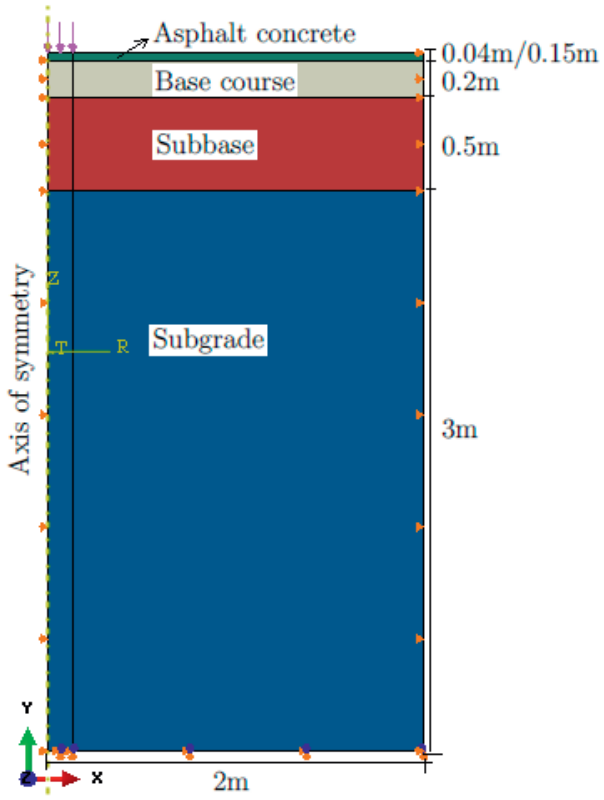

Figure 3.4: Axisymmetric multi-layer geometry.

Contour plots of the stress, and strain distribution for both nonlinear elastic and linear elastic models in the subgrade layer are presented in Figures 3.5 and 3.6. The stress predicted from nonlinear elastic model is lower than the stress predicted from linear elastic model. The difference is high at the proximity of the centre of traffic loading and reduces both widthwise and along the depth (compare Figure 3.5a and Figure 3.5b for the analysis of low-traffic volume road section and Figure 3.6a and Figure 3.6b for high-traffic volume road section). The increase in subgrade stiffness results in a more "rigid" foundation. Hence, the vertical stress in the subgrade increases while the vertical strain decreases. In the contrary, when the subgrade stiffness is reduced, the subgrade, literally, acts like a "flexible" layer. This scenario facilitates stress mobilization in the upper layers (unbound base and subbase), which leads to a reduced stress at the subgrade level.

3.3 Nonlinear resilient modulus of subgrade soil

In fine-grained soils, the resilient modulus decreases as the deviator stress increases. When nonlinear elastic model is used, the tangent stiffness near the top of the subgrade (and at the proximity of centre of loading) is low since the region has relatively high deviator stress due to the additional traffic loading. As explained above, the predicted stress will be lower and the strain will be higher in employing nonlinear elastic model as compared to the simple linear elastic analysis. Table 3.1 shows the comparison of the pavement response on the top of the subgrade layer. The deviation of the computed strains from the two methods is higher than the deviation of the computed stresses. Hence, an improved design analogy is obtained by using nonlinear elastic models as far as the vertical elastic strain criterion is used to limit rutting in flexible pavement design.

Table 3.1: Comparison of the pavement response on the top of subgrade for linear elastic and nonlinear elastic analyses.

Response	Asphalt thickness [mm]	Linear elastic	Nonlinear elastic
Vertical elastic strain on top of subgrade [-]	40	-188.0×10^{-6}	-270.0×10^{-6}
	150	-121.0×10^{-6}	-173.0×10^{-6}
Vertical stress on top of subgrade [kPa]	40	-28.4	-22.0
	150	-18.7	-14.4

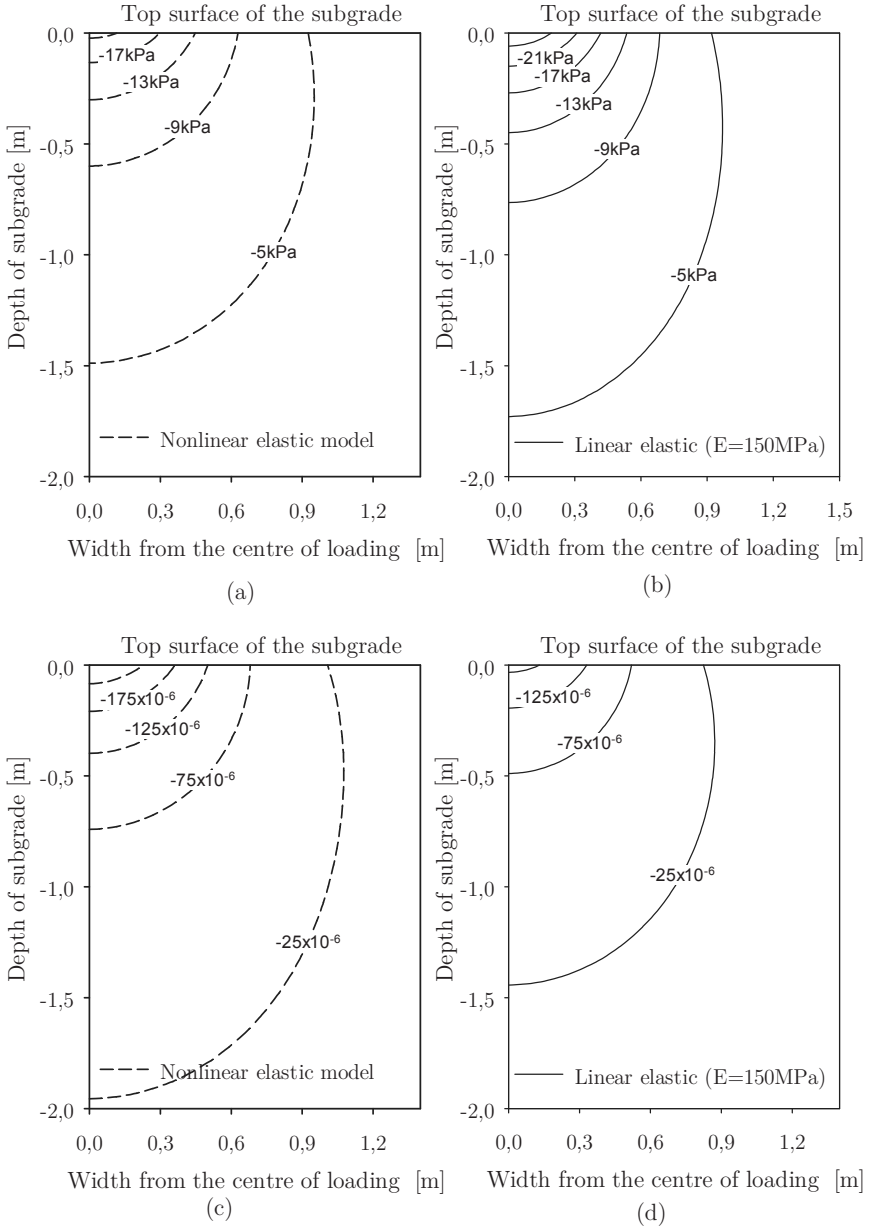

Figure 3.5: Response of low-traffic volume road section (AC thickness=40mm): a) vertical elastic strain distribution, b) vertical stress distribution, c) vertical elastic strain distribution, and d) vertical stress distribution.

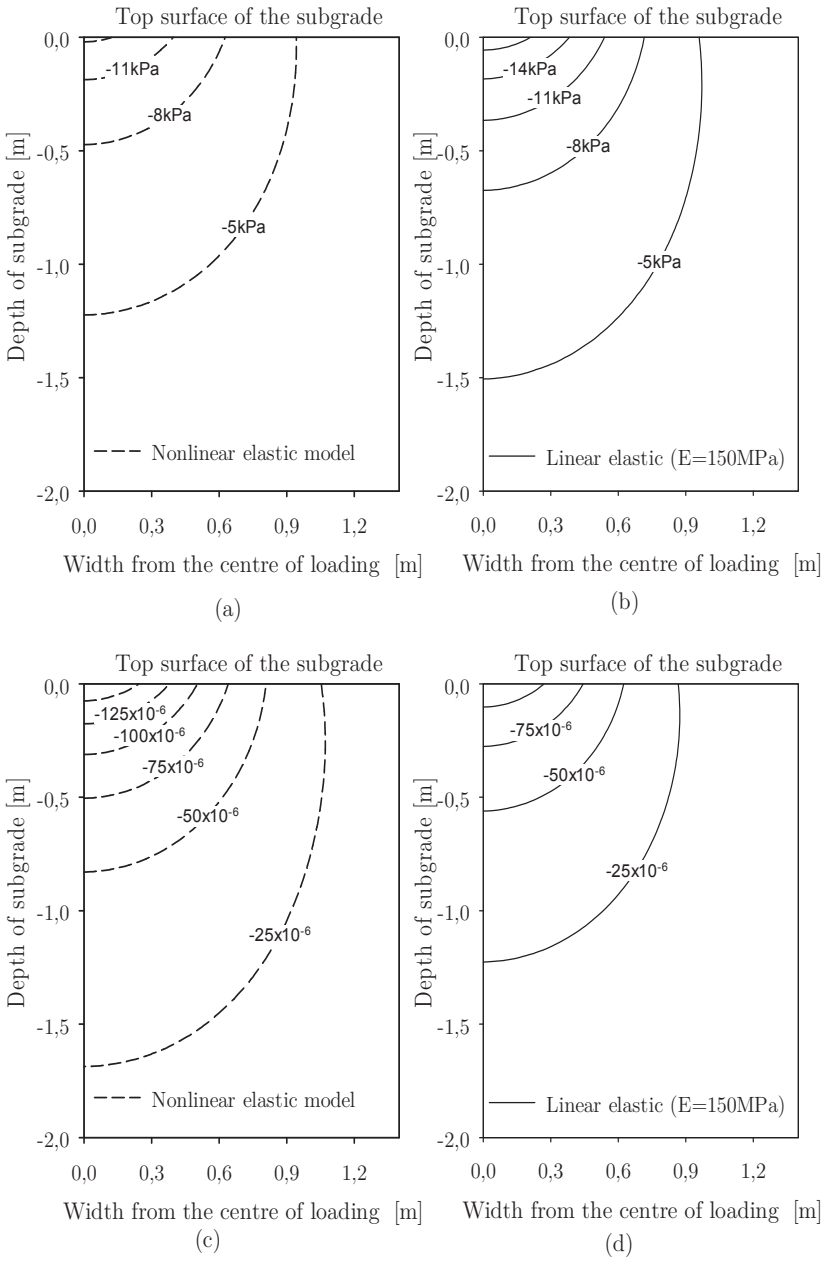

Figure 3.6: Response of high-traffic volume road section (AC thickness=150mm): a) vertical elastic strain distribution, b) vertical stress distribution, c) vertical elastic strain distribution, and d) vertical stress distribution.

3.4 Chapter summary

The subgrade stiffness highly influences the vertical strain on the top of the subgrade soil. However, its effect on the horizontal tensile strain at the bottom of the asphalt layer is insignificant. In consideration to stress dependent resilient modulus, a nonlinear elastic model is formulated. The results indicate a significant difference from the linear elastic method. Both methods, however, follow a hypothetical assumption that pavement layers possess elastic behaviour. In reality, it is the plastic deformation of each pavement layer that majorly controls the overall pavement performance. The next chapter addresses the theoretical and practical assumptions for modelling of the permanent deformation of subgrade soils.

Chapter 4

Modelling of permanent deformation of subgrade soils

This chapter presents a constitutive model to determine the permanent deformation of subgrade soils. Section 4.1 discusses the general perspective of permanent deformations of subgrade soils. In section 4.2, the main assumptions and premise of the proposed model are discussed, and the numerical implementation of the proposed model is presented. Then in section 4.3, the results obtained from the proposed model are compared with laboratory tests, and the practical implications of the model are indicated. In the end, section 4.4 summarises the main contents of this chapter.

4.1 Deformation of subgrade soils

Pavement design is carried out in consideration with the success of short-term and long-term performances. The long-term performance of flexible pavements is evaluated based on threshold values of road performance indicators and pavement distresses. Common modes of distresses in pavements associated to the long-term performance are accumulated permanent deformation, surface cracking and roughness. Permanent deformation of pavement layers is directly related to rutting, which is one of the most critical factors that affect the performance of flexible pavements. Other distress modes such as cracking and roughness are often associated to rutting.

In Pavement Management System (PMS) for road maintenance planning, the amount of rut depth is measured on the surface of the asphalt layer. Although the contribution of rutting from the subgrade to the total rut is usually small, the explicit quantification is important to outline different maintenance strategies. Different empirical methods for estimating the permanent deformation are presented in Chapter 2, section 2.4.2. However, the existing empirical models are viable only for few types of soils that they are derived from. Hence, numerical constitutive models are needed in mechanistic pavement design method.

The accumulated knowledge of permanent deformation in pavements follows the hierarchy of pavement layers from the top to the bottom. Particularly for subgrade soils, the emphasis has been very low due to the notion that the magnitude of stress is reduced at the subgrade level. Nevertheless, the variation of ground condition is immense, and the quality of subgrade soils can neither be fully investigated nor ensured during design and construction of roads, unlike the overlying pavement layers. Besides, the strength of subgrade soils is relatively low that even a small magnitude of stress can cause plastic deformation.

Uzan [110] suggested two approaches to incorporate rut prediction models in pavements. The first approach is computing the permanent strains under the traffic load at different locations and summing up the contribution of all layers. This approach is used when the stress state dominates the permanent deformation which is a typical phenomenon for road materials (for example aggregates) where the deformation is significant in the first loading cycles and stabilizes afterwards. In the second approach, the incremental deformation at each load application is computed and integrated over the design life. The later one incorporates the effect of the stress state as well as the number of load repetitions. This has been observed in laboratory tests of fine-grained soils (e.g. [15],[22],[65]).

In the following section, a constitutive model is proposed to predict the accumulation of permanent strains for subgrade soils. The deformation from the first loading cycle is incorporated in the elasto-plastic theoretical framework based on the Drucker-Prager yield criterion. The proximity of deviator stress level to the static failure limit is considered to predict the amount of incremental plastic strains at each loading cycle. The model is implemented in Abaqus FEA/UMAT and validated with test results available in the literature.

4.2 Formulation of the model

In the numerical modelling of permanent deformation in subgrade soils, the concept of plasticity must be applied. Conventional elasto-plastic models are well known and widely used in the analysis of geotechnical problems. Most models are efficient for static loading condition: either for static load application, incremental loading or constant strain rate loading. Nonetheless, the conventional elasto-plastic constitutive models based on strain hardening mechanism are able to simulate the plastic strains under monotonic loading. Due to this, the models do not account for the plastic strains after the first load application unless the load level is increased. New modelling concepts based isotropic and kinematic hardening mechanisms have been emerged to simulate cyclic loading applications in geo-materials (e.g [67],[98]). Such models are, however, appealing to few numbers of loading cycles and very large computation time is required to simulate the repeated load applications that of similar in pavements. Besides, extensive tests are required to determine the model parameters. Therefore, simplified and efficient models are yet to be developed for simulation of large number of load repetitions which can be applied in routine pavement design.

The fundamental principles of elasto-plastic models are available elsewhere in literature (e.g. [25],[31]). When soil models are considered to be employed for the prediction of permanent deformation, the hardening rule is considered to control the accumulation of plastic strains. Two distinct types of hardening mechanisms are available in elasto-plastic soil models, namely isotropic and kinematic hardening. Isotropic hardening is a reasonable assumption for monotonic loading. It has been observed in experiments that some materials exhibit translation of the yield surface upon stress reversal during cyclic loading. In this case, consideration of kinematic hardening provides a proper hardening mechanism. Traffic loading on pavements is not a complete cyclic loading, i.e. there is no deviator stress reversal; traffic loading is usually termed as “repeated” loading rather than “cyclic” loading. Due to this, only isotropic hardening is assumed in this study.

The premise for the hypothesis of the proposed model is based on the following studies.

- Bonaquist & Witczak [13] presented incremental permanent deformations normalized by the first-cycle strain for subgrade and base materials. The accumulation of permanent strain is strongly related to the magnitude of permanent strain on the first cycle of loading.

- The accumulation of permanent strains depends on the confining pressure [35],[97]. In order to include this effect in the long-term prediction in this study, the permanent deformation from the first loading cycle is obtained based on the Drucker-Prager yield criterion.
- The static stress limit is related to the accumulation of permanent strains [22],[65]. In the semi-analytical method described in Li & Selig [65], the static strength of the soil is used to include the effect of the physical state of the soil. The proximity to static failure is very important in the development of plastic deformation. The rate at which plastic strain accumulates was found to relate quite well to the proximity of the applied stress state to the stress conditions which are needed to cause failure under a single load [30],[72].

The proposed model in this study is presented in Equations [4.1] and [4.2].

$$\varepsilon_{p1,N} = N^{m\left(1-\frac{\sigma_d}{q_s}\right)}\,\varepsilon_{p1,0} \qquad [4.1]$$

$$\varepsilon_{p1,\,total} = \sum_{N=1}^{N}\left(N^{m\left(1-\frac{\sigma_d}{q_s}\right)}\right)\varepsilon_{p1,0} \qquad [4.2]$$

Where N is the number of load repetition, $\varepsilon_{p1,N}$ is the axial permanent strain for load cycle N, $\varepsilon_{p1,total}$ is the accumulated (total) axial permanent strain, $\varepsilon_{p1,0}$ is the accumulated axial permanent strain at the first loading cycle, σ_d is the deviator stress (loading from the traffic), q_s is the static strength of the soil, and m is a constant to fit laboratory tests.

The ratio of deviator stress to static strength of the soil (σ_d/q_s) represents the proximity of deviator stress level and it is directly related to stability of the soil relative to the apparent shakedown limit. It is noted in Equations [4.1] and [4.2] that the rate of accumulation of permanent strains increases as σ_d/q_s approaches to unity. When the level of deviator stress decreases, the accumulation of plastic strains reduces. The permanent strain from the first loading is obtained from an equivalent static load in the first load cycle based on the theory of plasticity.

4.2 Formulation of the model

The Drucker-Prager yield criterion is used to account for the effect of confining pressure. The Drucker-Prager yield criterion was first proposed by Drucker and Prager in the 1950ies is a smooth approximation to the Mohr-Coulomb law. The model is a modification of the von-Mises criterion where an extra term is included to introduce pressure sensitivity. The Drucker-Prager criterion states that plastic yielding begins when the second deviator stress and the mean stress reach a critical combination. The outset equation for plastic yielding is given in Equation [4.3] with graphical illustrations shown in Figures 4.1 and 4.2.

$$f(\sigma_{ij},c,\varphi) = \sqrt{J_2} + \eta p - \xi c \qquad [4.3]$$

$$J_2 = \frac{1}{2}\sigma_{ij}^{dev} : \sigma_{ij}^{dev} \;;\; \sigma_{ij}^{dev} = \sigma_{ij} - \frac{I_1}{3}\mathbf{I} \qquad [4.4]$$

Where f is the yield function, J_2 is the second deviator stress invariant, σ_{ij}^{dev} is the deviator stress tensor, p is the mean stress, η and ξ are defined in Equations [4.5] and [4.6], c is the cohesion, φ is the friction angle.

The isotropic hardening mechanism of soils is controlled by cohesion or friction angle depending of the type of soils [31],[80]. Cohesion hardening is considered for cohesive subgrade soils, while hardening governed by friction angle is used for non-cohesive soils such as sand and aggregates. Approximation techniques are obtained by making the yield surfaces of the Drucker-Prager and Mohr-Coulomb criteria coincident at the outer or inner edges of the Mohr-Coulomb surface.

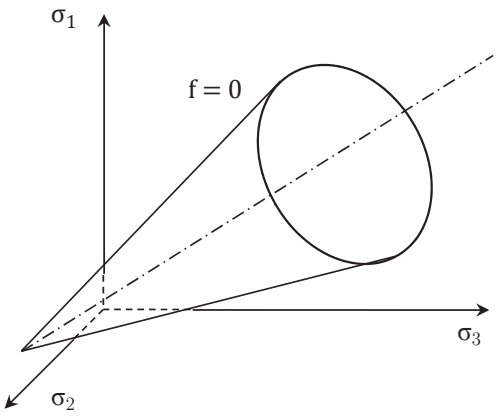

Figure 4.1: the Drucker-Prager yield surface in principal stress space. Adapted from Nordal [80].

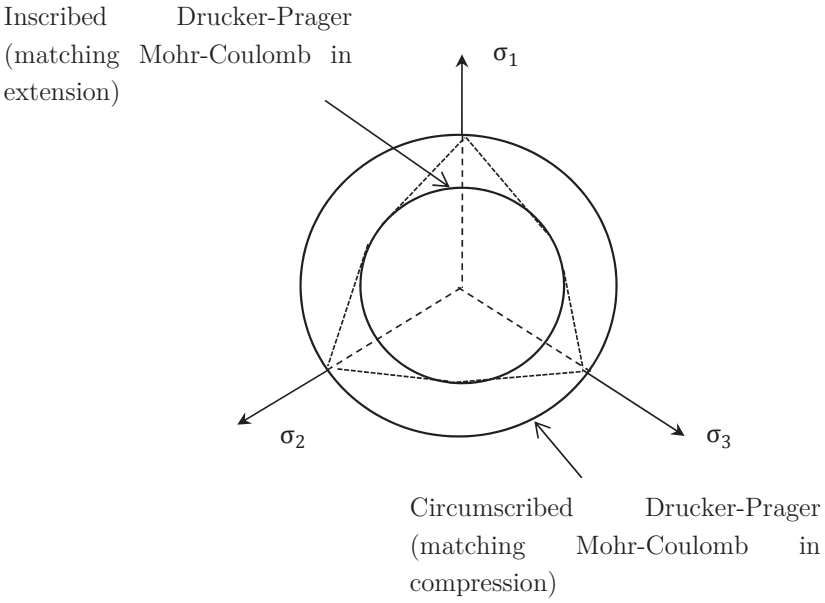

Figure 4.2: Alternative Drucker-Prager surfaces compared to Mohr-Coulomb. Adapted from Nordal [80].

For the case of compression, the approximation is provided in Equations [4.5] and [4.6].

$$\eta = \frac{6\sin\phi}{\sqrt{3}(3 - \sin\phi)} \quad [4.5]$$

$$\xi(\varphi) = \frac{6\cos\phi}{\sqrt{3}(3 - \sin\phi)} \quad [4.6]$$

In the theory of plasticity, the fundamental property of plastic strain increments is postulated in Equation [4.7].

$$d\varepsilon_{ij}^{p} = d\lambda \cdot \frac{\partial g(\sigma_{ij}, q_*)}{\partial \sigma_{ij}} \quad [4.7]$$

Where $d\varepsilon_{ij}^{p}$ is the incremental plastic strain, $d\lambda$ is a scalar quantity that quantifies the amount of plastic strain increment, g is the plastic potential which controls the direction of plastic flow, and q_* represents internal variables.

For the case of Drucker-Prager yield criterion, Equations [4.8] and [4.9] define the plastic potential.

$$g(\sigma_{ij}, \psi) = \sqrt{J_2} + \bar{\eta} I_1 \quad [4.8]$$

And,

$$\bar{\eta} = \frac{6*\sin\psi}{\sqrt{3}(3 - \sin\psi)} \quad [4.9]$$

Where ψ is the dilation angle.

When $\psi = \phi$, the plastic flow follows an associated flow rule which is a valid assumption for stable, work hardening materials. If $\psi \neq \phi$, the plastic flow follows non-associative flow rule.

4.2.1 Determination of parameters

The material parameters in the proposed model are obtained from triaxial testing. The maximum deviator static stress is the difference between the axial stress and the confining (radial) pressure at failure. The cohesion and friction angle are obtained from the effective mean stress (p') and deviator stress (q) as shown in Figure 4.3.

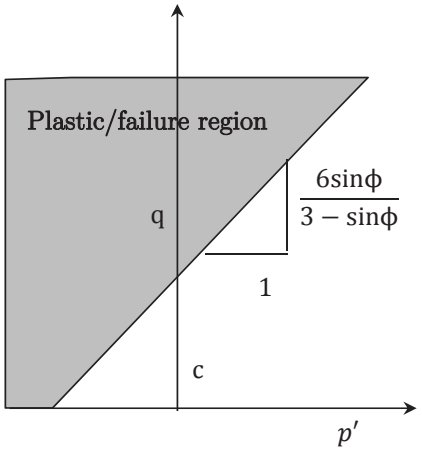

Figure 4.3: Determination cohesion and friction angle from conventional triaxial test.

4.2.2 Numerical implementation

The basic platforms of elasto-plastic constitutive models are decomposition of total strain in to elastic and plastic components, a relationship that governs the elastic contribution, and conditions for the development of plastic strains. The main ingredients necessary to control the plastic contribution in plasticity theory are yield criterion, flow rule, and hardening rule. Integration of constitutive equations is carried out within a finite set of integration points. Internal and external loads are balanced and a global iterative procedure supplies strain increments for each integration point. The constitutive model then, supplies constitutive stresses for the given strain increments and a process of finding an admissible stress state and its corresponding internal variables is carried out for

each integration points. The stress update mechanisms based on the above preconditions are available in the literature (e.g. [31],[102]).

The integration schemes for stress updates are generally categorized as explicit and implicit. In the explicit integration process, the stress increment is obtained with the knowledge of the total strain increment and the stress, and then an updated stress is obtained. Though this method is simple and straight forward, it is conditionally stable, i.e. the solution may diverge. The accuracy of integration also depends on the increment size. In the implicit integration scheme, in contrary, a trial stress increment is chosen which takes the updated stress outside the yield surface. The stress is then updated with a plastic correction to bring it back onto the yield surface. The implicit elastic predictor-return mapping algorithm for the Drucker-Prager model described in de-Souza-Neto *et al.* [31] is used for the numerical implementation in this study. The implicit scheme, in this case, insures a converged solution of the plastic strains in a few load increments.

If the applied load exceeds the yield limit of the soil, plastic strains develop and are obtained based on Equation [4.7]. Since plastic strains do not increase after the first load increment (unless the load level is increased), the semi-analytical model proposed in Equations [4.1] and [4.2] are used to predict the plastic strains after the first cycle loading. The illustration of the proposed model is shown in Figure 4.4.

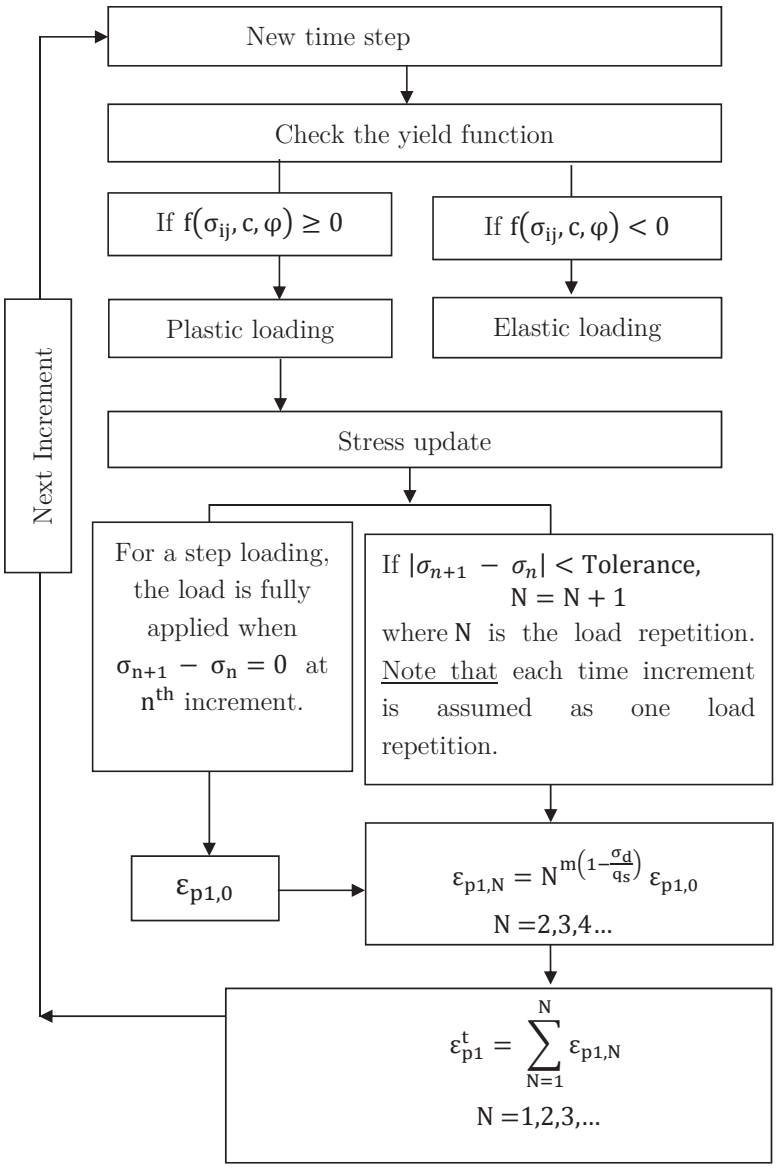

Figure 4.4: Schematic presentation of the proposed constitutive model.

4.2.3 Deformation from the first load application

The plastic deformation from the first load application is obtained based on the theory of elastoplasticity. The derivation of stress updates and consistent tangent modulus based on de-Souza-Neto *et al.* [31] is presented in this section.

The first trial stress ($\sigma_{ij}{}^{Trial}_{n+1}$) is obtained from a given elastic stiffness matrix (D^e_{ijkl}) and assumed elastic strain ($\varepsilon^{e\,Trial}_{ij\,n+1} = \varepsilon^e_{ij\,n} + \Delta\varepsilon_{ij}$) as shown in Equation [4.10].

$$\sigma_{ij}{}^{Trial}_{n+1} = \sigma_{ij\,n} + D^e_{ijkl}\varepsilon^{e\,Trial}_{kl\,n+1} \qquad [4.10]$$

Using the updated trial stress, and internal material variables (q_*), the yield function is checked for the new state. If $f\left(\sigma_{ij}{}^{Trial}_{n+1}, q_{*n}\right) < 0$, the response will be fully elastic, and there will be neither plastic flow nor evolution of internal variables. If $f\left(\sigma_{ij}{}^{Trial}_{n+1}, q_{*n}\right) = 0$, the plastic strain is obtained (using the flow rule) from Equations [4.11] and [4.12]. During plastic loading, the stress is restricted to stay at the yield surface $f\left(\sigma_{ij}{}^{Trial}_{n+1}, q_{*n}\right) > 0$ is inadmissible to fulfil the consistency condition in plasticity theory.

$$d\varepsilon^p_{ij} = d\lambda \cdot \left.\frac{\partial g}{\partial \sigma_{ij}}\right|_{n+1} \qquad [4.11]$$

$$\frac{\partial g}{\partial \sigma_{ij}} = \frac{1}{2}\frac{\partial g}{\partial \sigma_{ij}}\sigma^{dev}_{ij} + \frac{\bar{\eta}}{3}I \qquad [4.12]$$

Then, the general return-mapping update formula (Equation [4.13]) is used to obtain the new stress state. Figure 4.5 shows the illustration of the stress update mechanism for an implicit scheme.

$$\sigma^{n+1}_{ij} = \sigma^{Trial}_{ij} - d\lambda D^e_{ijkl}\left.\frac{\partial g}{\partial \sigma_{ij}}\right|_{n+1} \qquad [4.13]$$

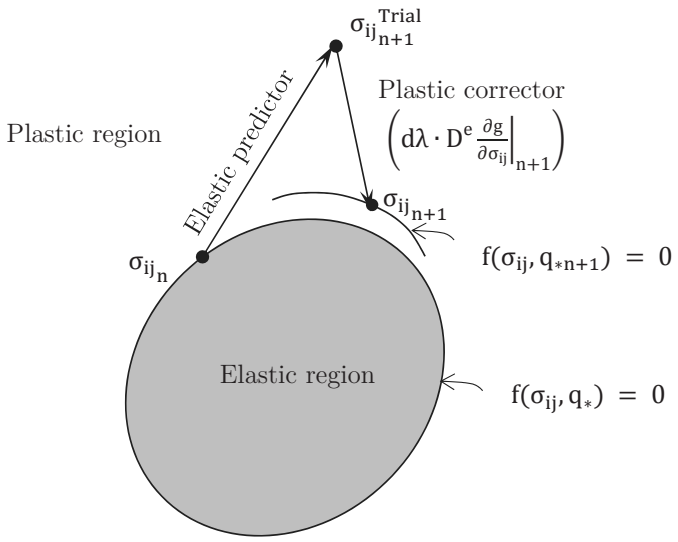

Figure 4.5: Geometric interpretation of return mapping scheme for hardening plasticity. Adapted from de-Souza-Neto *et al.* [31] (*Chapter 7, p. 197*)

Substituting Equation [4.12] into Equation **[4.13]**, and dividing the flow vector is into deviatoric and volumetric components, the expressions in Equation [4.14] are obtained.

$$\begin{aligned}\sigma_{ij,n+1} &= \sigma_{ij}^{Trial} - d\lambda\left[\frac{1}{2\sqrt{J_2}}\left(\left[\frac{\partial g}{\partial \sigma_{ij}}\right]_{dev}\right)_{n+1} + K\left(\left[\frac{\partial g}{\partial \sigma_{ij}}\right]_{vol}\right)_{n+1}\right] \\ &= \sigma_{ij}^{Trial} - d\lambda\left[\frac{G}{\sqrt{J_2}}\sigma_{ij,n+1}^{dev} + \frac{K\bar{\eta}}{3}I\right]\end{aligned} \qquad [4.14]$$

Where G is the shear modulus, and K is the bulk modulus.

Due to the definition of J_2, the ratio the deviator stress to the second stress invariant remains unchanged, i.e. $\sigma_{ij,n+1}^{dev}/J_2(\sigma_{ij,n+1}^{dev}) = \sigma_{ij}^{dev\,Trial}/J_2(\sigma_{ij}^{dev\,Trial})$. Then, the Equation [4.14] is rewritten as:

$$\sigma_{ij,n+1} = \sigma_{ij}^{Trial} - d\lambda\left[\frac{G}{\sqrt{J_2(\sigma_{ij}^{dev\,Trial})}}\sigma_{ij}^{dev\,Trial} + \frac{K\bar{\eta}}{3}I\right] \quad [4.15]$$

The deviator (σ_{ij}^{dev}) and hydrostatic (p) stress components are:

$$\sigma_{ij,n+1}^{dev} = \left(1 - \frac{Gd\lambda}{\sqrt{J_2(\sigma_{ij,n+1}^{dev\,Trial})}}\right)\sigma_{ij\,n+1}^{dev\,Trial} \quad [4.16]$$

$$p_{n+1} = p_{n+1}^{Trial} + K\bar{\eta}d\lambda$$

The accumulated plastic strain is obtained from Equation [4.17].

$$\bar{\varepsilon}^{p}{}_{n+1} = \bar{\varepsilon}^{p}{}_{n} + d\bar{\varepsilon}^{p}\,; \quad d\bar{\varepsilon}^{p} = d\lambda \cdot \xi \quad [4.17]$$

The solution from the consistency condition for $d\lambda$ in Equation [4.18] is used to update the stresses in Equation [4.15] or Equation [4.16].

$$\tilde{f}(d\lambda) \equiv \sqrt{J_2\left(\sigma_{ij\,n+1}^{dev\,Trial}\right)} - Gd\lambda + \eta(p_{n+1}^{Trial} + K\bar{\eta}d\lambda) - \xi \cdot c(\bar{\varepsilon}^{p}{}_{n} + d\lambda \cdot \xi) = 0 \quad [4.18]$$

Consistent tangent modulus

For a particular case of a stress state in the subgrade layer in pavements, the return mapping to the smooth part of the cone is considered. The elasto-plastic tangent modulus is given as shown in Equation [4.19].

$$D_{ijkl}^{ep} \equiv \frac{d\sigma_{ij,n+1}}{d\varepsilon_{kl\,n+1}^{e\,Trial}} \quad [4.19]$$

Equation [4.20] shows the consistent tangent modulus. The mathematical derivations can be referred in de-Souza-Neto *et al.* [31] (*Chapter 8: p. 338-339*).

$$D_{ijkl}^{ep} = 2G\left(1-\frac{d\lambda}{\sqrt{2}\left|\varepsilon_{ij}^{e\,Trial}_{n+1}\right|}\right)I_d + 2G\left(\frac{d\lambda}{\sqrt{2}\left|\varepsilon_{ij}^{e\,Trial}_{n+1}\right|} - GA\right)N_{ij}\otimes N_{ij} - \sqrt{2}\,GAK\left(\eta N_{ij}\otimes \mathbf{I} + \bar{\alpha}\mathbf{I}\otimes N_{ij}\right) + K(1-K\eta\bar{\eta}A)\mathbf{I}\otimes\mathbf{I} \quad [4.20]$$

Where I_d is the deviatoric projection tensor, N_{ij} is the second order tensor as shown in Equation [4.21], and A is defined in Equation [4.22].

$$N_{ij} = \frac{\varepsilon_{ij}^{e\,Trial}_{n+1}}{\left|\varepsilon_{ij}^{e\,Trial}_{n+1}\right|} \quad [4.21]$$

$$A = \frac{1}{G + K\eta\bar{\eta} + \xi^2 H} \quad [4.22]$$

Where H is the hardening modulus

Verification

The constitutive numerical model based on the Drucker-Prager yield criterion for the first cycle loading is implemented in Abaqus FEA/UMAT. The numerical scheme was written in FORTRAN programming language. For the verification of the numerical model, the prediction of plastic strains from the first load application using the UMAT model presented in this study is compared to In-build Mohr-Coulomb model in Abaqus FEA. Similar results are obtained.

4.2.4 Repeated loading

In the implicit numerical scheme, the solution for the applied load is converged in a few time increments. In Abaqus FEA, there are two load increment methods, namely RAMP and STEP. RAMP is used for a gradual increment of the load proportional to the time step while STEP represents for the conditions where the total load is applied at once. In this study, a STEP option is used to obtain the plastic strain from the first load application. Though, the concept of a sudden application of the entire load is used, the solution does not converge in the first

time increment. The load is assumed to be fully applied when $|\sigma_{n+1} - \sigma_n| <$ Tolerance; where the "Tolerance" is a very small number chosen by the user. Figure 4.6 illustrates the load application in the first load application and the assumption of the subsequent load repetitions that are considered in this study.

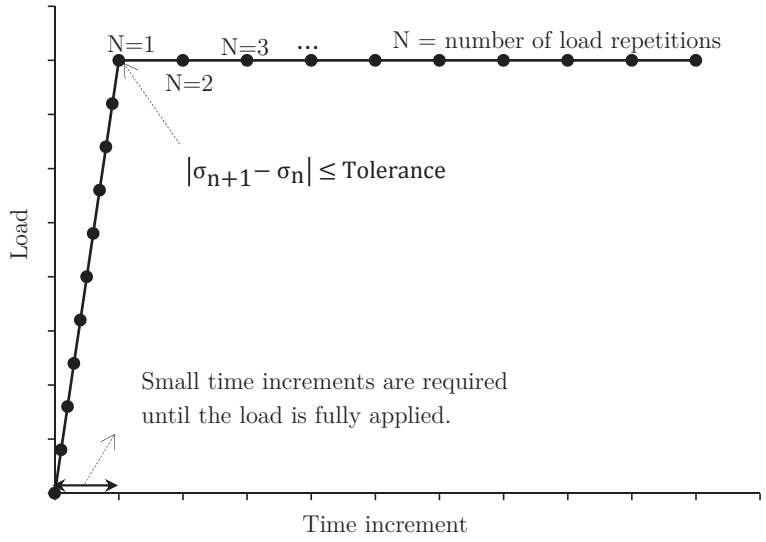

Figure 4.6: Concept of repeated load applications assumed in this study.

4.3 Results and discussions

Numerical simulations are carried out based on the proposed model to compare the results with laboratory tests obtained from Townsend and Chrisolm (as cited in Li & Selig [65]). The physical properties of the soil were: dry density, ρ_d = 1440 kg/m^3, and water content, w = 28.7%. The maximum static strength obtained from uniaxial laboratory testing was q_s = 159kPa. The input parameters shown in Table 4.1 are calibrated for the same maximum static strength i.e. 159kPa, using finite element analysis (strain controlled uniaxial test simulation). Three sets of deviator stress are considered for numerical analysis similar to the laboratory tests reported in Li & Selig [65]: σ_d = 52.5kPa, 73.1kPa,

and 81.1kPa. Figure 3 shows the comparison of the numerical simulation with laboratory tests at different deviator stress levels.

Table 4.1: Input parameters.

Parameter		Unit	Value
Stiffness (E)		MPa	100.0
Poisson's ratio (ν)		[-]	0.3
Friction angle (ϕ)		[°]	15.0
Dilation angle (ψ)		[°]	15.0
Hardening parameters	Cohesion: c_0	kPa	10.0
	Plastic strain: $\bar{\varepsilon}_{p,0}$	[-]	0.0
	Cohesion: c_1	kPa	61.0
	Plastic strain: $\bar{\varepsilon}_{p,1}$	[-]	0.001275
Rate of plastic strain accumulation: m		[-]	-1.49

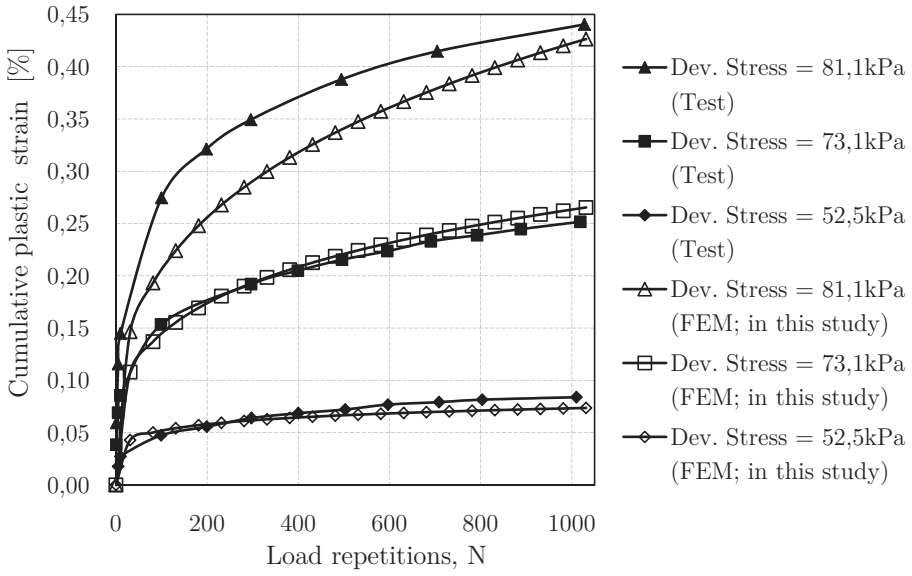

Figure 4.7: Comparison of the proposed model in this study with test results reported in Li & Selig [65] for soil type $\rho_d = 1440$ kg/m^3, $w = 28.7\%$, $q_s = 159$kPa.

The proposed model is also validated for the same soil type but with different water content where the test data is obtained from Townsend and Chisolm (as cited in Li & Selig [65]). Ying *et al.* [122] showed that the cohesion of a soil does not change appreciably at high water content; whereas the friction angle changes substantially (see Figure 4.8). Hence, in the calibration of material parameters in this study, the cohesion hardening parameters are kept constant, and only the friction angle is varied to obtain a static strength of $q_s = 193$kPa for the soil with dry density $\rho_d = 1470$ kg/m^3, and water content, $w = 27.6\%$. Consequently, $\varphi = 26°$ is obtained. The calibrated input parameters for the numerical model are summarised in Table 4.2. The results from finite element analysis in comparison with laboratory tests are presented in Figure 4.9.

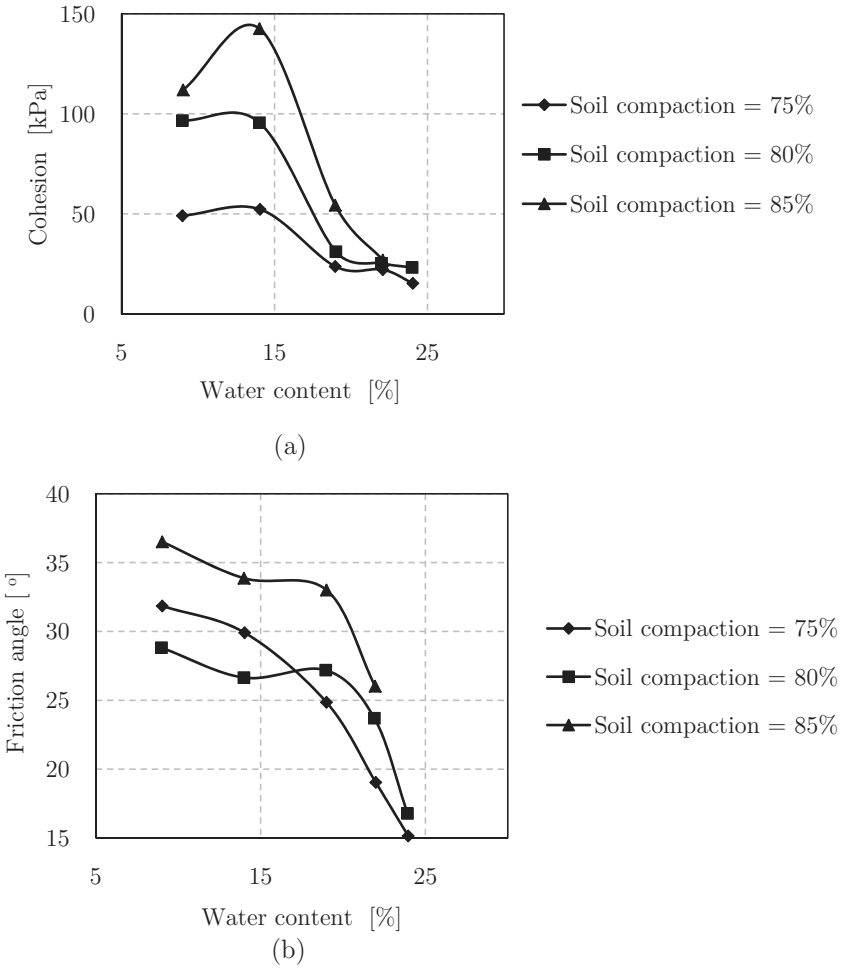

Figure 4.8: Change of soil parameters with water content. a) cohesion, and b) friction angle. Adapted from Ying *et al.* [122].

Table 4.2: Input parameters.

Parameter		Unit	Value
Stiffness (E)		MPa	120.0
Poisson's ratio (ν)		[-]	0.3
Friction angle (ϕ)		[°]	26.0
Dilation angle (ψ)		[°]	26.0
Hardening parameters	Cohesion: c_0	kPa	10.0
	Plastic strain: $\bar{\varepsilon}_{p,0}$	[-]	0.0
	Cohesion: c_1	kPa	61.0
	Plastic strain: $\bar{\varepsilon}_{p,1}$	[-]	0.001275
Rate of plastic strain accumulation: m		[-]	-1.49

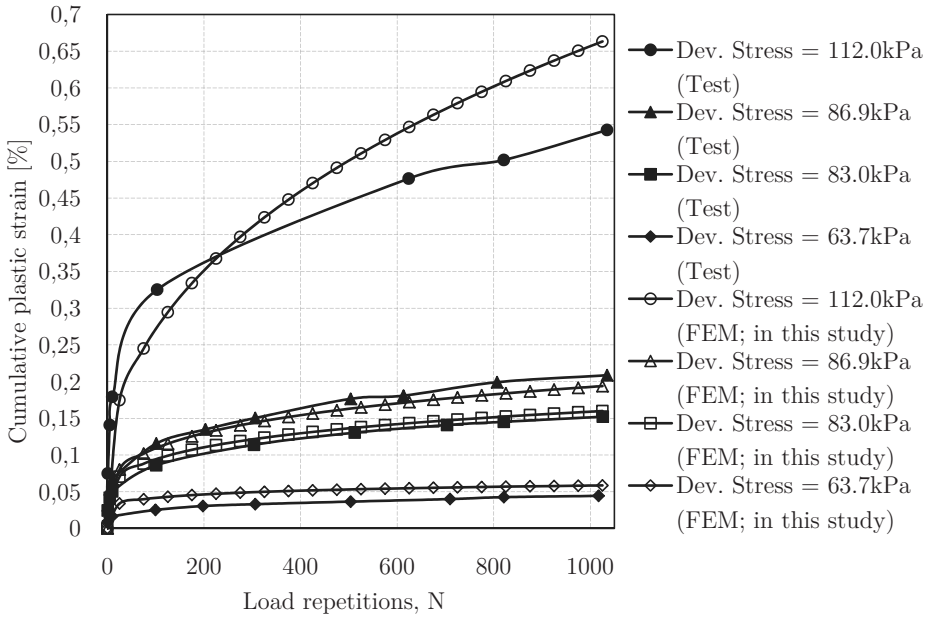

Figure 4.9: Comparison of the proposed model in this study with test results reported in Li & Selig [65] for soil type $\rho_d = 1470$ kg/m^3, $w = 27.6\%$, $q_s = 193$kPa.

Figures 4.7 and 4.9 show that the proposed numerical model gives a good agreement with test results up to 50% of the static strength of the soil. For higher deviator stresses, the results do not fit well. When the deviator stress level is close

to the static strength of the soil, the failure phenomenon is very much complicated, and the physical interpretation of such scenario is not easily captured using simplified models. The degree of mobilization of subgrade soils in pavement is usually low, i.e. less than 50% of the static strength of the soil. Hence the proposed model is this study can effectively be used for subgrade soils.

The Drucker-Prager failure criterion used to obtain the plastic strains in the first loading cycle provides the capability of the proposed model to predict the effect of confining pressure on the accumulated permanent deformation. For the given input parameters in Table 4.1, the deviator stress is kept constant at σ_d = 73.1kPa, and the confining pressure is varied. In addition, a loading cycle up to 10000 repetitions is simulated.

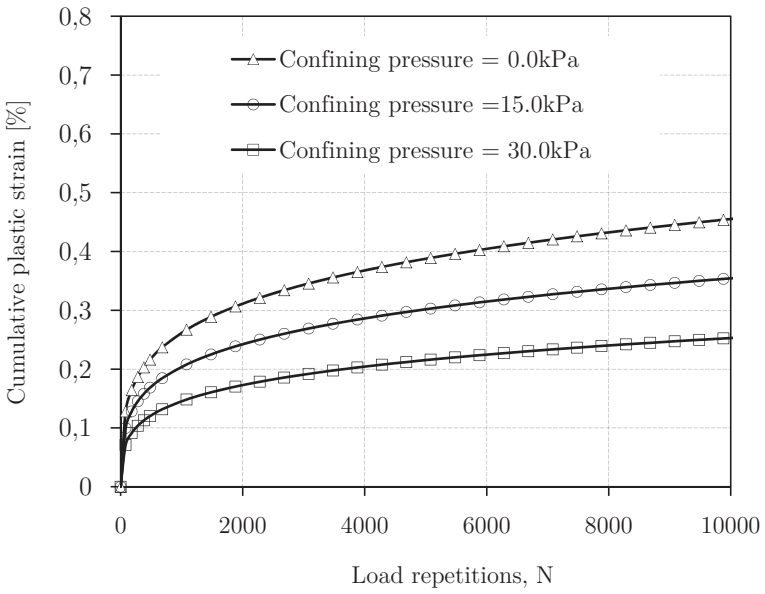

Figure 4.10: Effect of confining pressure on the accumulation of plastic strain at a deviator stress of 73.1kPa.

The effect of confining pressure on the accumulation of plastic strains is clearly shown in Figure 4.10. As the confining pressure increases, the permanent

deformation is reduced. When the confining pressure is doubled (from 15kPa to 30kPa), the accumulation of plastic strains is reduced by 29%. This implies that confining pressure is also an important component in the prediction and quantification of plastic strains.

Some of the practical implications and the advantages of the proposed model in this study over the existing analytical models are:

- The effect of the friction angle and cohesion of the soil is included.
- The effect of confining pressure is incorporated.
- The model parameters are obtained from conventional triaxial tests which are commonly carried out in routine geotechnical investigation.

The application of the proposed model is apparently limited to cohesive soils. For non-cohesive soils such as sands and aggregates, the accumulation of plastic strains has not been clearly observed to relate to the static failure limit.

4.4 Chapter summary

Rutting of flexible pavements is a major concern on the evaluation of pavement performance. The rutting in the unbound layers, particularly in the subgrade soils, is mainly as a result of permanent deformation due to traffic loads. Hence, the permanent deformation characteristics of subgrade soils are essential components to quantify the amount of rut contributed from the subgrade. The main objective of this study was to show that incremental permanent strains in repeated loadings can be related to the value of the first loading cycle. A good agreement is obtained between the predicted results and laboratory tests for deviator stress level up to 50% of the static strength of the soil. In pavements, especially in subgrade and subbase layers, the stress level is relatively low. Hence, the proposed model in this study can be used effectively in mechanistic pavement design.

Chapter 5

Optimisation of effective depth of compaction of subgrade soils

This chapter deals with a method to use the strength parameters of soils to achieve an optimum compaction depth. The first section presents the general aspects of lift thickness in compaction of subgrade soils. Section 5.2 introduces a three-dimensional finite element model (FEM) for simulation of soil compaction. Section 5.3 discusses the results obtained from the finite element analyses. In the same section, possible optimization techniques of soil compaction are presented based on parametric study of soil strength parameters. The last section, section 5.4 summarises the main themes of this chapter.

5.1 Compaction of fine-grained soils

Soil compaction is an important phase during construction of roads. Its primary aim is to reduce the void ratio, in order to improve the strength of the soil. In this way, a good bearing capacity of pavement foundation is obtained and the long-term deformation is reduced. The principles of compaction of fine-grained soils and the properties that control soil compactibility have been discussed in Chapter 2 (section 2.3.1). This chapter discusses one of the important factors that affect field compaction, i.e. lift thickness.

Lift thickness refers to the depth of the soil layer, over the previously compacted layer. It affects both machine performance and compaction cost. Figure 5.1 shows an approximate method for determining the lift height based on the required minimum compacted relative density. As shown in the same figure, the maximum

density is located at some depth below the surface where the compaction is applied.

If a thin lift height is provided below the required limit, much of the compaction energy is applied on the previously compacted layer. Similarly, too thick lift height causes some problems during compaction, for example the compaction energy is reduced and the soil mass, particularly the lower portion of the lift may not be compacted as intended — the compaction process will be difficult due to unwanted ruts. The machine may also stuck in the soil, and in some cases, the drum may push the soil in the front rather than compacting it.

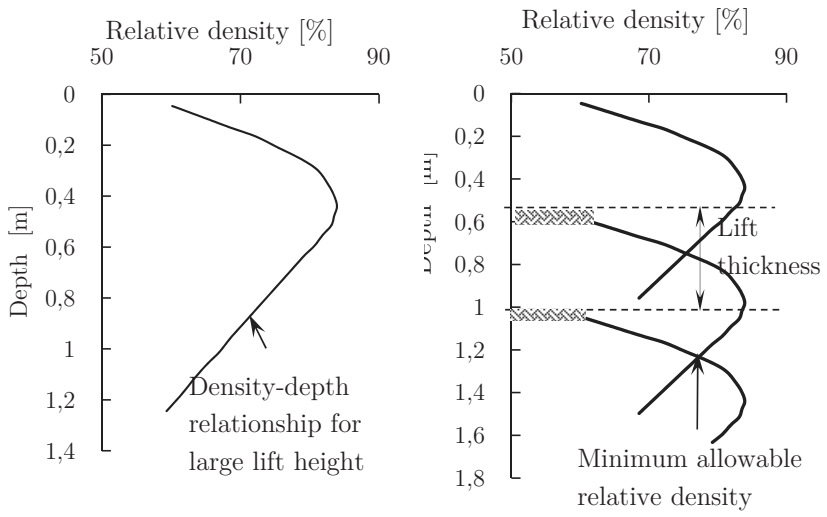

Figure 5.1: Principle of an approximate method for determining a lift thickness to achieve a minimum compacted relative density. Adapted from Dappolonia et al., as cited in Holtz & Kovacs [46] (*Chapter 5, p. 139*).

Road agencies usually specify the limits for the thickness of the lift height. The choice of lift thickness depends on the soil type, the compaction method and type, and the compaction effort. The latter two factors have been the main

considerations in practice. For instance, similar lift heights are considered for a range of fine-grained soils, and only the compaction method is varied. In this study, finite element analysis is carried out to evaluate the effect of soil parameters such as friction angle and cohesion on effective depth of compaction. It should be noted that the friction angle and cohesion of soil are not inherent properties of soil — rather they describe the behaviour the soil at a particular state. Hence, the type of soil and water content describe the condition of the soil and can be expressed in terms of cohesion and friction angle.

5.2 Finite element modelling

With the development of high computer speed and availability of advanced finite element modelling tools, soil-structure modelling is gaining popularity in the recent years for optimization of soil-structure interaction problems (e.g. [26],[39],[115]). Besides the modelling techniques, appropriate soil models should be chosen for the specific practical problems. The conventional elastoplastic soil models, such as the standard Drucker-Prager and Mohr-Coulomb models do not provide the volumetric compaction of the soil. In order to alleviate this limitation, the Drucker-Prager model is extended to Drucker-Prager Cap model which is discussed in the following section. This constitutive model has been used for optimization technique of the compaction process in soils.

5.2.1 The soil model/Drucker-Prager Cap model

The basic principles of Drucker-Prager yield criterion are discussed in Chapter 4 (Section 4.2). The Drucker-Prager Cap model is a modification of the standard Drucker-Prager model with additional cap as shown in Figure 5.3. The deviator stress measure of the standard Drucker-Prager yield surface is modified in Abaqus FEA [104] to allow matching of different stress values in tension and compression in the deviatoric plane. This provides flexibility in fitting experimental results with a smooth approximation to the Mohr-Coulomb surface. Equation [5.1] presents the equation for the shear failure surface of the model shown in Figure 5.3.

$$F_s = t - p^{*}\tan\beta - d = 0 \qquad [5.1]$$

Where F_s is the shear failure surface, β and d represent the friction angle and cohesion of the soil (in Abaqus) respectively. The deviator stress measure (t) is defined in Equation [5.5] with graphical illustration as shown in Figure 5.2, and p is the mean stress defined in Equation [5.2].

$$p = -\frac{1}{3}\text{trace}(\sigma_{ij}) \quad [5.2]$$

Abaqus FEA [104] uses Equations [5.3] and [5.4] to determine the friction angle and cohesion inputs into the program.

$$\tan\beta = \frac{6 * \sin\phi}{3 - \sin\phi} \quad [5.3]$$

$$d = \frac{6*c*\sin\phi}{3-\sin\phi} \quad [5.4]$$

Where ϕ and c represent the friction angle and cohesion in Mohr-Coulomb failure surface respectively.

$$t = \frac{1}{2}q\left[1+\frac{1}{M}-\left(1-\frac{1}{M}\right)\left(\frac{r}{q}\right)^3\right] \quad [5.5]$$

Where t is the deviator stress measure, q is the deviator stress and r represents the dependence of the yield surface on the third stress invariant (see Equation [5.6]). M is the ratio of the yield stress in triaxial tension to the yield stress in triaxial compression, and it controls the shape of the yield surface.

$$q = \left(\frac{3}{2}\sigma_{ij}{}^{dev}:\sigma_{ij}{}^{dev}\right)^{\frac{1}{2}} \quad ; \quad r = \left(\frac{9}{2}\sigma_{ij}{}^{dev}:\sigma_{ij}{}^{dev}\cdot\sigma_{ij}{}^{dev}\right)^{\frac{1}{3}} \quad [5.6]$$

Where σ_{ij} and $\sigma_{ij}{}^{dev}$ are the stress tensor and its deviatoric component respectively.

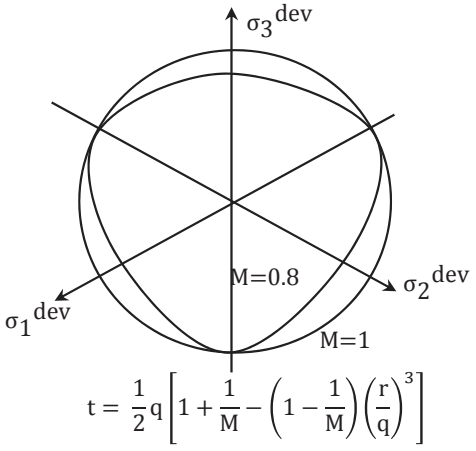

Figure 5.2: Typical yield surfaces of the Cap model in the deviatoric stress plane. Adapted from Abaqus FEA [104].

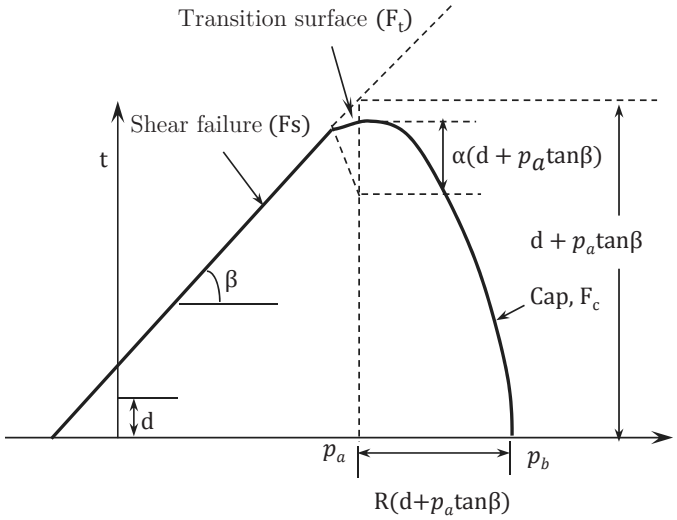

Figure 5.3: Density dependent Drucker-Prager Cap model. Adapted from Abaqus FEA[104].

The cap yield surface illustrated in Figure 5.3 hardens or softens as a function of the volumetric plastic strain. The expressions of the cap yield surface (F_c), and the transition surface (F_t), are shown in Equations [5.7] and [5.8].

$$F_c = \sqrt{(p - p_a)^2 + \left[\frac{R*t}{1+\alpha - \frac{\alpha}{\cos\beta}}\right]^2} - R(d + p_a \tan\beta) = 0 \quad [5.7]$$

$$F_t = \sqrt{(p - p_a)^2 + \left[\frac{\alpha t}{1+\alpha - \frac{\alpha}{\cos\beta}}\right]^2} - \alpha(d + p_a \tan\beta) = 0 \quad [5.8]$$

Where R is a material parameter that controls the shape of the cap, p_a is an evolution parameter that represents the volumetric plastic strain (hardening or softening).

The value of $d, \beta, R, \varepsilon^p_{vol,0}, \alpha,$ and M are used to define the shape of the yield surface. In the cap region, associated flow rule is assumed and the plastic flow is defined by a flow potential in Equation [5.9]. For the Drucker-Prager failure surface and the transition yield surface, a non-associated flow is assumed, i.e. the shape of the flow potential is different from the yield surface. The elliptical flow potential surface is given in Equation [5.10]. The geometrical interpretation of the flow potential is presented in Figure 5.4.

$$G_c = \sqrt{(p - p_a)^2 + \left[\frac{R*t}{1+\alpha - \frac{\alpha}{\cos\beta}}\right]^2} = 0 \quad [5.9]$$

$$G_s = \sqrt{[(p_a - p)\tan\beta]^2 + \left[\frac{t}{1+\alpha - \frac{\alpha}{\cos\beta}}\right]^2} = 0 \quad [5.10]$$

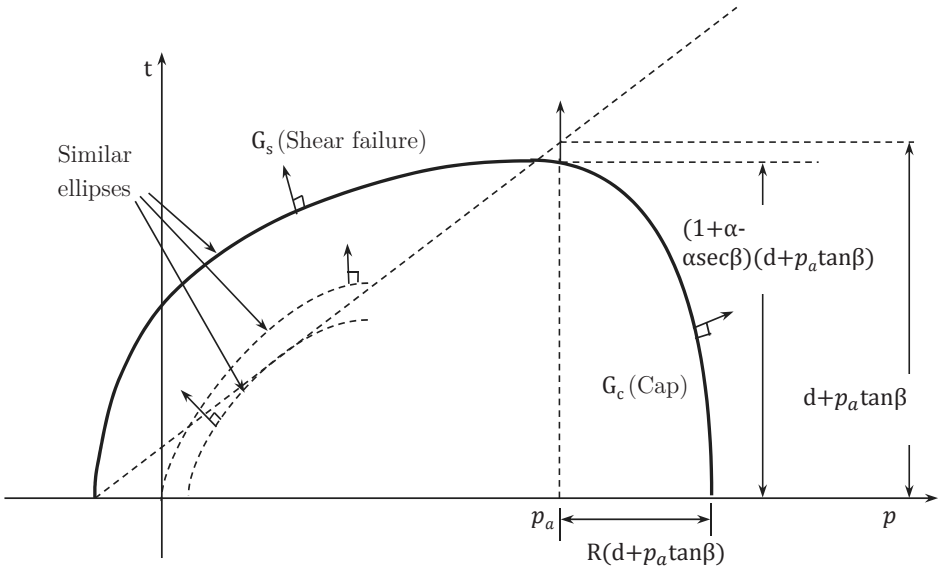

Figure 5.4: Modified Drucker-Prager/Cap model: flow potential in the $p-t$ place. Adapted from Abaqus FEA [104].

The evolution parameter (p_a) is obtained from Equation [5.11].

$$p_a = \frac{p_b - R^*d}{1+R\tan\beta} \qquad [5.11]$$

The cap hardening curve can alternatively be obtained from results of the isotropic consolidation tests in soils (see Figure 5.5) as shown in Equation [5.12] [41].

$$\varepsilon_v^p = \frac{\lambda-\kappa}{1+e_0}\ln\frac{p'}{p'_0} = \frac{C_c-C_s}{2.3(1+e_0)}\ln\frac{p'}{p'_0} \qquad [5.12]$$

Where λ (or C_c) is the compression index, κ (or C_s) is the swelling index, e_0 is the initial void ratio at initial stress condition of p'_0, and p' is the mean effective stress corresponding to the plastic volumetric strain (ε_v^p).

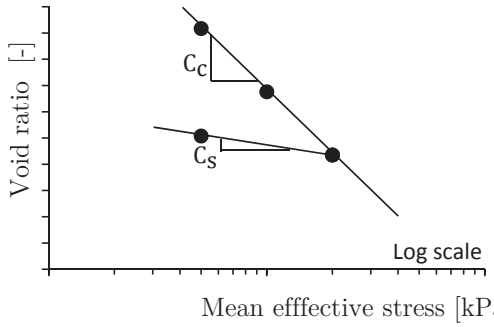

Figure 5.5: Isotropic consolidation test to determine hardening parameters.

Knowing the volumetric plastic strain, the current density (ρ) in reference to initial density (ρ_0) is obtained using Equation [5.13].

$$\varepsilon_{vol}^{p} = \ln\left(\frac{\rho}{\rho_0}\right) \qquad [5.13]$$

The analysis presented in this study is based on the assumption of monotonic loading conditions of static rollers during soil compaction. If the dynamic effect of the roller (i.e. rolling speed, vibration frequency) is to be evaluated, advanced rate-dependent models such as the hypoplastic model formulation must be considered for realistic simulation of the compaction process [50],[56]. Another important aspect of numerical simulation of soil compaction is the geometric and boundary modelling techniques. Such issues are addressed mainly based on Abaqus FEA [104].

5.2.2 Geometric modelling

Numerical simulation of soil-structure interaction needs the contact boundary conditions to be properly defined. The numerical simulations presented in this study are carried out using Abaqus/Explicit. The explicit scheme is computationally efficient for discontinuous events and processes. The use of small time increments in this method simplifies the treatment of contact problems

because it allows the solution to proceed without iterations and without requiring stiffness matrices to be formed. The three-dimensional model shown in Figure 5.6 consists of two distinct bodies: a soil bed and a rigid rotating roller.

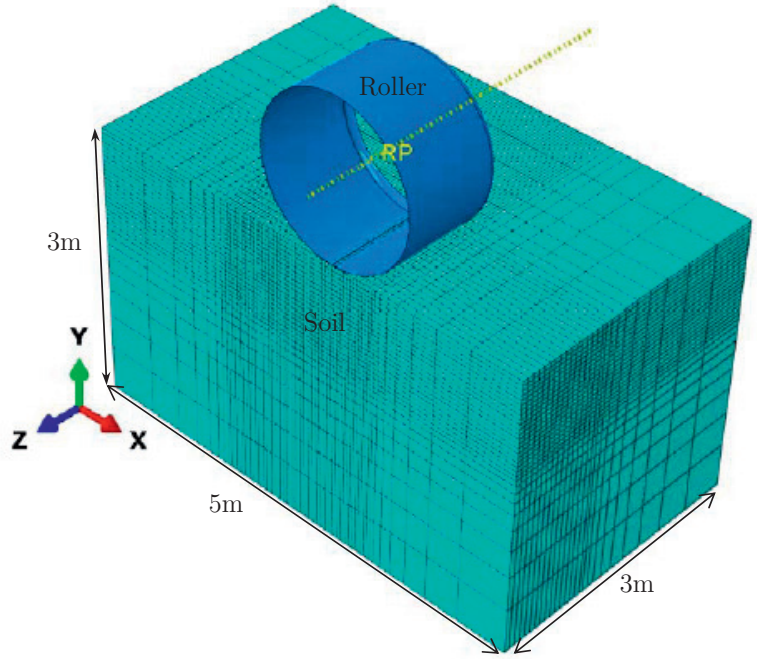

Figure 5.6: Geometric model of the soil and roller.

Roller

The roller has a diameter of 1.2m. For low rolling speed, the rotary inertia of the roller is not considered in the model. The roller is modelled as an analytical rigid body and it is non-deformable in the analysis. Analytical rigid surface is chosen for both accuracy and computational performance since analytical surfaces are not discretized in to finite elements [104]. A cylindrical shell with edge fillet of radius 0.07m is used in the outer edge of the roller to avoid numerical problems.

Because of symmetry, only one-half of the roller (width = 1m) is modelled. To ensure the dynamic analysis with a very small inertial effect, a small mass (i.e. 100kg) is assigned for the roller. A point load, equivalent to the weight of the roller) is applied at the centre of mass (at the reference point in this case). In the

numerical model, the motion of the rigid body is controlled by the boundary and loading conditions applied at the reference point.

Soil layer

The soil layer in Figure 5.6 is compressible and the material properties are defined using the Drucker-Prager Cap model. The element type available in Abaqus C3D8R (8-node linear brick, reduced integration, solid elements) is used for numerical simulation. This element supports the three translation degrees of freedom in the x-, y- and z- directions. Dense mesh (or small elements) defines the geometry in the periphery of the anticipated contact area with the roller. Particularly in the longitudinal direction (direction of rolling), very small elements are used to ensure a smooth interaction between the roller surface and the soil.

Roller-Soil Interaction

The analytical surface of the roller is constrained to the reference point. A roller speed of 4km/h is assumed and a corresponding angular velocity of 1.85 rad/sec is applied at the reference point. Since the soil model used in this study is rate-independent, the rolling speed has not influence on the compaction process. A surface-to-surface contact is chosen and a penalty contact method is used in Abaqus/Explicit. Two surfaces (the outer surface of the roller and the top surface of the soil layer) are defined for the roller-soil interaction. The friction coefficient between the roller and the soil surface is roughly approximated from the friction angle of the soil, i.e. $\text{friction coef.} = \tan\phi$; where ϕ is the friction angle of the soil. To be more realistic, a slightly lower value of friction coefficient than the one computed from the friction angle is used. This is to account the fact that rolling friction is lower than sliding or static friction. For $\phi < 20°$, a friction coefficient of 0.3 is considered to ensure rolling of the roller on the soil surface.

5.3 Results and discussions

The elastic behaviour of the soil is defined by its Young's modulus and the Poisson's ratio, and is combined with the Modified Drucker-Prager Cap model to model the overall soil behaviour during compaction. For triaxial loading

condition, the material cohesion (d) and friction angle (β) are obtained from the Mohr-Coulomb parameters, cohesion (c) and friction angle (ϕ) as shown in Equations [5.3] and [5.4] for the points where the Drucker-Prager yield surface coincides with the Mohr-Coulomb in triaxial compression. Table 5.1 presents the input data for analyses. The Cap hardening parameters are determined, based on the ratio of compression index to swelling index ($\lambda/\kappa=10$), where $\lambda=0.2$ is assumed.

Table 5.1: Assumed input parameters for the Cap model.

Parameters	Unit	Value
Cap eccentricity parameter (R)	[-]	0.2
Initial yield stress (p'_0)	kPa	60
Initial Cap yield surface position ($\varepsilon^p_{vol,0}$)	[-]	0
Transition surface radius parameter (α)	[-]	0.01
Flow stress ratio (K)	[-]	1.0
Density(initial), (ρ_0)	kg/m^3	1600
Stiffness (E)	MPa	50
Poisson's ratio (ν)	[-]	0.3
Mohr-Coulomb cohesion (c)	kPa	40
Mohr-Coulomb friction angle (ϕ)	[°]	20

Figure 5.7 shows the result from a single roller pass. The density at the instance of roller loading is computed from the total volume change, i.e. both the elastic and plastic volume change in the soil. After the roller is passed, the density is computed only from the plastic volume change since the elastic volume change recovers during unloading.

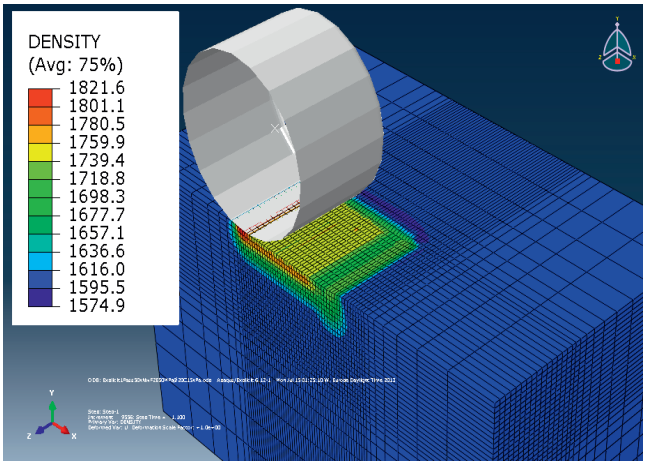

Figure 5.7: View of compaction profile.

The stress components, namely the vertical stress (σ_2), the horizontal stress component in the direction of rolling (σ_1), and the shear stress component (τ_{12}) are shown in Figure 5.8. This particular plot is obtained at a depth of 7.5cm from the surface. As the roller approaches, the lateral stress exceeds the vertical stress. The moment at which the roller stands at the vicinity of the point creates the highest vertical stress, and the shear stress approaches to zero. The response of the stresses from a rolling roller creates rotation of principal stresses in the soil.

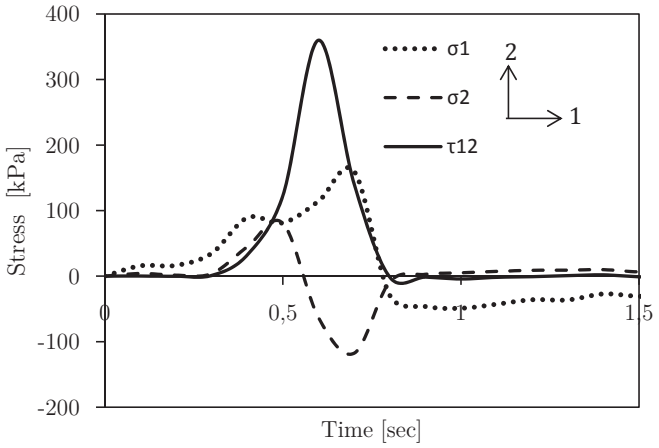

Figure 5.8: Stress components induced due to the load from the rolling roller at a depth of 7.5cm from the surface for a roller weight of 140kN.

Similarly, Figure 5.9a shows the mean stress and corresponding shear stress at a depth of 7.5cm. The change of density in the element located at the same depth is shown in Figure 5.9b. The maximum density is obtained at a critical combination of the mean stress and shear stress. Thereafter, the soil remains intact since volumetric plastic strains are non-recoverable.

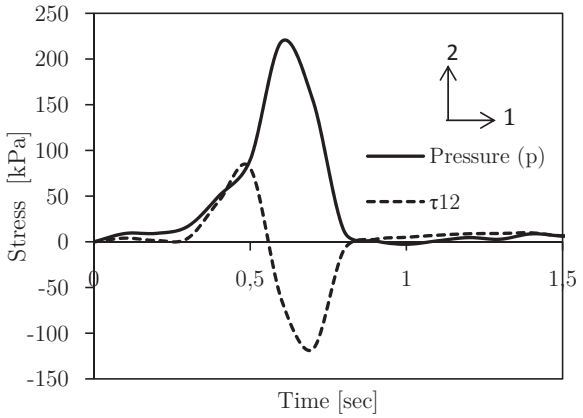

(a)

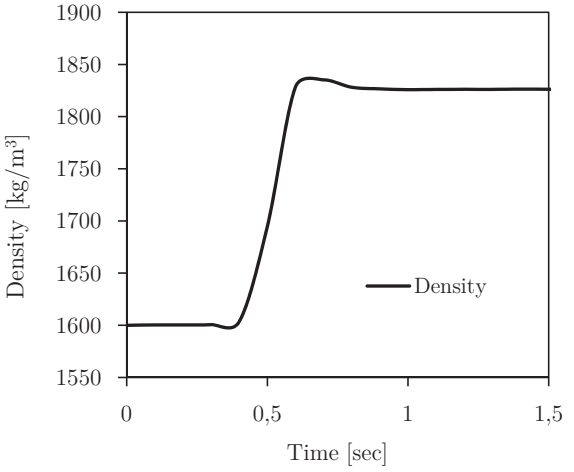

(b)

Figure 5.9: a) pressure (or mean stress)(p) and shear stress (τ) at a depth of 7.5cm from the surface for a roller weight of 140kN, and b) the corresponding change of density.

A more interesting plot that illustrates stress paths and the evolution of the cap surface is presented in Figure 5.10. As the load increases the cap surface expands accordingly. The shear failure limit has been observed to increase as the load limit increases with the same inclination for different loading conditions. The inclination of the yield surface is affected only when the strength parameters such as the friction angle and cohesion are changed.

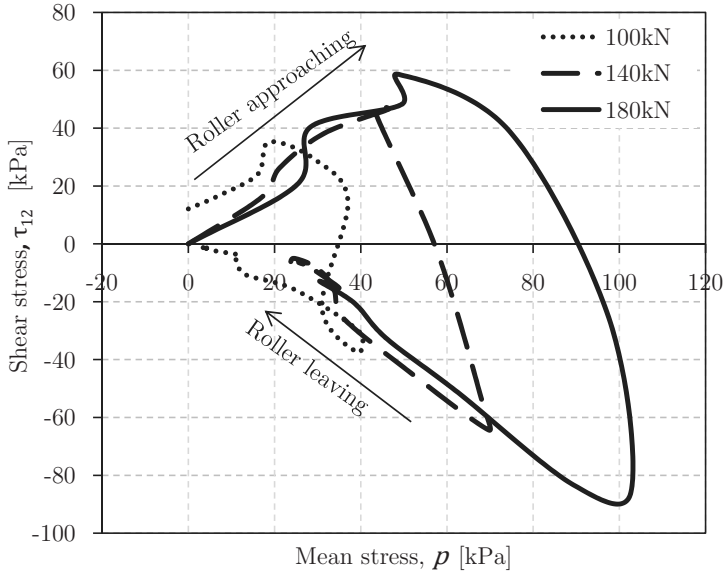

Figure 5.10: Stress paths and evolution of the cap surface.

The effect of the weight of the roller on the depth of compaction is shown in Figure 5.11. It is evident that the effective compaction depth increases as the weight of the roller increases. The relative density (RD), in this case, is defined as the density normalized by the maximum density.

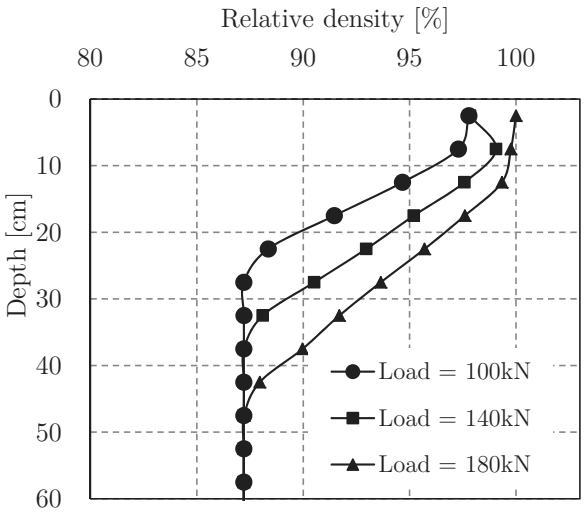

Figure 5.11: Compaction density profile for different weight of roller.

Figure 5.12 shows the effect of friction angle on effective compaction depth for a roller weight of 100kN. The cohesion of the soil is kept constant at 15kPa and the friction angle is varied. A critical height is noted at a depth of 0.3m above which the soil with low friction angle is compacted to a lesser extent. The highest density is obtained for moderate friction angle and the density closer to the surface of compaction reduces for higher friction angle, mainly due to the effect of dilation. Dilation in soils is associated with increase in volume which consequently reduces the density.

It is further noted in Figure 5.12 that the response from ϕ=10° and ϕ=15° is different. This is due to the fact that soils having lower friction angle apparently have high cohesion. Hence, the compaction process is more controlled by cohesion and the depth of compaction is usually small and effective compaction is achieved closer to the surface of compaction where the highest stress located. When the depth of compaction increases, there is no significant change for low friction angle since the compaction depth is controlled by cohesion. At higher values of friction angle, the change in effective compaction depth is small as the soil becomes strong enough and additional compaction effort is required.

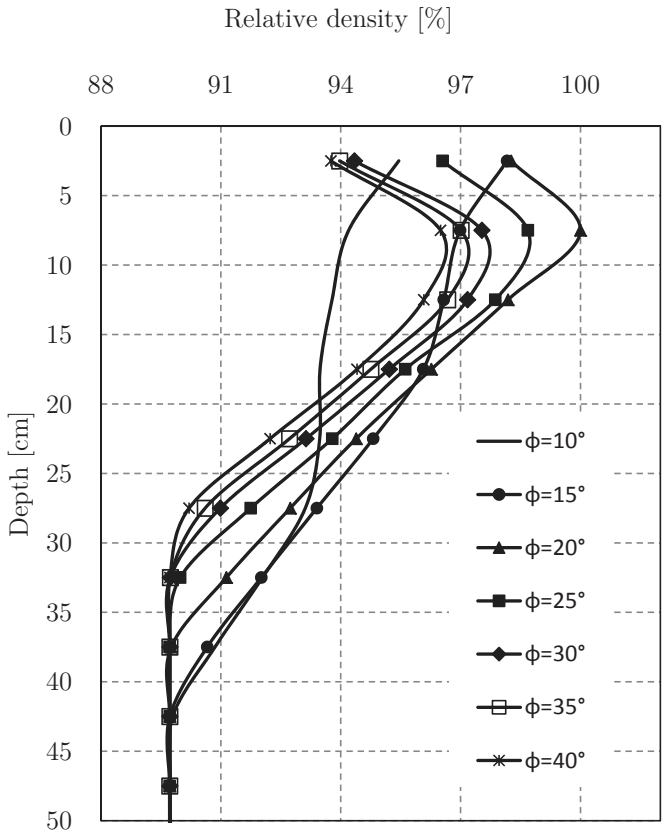

Figure 5.12: The effect of friction angle on soil compaction.

The relationship between the effective depth of compaction and friction angle in Figure 5.13 is obtained from Figure 5.12. For relatively lower relative density (for example at 90%), the soil at low friction angle provides the highest effective compaction depth which gradually decreases as the friction angle increases. When a high relative density is desired (for example at 98%), low effective depth of compaction is obtained, and effective compaction is achieved only for small ranges of friction angle — with the highest value at about 20°. The implication from Figure 5.13 is that the lift thickness depends not only on the strength parameters, but also on the relative density to be achieved in the field.

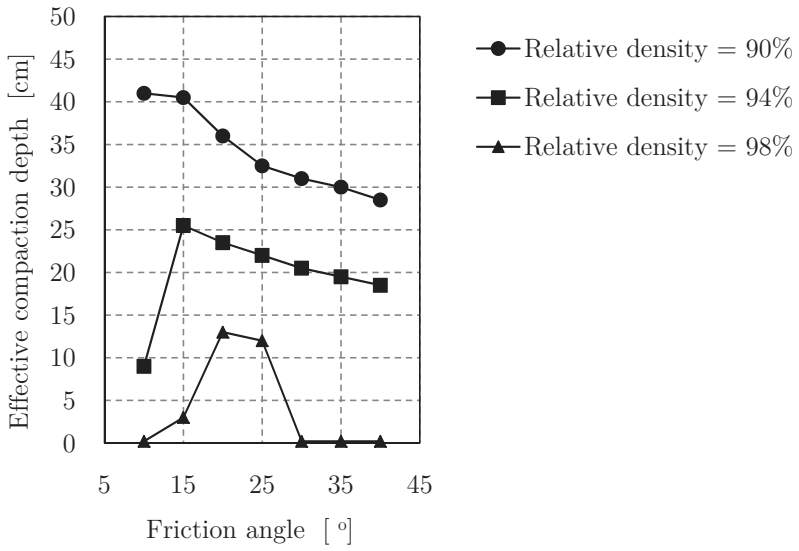

Figure 5.13: Effective compaction depth at different relative densities based on friction angle.

Figure 5.14 presents the relationship between the relative density and cohesion at specific depths in the soil. In this case, the value of friction angle is kept constant at ϕ=20° and the cohesion is varied. The compacted density appears to be independent of the cohesion of the soil in the top 0.1m for high cohesion values. As the depth increases, the effect of cohesion is clearly shown. For the same load, the effective depth of compaction for highly cohesive soils is very limited and it increases as the cohesion deceases.

The direct relationship between the effective compaction depth and soil cohesion is illustrated in Figure 5.15 based on the plot of Figure 5.14. At high relative density, the effective depth of compaction appears to be independent of cohesion for the cohesion values exceeding 15kPa. In this particular case, the lift thickness for high relative density cannot be optimised by varying the cohesion; instead, the weight of the roller should be increased if higher effective compaction depth is desired.

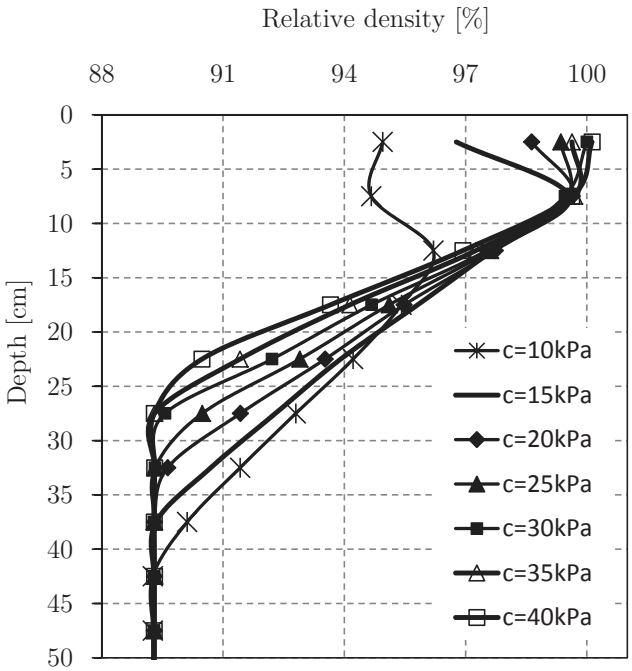

Figure 5.14: The effect of cohesion on soil compaction.

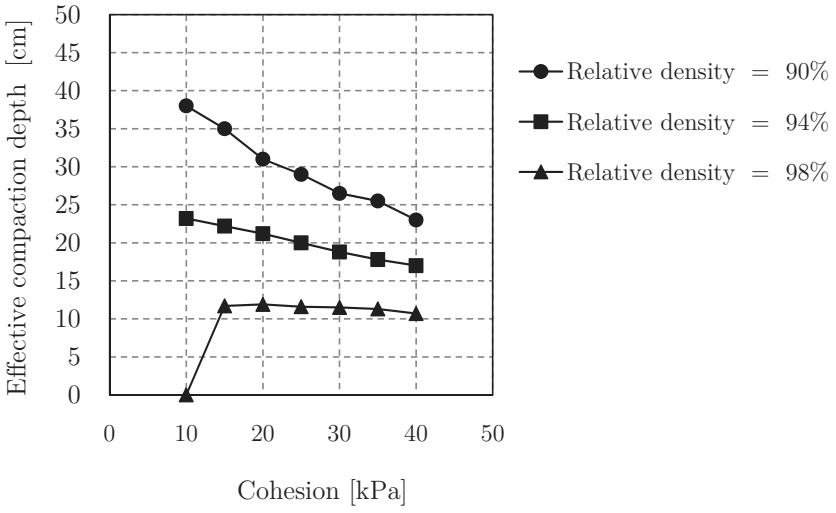

Figure 5.15: Effective compaction depth at different relative densities based on cohesion.

The study presented in this work is carried out using a rate-independent soil model, i.e. it only the stress limits that matters for the response the soil regardless of the rate of application. So the direct implications of vibration roller cannot exactly be represented in this method. Some analytical models [93],[100] are available to model the compaction effect of vibratory rollers despite their practical validity is not well described. Besides the studies emphasised the dynamic features of the roller, not the soil.

There is no robust model available to capture the actual effect of dynamic rollers in soil compaction. The development of new soil modelling techniques such as hypoplastic model [56] has shown an optimistic important features of dynamic soil compaction, for instance the change of vertical acceleration and void ratio.

5.4 Chapter summary

Lift thickness is one of the important factors that affect soil compaction. Hence, compaction cost and machine performance can be optimised with an appropriate choice of lift thickness. Different road agencies have their own specification for the lift height during compaction of pavement foundations which is mainly based on field experience.

In the study presented in this chapter, the effect of soil strength parameters during the compaction process is used as an input to optimise the compaction depth. The rule of thumb in practice is to use a specified lift height for a range of fine-grained soils. Depending on the weight of roller and the required relative density, the lift thickness can be chosen as a function of the strength parameters. Based on the knowledge of the friction angle and cohesion of soils, the rolling strategy can be adjusted and the compaction practice can be improved.

Chapter 6

Prediction of thawing process in frozen subgrade soils

In the previous chapter, one aspect of bearing capacity with optimisation of effective depth of soil compaction has been discussed. This chapter extends description of the challenges of bearing capacity in roads related to environmental factors. The spring thawing is the main theme of this chapter as it is considered to be a major factor that greatly affects bearing capacity of subgrade soils in cold climate regions. The first section discusses the general perspectives of spring thawing in roads. Section 6.2 presents the existing analytical solutions for prediction of the thawing process. Section 6.3 deals with the basic principles of heat transfer mechanism in finite element method. In section 6.4, finite element analysis is carried out for similar assumptions of the analytical solutions, and the results from the two methods are compared. Thereafter, a finite element model is developed for thaw prediction for varying surface temperature and thermal properties of all pavement layers similar to field conditions. The summary of this chapter will be a part of section 6.5.

6.1 Spring thawing

Roads are most prone to deterioration during the spring thaw period, majorly due to the weakening of bearing capacity. Field observations (e.g. [99],[52],[57], and others) showed that the spring season is the critical time at which the moisture balance varies the most. The water accumulated during winter (which exists in ice form below freezing temperature) is released over a relatively short period of

time causing a sharp increase in unfrozen water content in the subgrade soils. At the same time, precipitation and melting of snow accumulated on the shoulders and on the slopes of the embankment contribute to high moisture content in the system through infiltration [33](*Chapter 2, p. 36*).

The cumulative effect may cause an excess pore-water pressure which adversely reduces the strength of soils. Full scale tests conducted at the Vormsund test road [79] showed that the excess pore-water pressure developed during the spring thaw was the primary reason for the reduced bearing capacity. Pore-water pressure of up to 0.90m above the drainage level was registered during thawing.

Figure 6.1 illustrates the variation of the stiffness of the subgrade layer throughout a year. The strength of subgrade soils increases during freezing. In the winter period, the load bearing capacity is appreciably very high. However, there is a risk of cracking in the asphalt layer due to upward stress from heaving of the subsoil layer. As can be seen in Figure 6.1, the loss of subgrade support is critical during the thawing period. Thereafter, the strength is gradually recovered due to dissipation of the excess pore-water pressure and reconsolidation of subgrade soils.

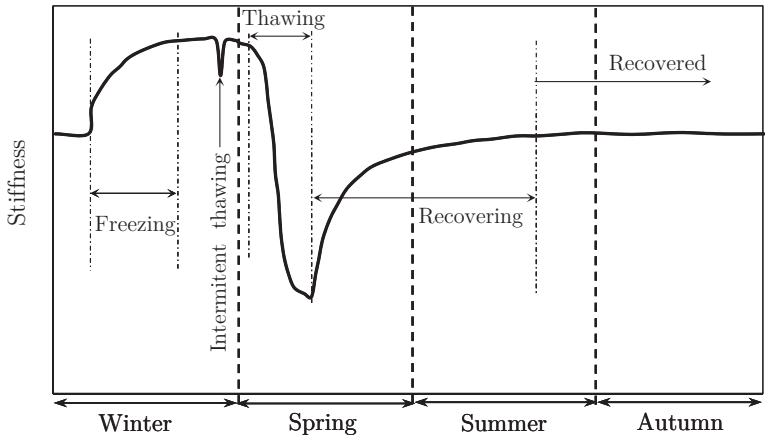

Figure 6.1: Conceptual pavement stiffness variations due to freezing and thawing. Adapted from Erlingsson & Salour [37].

Why the prediction of thawing process is so important? Firstly, prediction of the thawing phenomenon helps to optimize road operation periods in countries which

impose load restriction during spring thawing. Secondly, full-scale tests and field measurements with embedded sensors in subgrade soils are quite demanding. In addition, environmental factors vary from one place to another, and it is not feasible to have direct measurements at many places. Based on relevant field data, analytical and numerical models can be calibrated to perform versatile predications. Thirdly, finite element method (FEM) has been becoming robust in computation of advanced models and coupled analysis for different thermal boundaries and properties of soils similar to the in situ condition. Hence, the effect of environmental factors, and thermal and geotechnical properties of soils on the process of thawing mechanism can easily be studied.

6.2 Analytical solutions for thawing process

6.2.1 Thawing rate

The problem of spring thawing has no exact solution. Analytical solutions for phase transformation based on the theory of heat conduction were presented in Carslaw & Jaeger [21]. In particular for a frozen soil layer, Nixon & McRoberts [78] formulated analytical solutions for the movement of a thawing interface as shown in Figure 6.2. The moving interface starts from the surface in the beginning and it gradually moves downward after the surface temperature is instantly increased.

The properties of the frozen and thawed regions in Figure 6.2 are assumed to be homogeneous and independent of temperature. The formula relating the depth of thawing to the square root of time is given in Equation [6.1].

$$X = \lambda\sqrt{t} \qquad [6.1]$$

Where X is depth of thaw, t is time, and λ is a constant which is obtained from numerical iterations using Equation [6.2].

$$\frac{e^{-\frac{\lambda^2}{4\kappa_u}}}{erf\left(\frac{\lambda}{2\sqrt{\kappa_u}}\right)} - \frac{T_g}{T_s}\frac{k_f}{k_u}\sqrt{\frac{\kappa_u}{\kappa_f}}\frac{e^{-\frac{\kappa_u}{\kappa_f}*\frac{\lambda^2}{4\kappa_u}}}{erfc\left(\sqrt{\frac{\kappa_u}{\kappa_f}}\frac{\lambda}{2\sqrt{\kappa_u}}\right)} = \frac{L\sqrt{\pi}\,\lambda}{2\sqrt{\kappa_u}c_u T_s} \quad [6.2]$$

Where κ_u and κ_f are the diffusivity of unfrozen and frozen soil respectively, k_u and k_f are the thermal conductivity of unfrozen and frozen soil respectively; c_u and c_f are the volumetric heat capacity of unfrozen and frozen soil respectively, L is the volumetric latent heat of fusion of the soil, T_g is the ground temperature, T_s is the applied constant surface temperature, **erf** is the error function, and **erfc** is the complementary error function.

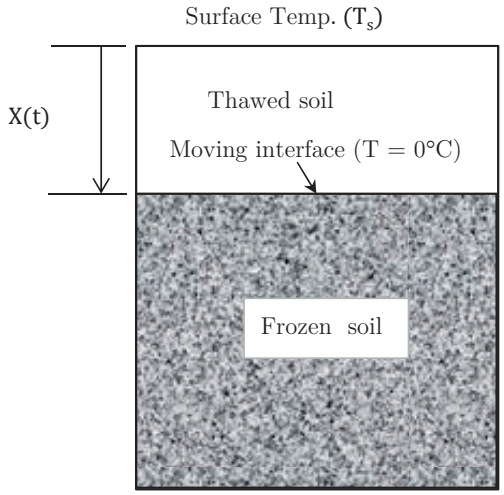

Figure 6.2: The Neumann problem. Adapted from Nixon & McRoberts [78].

In order to ease the difficulty of the rigorous analytical solution in Equation [6.2], Nixon & McRoberts [78] proposed a simplified equation under certain assumptions. The main assumption is that temperature distribution in the frozen zone does not affect the rate of thaw. Hence, by setting $T_g = 0$, Equation [6.2] is reduced to Equation [6.3].

$$\frac{e^{-\frac{\lambda^2}{4\kappa_u}}}{erf\left(\frac{\lambda}{2\sqrt{k_u}}\right)} = \frac{L\sqrt{\pi}\,\lambda}{2\sqrt{\kappa_u}c_u T_s} \qquad [6.3]$$

Assuming a linear temperature distribution in the thawed zone and ignoring the temperature profile in the frozen zone, a dimensionless parameter is obtained from the Stefan's solution as indicated in Equation [6.4].

$$\frac{\lambda}{2\sqrt{\kappa_u}} = \sqrt{\frac{Ste}{2}} \qquad [6.4]$$

Where Ste is the Stefan number which is defined as the ratio of sensible[4] heat to latent heat. It is given by the formula shown in Equation [6.5].

$$Ste = \frac{c_u \Delta T}{L} \qquad [6.5]$$

Where $\Delta T = T_s$ for $T_g = 0.0°C$.

Nixon and McRoberts's semi-empirical model (Equation [6.6]) approximates the thawing constant λ to a higher order of accuracy. The comparison of the three methods (Neumann's exact solution, Nixon and McRobert's semi-empirical model, and the Stefan solution) is shown in Figure 6.3. Nixon and McRobert's semi-empirical model gives similar results to the Neumann's exact solution for the Stefan number, $Ste < 1.0$.

$$\frac{\lambda}{2\sqrt{\kappa_u}} = \sqrt{\frac{Ste}{2}}\left(1 - \frac{Ste}{8}\right) \qquad [6.6]$$

[4] Sensible heat the amount of heat that causes a change in temperature in an object. The temperature rises when the object is heated and falls when the heat is removed.

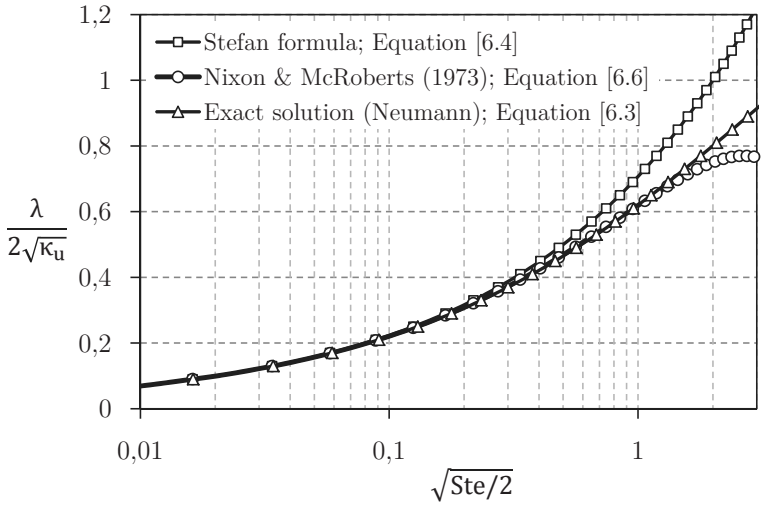

Figure 6.3: Comparison of different solution methods at $T_g = 0$°C.

Jumikis [54] (*Chapter 14, p. 199-202*) showed a mathematical derivation of the Neumann's solution at which it converges to the Stefan's formula and concluded that Stefan's solution is merely a special case of Neumann's theory. In this respect the resemblance of the Stefan method and the Neumann solution is not surprising. It is noted in Figure 6.3 that the simplified methods substantially diverges from the Neumann's exact solution for higher value of Stefan number, i.e. the usage of the simplified methods for thaw prediction should be avoided for the cases of high thermal gradients and soils with low latent heat, for example soils with low degree of saturation.

6.2.2 Excess pore-water pressure

The main cause for weakening of bearing capacity in pavements during spring thawing is excess pore-water pressure. Particularly in low traffic volume roads where the asphalt layer thickness is small, the anticipated stress from the traffic load is high. Consequently, the excess pore-water pressure during thawing increases, partly due to the phase change from the solid state (ice), and partly due to the additional load induced from the traffic. In addition, maintenance budgets of low traffic volume roads are relatively low and appropriate drainage is missing which causes severe cumulative effect on the pavement performance.

The increase in pore-water pressure reduces the effective contact area of particles in soils. Since water does not resist shear forces, the shear strength reduces and plastic strains develop and accumulate as the traffic loads are repeated. The water moves towards the upper layers following the consolidation process. During and after thawing, the soil consolidates due to overburden pressure from the overlying pavement layers. The effect of the traffic load is significant for a sudden increase of excess pore-water pressure. Nonetheless, traffic load is transient and its effect on the reconsolidation process may not be pronounced.

The excess pore-water pressure at the moving interface in Figure 6.2 is obtained by linear theory of thaw-consolidation. For the of self-weight loading only, Nixon [77] proposed a linear profile of excess pore pressure with depth as shown in Equations [6.7] and [6.8].

$$u = B\gamma' x \tag{6.7}$$

$$B = \frac{1}{1 + \frac{1}{2R^2}};\ R = \lambda/(2\sqrt{c_v}) \tag{6.8}$$

Where B is a dimensionless physical is constant, γ' is a submerged unit weight of the soil, x is the location of the thawing interface from the surface, c_v is the coefficient of consolidation of soil, λ is a constant determined by numerical iterations from Equation [6.2].

6.2.3 Limitation of analytical solutions

The analytical methods fail to capture the actual mechanism of thawing in the field — for instance, varying thermal boundaries and non-homogeneous pavement layers. To some extent, the use of FEM overcomes the major limitations of the analytical methods. Nowadays, material models based on coupled analysis of two different physical processes provide a more reliable results and predictions. Nonetheless, erroneous solutions obtained from FEM are not uncommon due to limited knowledge of modelling techniques. In the following section, similar models and assumptions on the basis of analytical solutions are used to establish the platform of modelling techniques using FEM. The results of the finite element

analysis and the analytical solutions are compared, and further modelling techniques considering the actual field conditions are presented.

6.3 Finite element analysis

In recent years, some advanced finite element programs have provided features for solving multi-physics problems, where the response of the system is affected by the interaction between several distinct physical fields such as heat transfer, deformation, pore pressure and others. In this study, the coupled temperature-pore pressure elements in Abaqus FEA [104] are used to solve the heat transfer equation in addition to and in a fully coupled manner with the continuity and mechanical equilibrium equations. Temperature is used as additional degree of freedom in addition to pore pressure and displacement components. In Abaqus, heat transfer due to conduction in the soil skeleton and pore fluid, as well as convection in the pore fluid can be modelled. In order to compare the numerical results with the analytical solutions, only heat transfer due to conduction is assumed.

In saturated soils, the latent heat absorbed or released on the freeze-thaw front has a major impact on the rate of thawing. In the numerical scheme, the latent heat can be defined in two ways [116]. It can be included in the heat conduction equations or it can be defined by using temperature dependent specific heat as shown in Figure 6.4. To ensure the accuracy of this method, the time increments or the maximum temperature change in each increment should be limited to assure the energy balance and a uniform temperature field is defined as initial condition. The latent heat of fusion is assumed to be released between -0.1°C and 0.0°C. Some variables for “predefined fields” in Abaqus are defined, for instance geostatic stress, initial temperature state of the frozen soil, initial void ratio, and initial degree of saturation. Detailed procedures for defining the “predefined fields” and “initial conditions” and thermal boundary conditions are available in the user’s, analysis and theory manuals of Abaqus FEA [104].

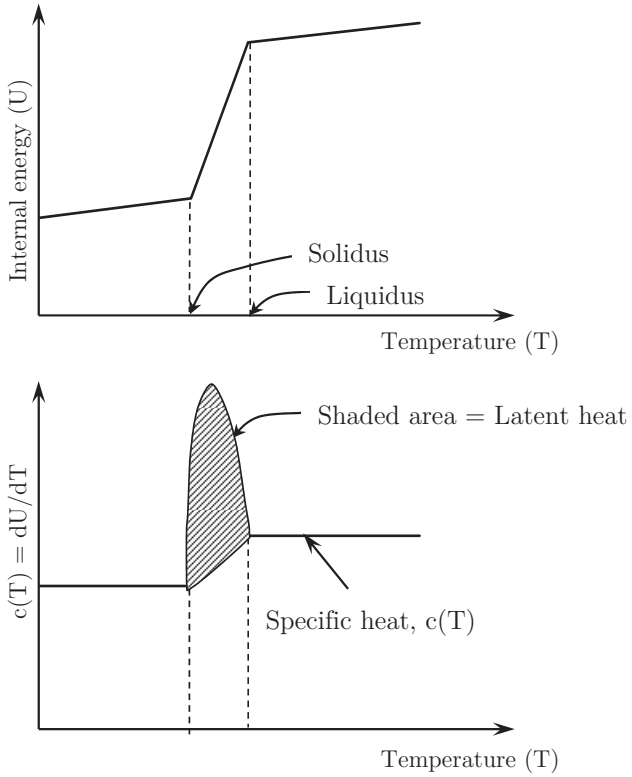

Figure 6.4: Specific heat, latent heat definition. Adapted from Abaqus FEA [104].

Abaqus provides two analysis methods for heat transfer problems, namely uncoupled and coupled heat transfer analyses. In the uncoupled analysis, the temperature field is calculated without consideration of other fields in the bodies, such as stress-deformation field. The analysis includes conduction, boundary convection and boundary radiation. It can also be transient or steady-state, linear or nonlinear. The nonlinearity heat transfer analysis can be due to temperature dependent material properties or nonlinear boundary conditions. For example, when the latent heat effects are included, the analysis may be severely nonlinear.

The coupled analysis, on the other hand, provides simultaneous procedures at which the mechanical and thermal solutions affect each other. The application of coupled analysis is very significant in geotechnical problems. Soils are porous

material, and the pore fluid (commonly water) highly influences stresses in the soil mass. Abaqus provides the possibility to combine the effect of temperature in the coupled pore fluid diffusion and stress analysis. The coupled analysis gives the option to model heat transfer due to conduction in the soil skeleton and the pore fluid, and convection due to the flow of the fluid, through the use of coupled temperature-pore pressure displacement elements.

6.4 Thawing of homogeneous frozen layer

In this section, we start from analysis of simplified geometric models to compare the results from finite element analysis and analytical methods. This is because of two reasons. One, the analytical solutions are known and well established for homogeneous layers and simplified boundary conditions, for example a constant surface temperature. Two, the analytical methods are used in this study to control the prediction capability of finite element method. Once we gain experience for simplified models, we can easily extrapolate the modelling techniques for multi-layer systems and varying thermal boundary conditions, similar to pavements. Some key assumptions are made in both analytical method and FEM — the frozen soil is fully saturated, the heat transfer mechanism is only by conduction, and the thermal conductivity of the soil is isotropic.

6.4.1 Analytical solution versus uncoupled finite element analysis

Carslaw & Jaeger [21] (*Chapter 11, p. 282-298*) presented the generalized Neumann's solution of heat transfer analysis that accounts for a substance with a transformation point at which it changes from one phase to another with emission or absorption of heat. The analytical solutions for the case of thawing of frozen soils have been shown in Equations [6.1] and [6.2]. This method treats the bulk soil mass as a single entity i.e. properties of soil grains and the pore-water are not included separately. Hence, based on similar input parameters, the thaw prediction using the analytical solution and FEM (uncoupled analysis) should provide similar results. It must be noted that the specific heat and latent heat of fusion are defined in volumetric basis in the analytical method, while in mass basis in Abaqus FEA. Hence, the density is used as a converting factor to use consistent values in both methods. The input data shown in Table 6.1 is used for analysis.

Table 6.1: Assumed[5] input data for analytical solution and uncoupled finite element analysis.

Parameters	Analytical method	FEM (Abaqus)
Bulk density	1800.0 kg/m^3	1800.0 kg/m^3
Thermal conductivity (unfrozen)	1.0 J/m*s*°C	1.0 J/m*s*°C
Specific heat (unfrozen)	1800000.0 J/m^3*°C	1000.0 J/kg*°C
Latent heat	170000000.0 J/m^3	94444.4 J/kg
Ground temperature (T_g)	0.0°C	0.0°C
Surface temperature (T_s)	12.0°C	12.0°C

The geometric model is shown in Figure 6.5. An axisymmetric model is chosen with 2.0m width in lateral direction and 1.0m in thickness. The analytical solutions are derived based on semi-infinite half space. Hence, relatively small elements are used in meshing of the finite element model to minimize the effect of infinite boundaries considered in the analytical solutions. In Abaqus, DCAX4 (Abaqus designation for 4 node axisymmetric heat transfer elements) are used for the uncoupled analysis. The initial ground temperature is set to be 0°C in all elements. Then the surface temperature is instantly increased to 12.0°C.

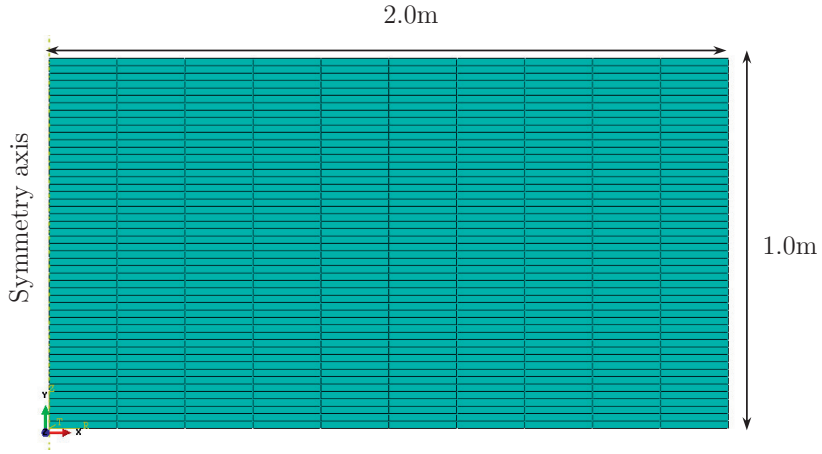

Figure 6.5: Finite element mesh for one-dimensional thawing of a frozen soil layer.

[5] The values are estimated to verify the results from FEM using an analytical solution.

Figure 6.6 illustrates the nodal temperature distribution of one-dimensional thawing at different time steps. The moving thawing interface (rate of thawing) is obtained from observation of the time step at which the nodal temperature changes from negative value (in °C) to positive value (in °C). Figure 6.7 shows the comparison of the results obtained from finite element modelling (uncoupled heat transfer analysis) and Neumann's analytical solution. The results from the two methods show a very good agreement. The slightly small difference at higher thawing depths arises possibly due to the assumption that $T_g = 0$°C is used for the analytical solution; while $T_g = -0.15$°C is considered for the finite element analysis to ensure that the latent heat of fusion from ice to water is utilized to define the phase change in the soil pores.

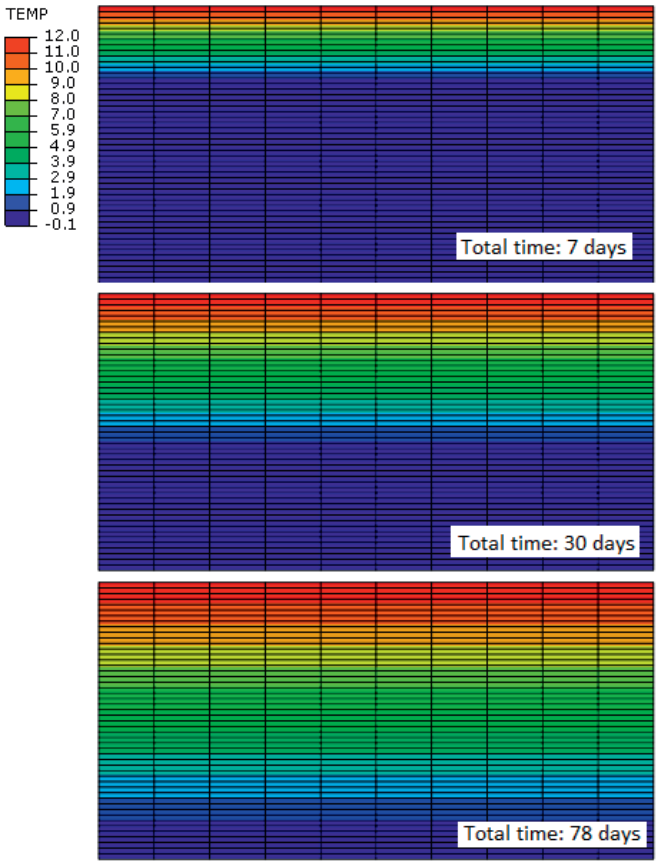

Figure 6.6: Temperature distribution in one-dimensional thawing at different time steps (NT: Nodal temperature).

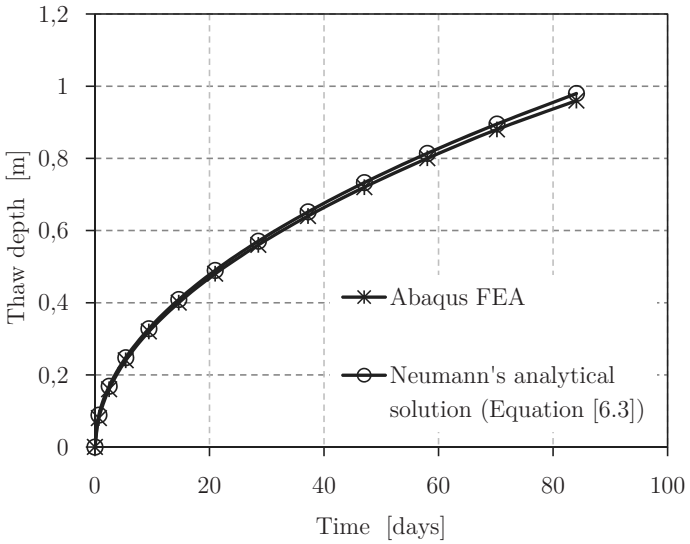

Figure 6.7: Comparison of analytical heat transfer analysis with FEM. Note that the FEM is this case is only heat transfer (uncoupled) analysis.

The uncoupled analysis, however, does not provide an explicit overview of the volume of the void in the soil and the properties of water in its solid and liquid state. The latent heat of fusion absorbed or released during freezing/thawing process mainly depends on the amount of available water in the pore of the soil. Hence, the analysis of the thawing process must incorporate the void ratio, the degree of saturation, and the amount of frozen water for realistic simulation closer to field conditions. This will be a part of the next section.

6.4.2 Analytical solution and finite element coupled analysis

In contrary to the uncoupled finite element analysis dealt in section 6.4.1, the coupled finite element modelling considers the effect the thermal and physical properties of the pore-water. However, the analytical solution used for verification is valid for the assumption of the frozen bulk soil as homogeneous frozen layer. In Abaqus, the input properties of the pore fluid and the soil grains are obtained separately, and the program computes for the bulk soil for the given void ratio and degree of saturation. In order to compare the results of analytical and the

coupled analysis, the methods of determining the properties of bulk soil mass from given properties of pore-water and soil grains are presented.

Latent heat of fusion

Abaqus: The latent heat of fusion upon thawing is only required to thaw the frozen water in the frozen soil. In the coupled analysis, only the latent heat of water (i.e. 334kJ/kg) is defined.

Analytical solution: The volumetric latent of heat of fusion for the analytical solution is computed based on the water content and dry density of the soil [78],

$$L = \rho_d * \frac{w}{100} * \left(1 - \frac{w_u}{100}\right) L_w \qquad [6.9]$$

Where L_w is the latent heat of water (kJ/kg), w_u is the unfrozen water content (%), w is the water content (%), and ρ_d is the dry density of the soil (kg/m^3).

Once the frozen soil is thawed, for fully saturated soils, a reasonable relationship between the void ratio and water content can be made as shown in Equation [6.10].

$$e = \frac{w}{100} * G_s \qquad [6.10]$$

Where e is the void ratio; G_s is the specific gravity of the soil.

Heat capacity

Abaqus: The specific heat of soil grains and water are the required inputs in Abaqus.

Analytical solution: In the analytical solution, the specific heat is defined in volumetric basis. The volumetric heat capacity of a frozen soil (c_f) is calculated by summing up the relative heat capacities of the constituent materials [78].

$$c_f = \rho_d \left[c_m + 0.5 c_w \left(1.0 + \frac{w_u}{100} \right) \frac{w}{100} \right] \quad [6.11]$$

Where c_f is the volumetric heat capacity of frozen soil, ρ_d is the dry density of the soil (kg/m^3), c_m is the specific heat of the soil grains (J/kg*°C), c_w is the specific heat of water (J/kg*°C), w_u the unfrozen water content (%). Note that 0.5 in Equation [6.11] accounts for the assumption that the specific heat of ice is about half of the specific heat of water.

Similarly, the volumetric heat capacity of a thawed soil (c_u) is estimated from Equation [6.12].

$$c_u = \rho_d \left(c_m + c_w \frac{w}{100} \right) \quad [6.12]$$

Thermal conductivity

Abaqus: The thermal conductivity of the soil grains and water are the required input.

Analytical solution: The thermal conductivity of the bulk soil mass is approximated from the individual components. In this study, the average thermal conductivity for the frozen and unfrozen soils is obtained from Kersten's empirical equations [Kersten (1949)] cited in Farouki [38]—shown in Equations [6.13] and [6.14]. For the frozen soil, it is further assumed that all water in the soil exists as ice. For clay and silt,

$$k_u = 0.1442 \, (0.91 \log w + 0.2) \times 10^{0.6243 \rho_d} \quad [6.13]$$

$$k_f = 0.001442 \, (10^{1.373 \rho_d}) + 0.01226 w \, (10^{0.4994 \rho_d}) \quad [6.14]$$

Where k_u is thermal conductivity of thawed (unfrozen) soil (J/m*s*°C), k_f is thermal conductivity of the frozen soil (J/m*s*°C), and ρ_d is the dry density (g/cm^3).

Table 6.2 summarises the thermal properties of fine-grained subgrade soils. Some of the thermal properties are obtained from literature [90],[91],[12],[104],[38], while the physical/geotechnical parameters are reasonably approximated for a typical fine grained (silty-clay) soils.

Table 6.2: Input parameters the coupled finite element analysis and analytical solution.

Parameter	Abaqus coupled analysis	Analytical solution
Bulk density (ρ, in kg/m^3)	1800.0	
Void ratio (e)	1.0	
Saturation (S, in %)	100.0	
Specific density of soil grains (G_s)	2.7	
Water content (w, in %)		37.0; from Equation [6.10]
Dry density (ρ_d, in kg/m^3)		1313.5
Specific heat		
- Soil grains (c_s; in kJ/kg*°C)	0.71	
- Water (c_w; in kJ/kg*°C)	4.20	
- Ice (c_{ice}; in kJ/kg*°C)	2.05	
- Volumetric heat capacity for frozen state (c_f; in kJ/m^3*°C)		1930.0 ; Equation[6.11]
- Volumetric heat capacity for unfrozen state (c_u; in kJ/m^3*°C)		2975.8 ;Equation [6.12]
Latent heat		
- Water/ice (L_w; in kJ/kg)	334.0	
- Soil grains	0.0	
- Bulk soil mass (L; in kJ/m^3)		162490.0;Equation [6.9]
Thermal conductivity (J/m*s*°C)		
- Water	0.6	
- Ice	2.2	
- Soil grains	2.7	
- Frozen soil (for analytical solution)		2.14; Equation [6.13]
- Thawed soil (for analytical solution)		1.53; Equation [6.14]

For the coupled analysis in Abaqus, the following additional parameters are defined.

Table 6.3: Additional input parameters for coupled analysis in Abaqus.

Parameter	Values
Stiffness E (MPa) and Poisson's ratio,ν	40.0MPa and 0.45 for $T > 0$°C 400.0MPa and 0.3 for $T \leq 0$°C
Coefficient of thermal expansion	9.67×10^{-6}
Pore fluid expansion coefficient	5.1×10^{-5} for $T \leq 0$°C -1.67×10^{-5} for $T = 0$°C 0.0 for $T = 4$°C 2.933×10^{-5} for $T \geq 12$°C
Consolidation coefficient (m^2/s)	1.0×10^{-6}
Permeability (m/s)	1.0×10^{-7} for $T > 0$°C 1.0×10^{-14} for $T \leq 0$°C

The finite element model for coupled analysis of the thawing process is shown in Figure 6.8. One-dimensional thawing is assumed, i.e. thawing starts at the top and then advances downwards. A 2m wide and 1m thick axisymmetric model is divided in fine meshes in the direction thawing to increase the accuracy of the results from FEM. The coupled analysis uses first-order reduced integration fully coupled elements "CAX4RPT" (Abaqus designation for 4 node bilinear displacement, pore pressure, and temperature axisymmetric elements). The input parameters shown in Tables 6.2 and 6.3 are used. The physical and thermal properties of the soil and water are considered to depend on temperature. Both the soil and water are assumed to undergo thermal expansion associated with temperature variation. In the finite element analysis, the latent heat is assumed to be released between -0.15°C and 0.0°C.

The initial temperature (T_g) and initial void ratio (e) are assumed to be uniformly distributed at all nodes in the model. In this particular analysis, the soil is assumed to be fully saturated and the initial pore-water pressure of the frozen soil is set to be 0.0. As shown in Figure 6.8, all outer surfaces except the top surface are restrained from moving in a perpendicular direction. A surface temperature ($T_g = 12°C$) is suddenly applied on the top surface and remains constant. The top surface allows drainage and the pore-water is kept to be 0.0 throughout the analysis.

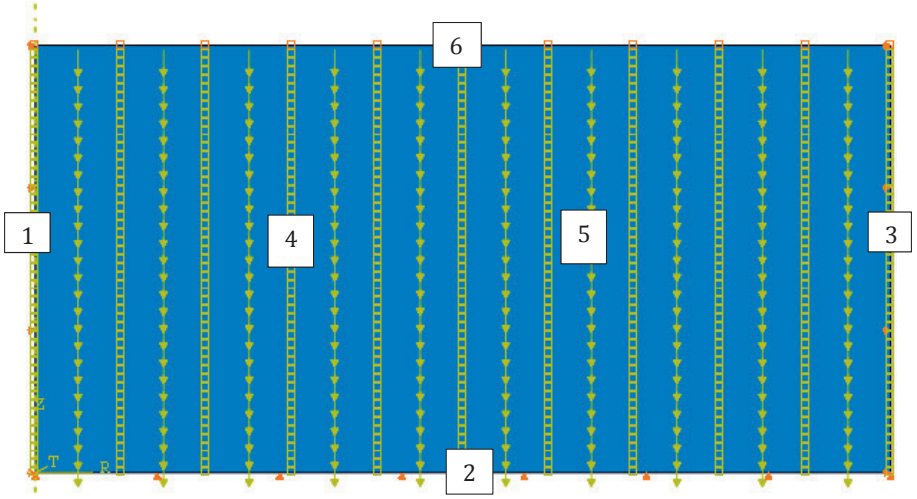

1: axis of symmetry (rotation/deformation)
2/3: deformation boundary conditions (rotation/deformation)
4: initial temperature, void ratio, and saturation of the frozen soil.
5: self-weight of the soil
6: surface thermal boundary

Figure 6.8: Finite element model: boundary conditions and predefined variables for the coupled analysis. Note that the geometric dimensions and meshes are similar to Figure 6.5.

Figure 6.9 shows that the rate of thaw determined from the coupled finite element analysis is slightly higher than the prediction from the Neumann's analytical solution. Comparing to the number of assumptions made to match the input values in the two methods, the prediction capability of the coupled analysis is

well accepted. The coupled finite element analysis is more appealing and superior to the analytical solution since it gives the possibility to define the pore-water properties, the void ratio, and saturation which are some of the key ingredients in the analysis of thawing in frozen soils.

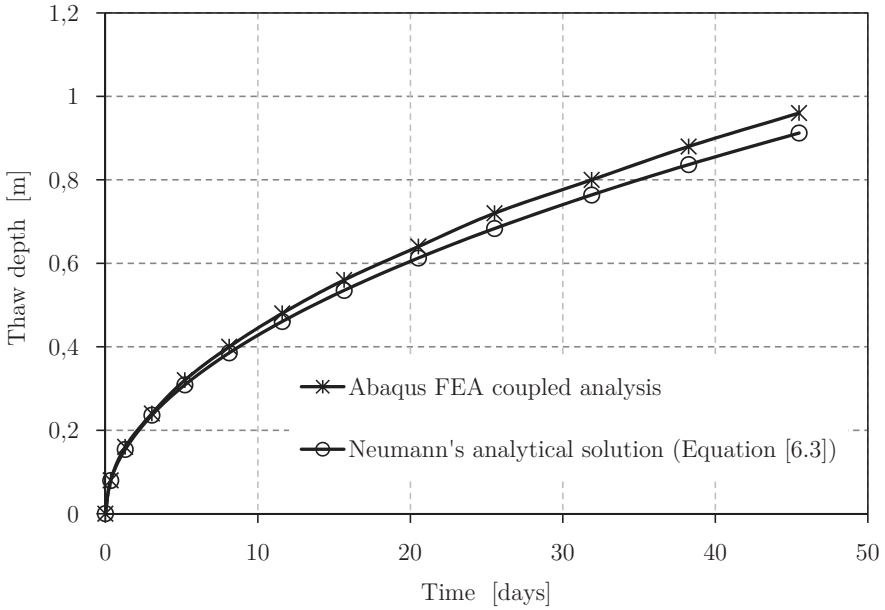

Figure 6.9: Comparison of analytical solution (Neumann's solution at $T_g = 0°C$) with finite element analysis.

6.4.3 Excess pore-water pressure

Another feature of the coupled analysis in Abaqus is to predict the development of excess pore-water pressure associated to the thawing process. The prediction of excess pore-water pressure is also carried out using the analytical solution from Nixon [77] shown in Equations [6.7] and [6.8] based on the input parameters given in Table 6.4. Although traffic loads increase the magnitude of excess pore-water pressure, they have only a transient effect, i.e. they do not affect the consolidation process. Consolidation in subgrade soils is majorly due to the weight of the soil itself and the overburden pressure from the overlying pavement structures.

Table 6.4: Input parameters for analytical solution and FEM.

Analytical solution ; Equations [6.7] and [6.8]	Parameters	value
	Consolidation coefficient (m^2/s)	1.0×10^{-6}
	Permeability (m/s)	1.0×10^{-7}
	Thermal properties	Given in Table 6.2
FEM	Given in Table 6.2 and Table 6.3	

Table 6.5 shows the normalized pore-water pressure for self-weight loading only from Nixon's analytical solution. The values are obtained when the thaw interface reaches at a depth of 0.5m from the surface. The results indicate that the pore-water pressure increases as the surface temperature increases.

Table 6.5: Excess pore-water pressure obtained from analytical solution

Location of thaw interface (x) in [m]	Ground temperature (T_g) in [°C]	Surface temperature (T_s) in [°C]	λ [-]	Normalized excess pore-water pressure ($u/\gamma' x$)
0.5	0.0	6	0.000358	0.0603
0.5	0.0	12	0.000498	0.1104
0.5	0.0	18	0.000600	0.1528

The excess pore-water pressure from the coupled finite element analysis is illustrated in Figure 6.10. To consider the effect of self-weight loading similar to the analytical solution, gravity loading is defined with distributed load type BZ (in Abaqus). Hence, the pore-water pressure obtained from the coupled analysis in Abaqus is the pore pressure in excess of the hydrostatic pressure required to support the weight of pore fluid above the particular point in consideration. In contrary to the analytical solution, the FEM analysis provides peak excess pore-water pressure independent of the magnitude of the surface temperature. The main reason for this is that the initial rise of the pore pressure depends primarily on the differential expansion of the water relative to the pores in the soil.

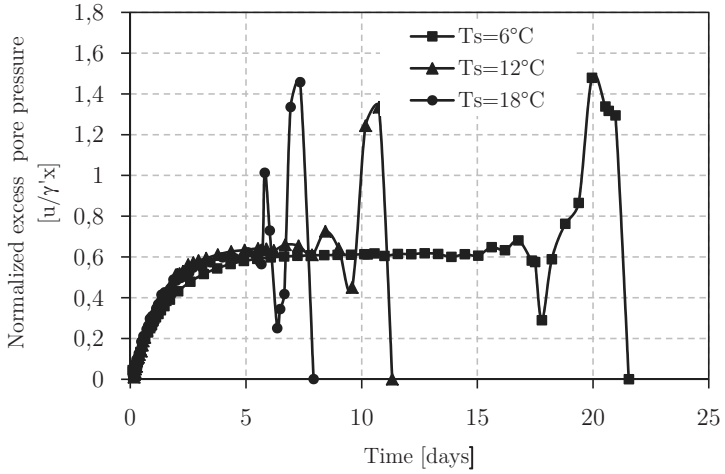

Figure 6.10: Pore-water pressure generated during thawing at a depth of 0.5m from surface using coupled analysis in Abaqus.

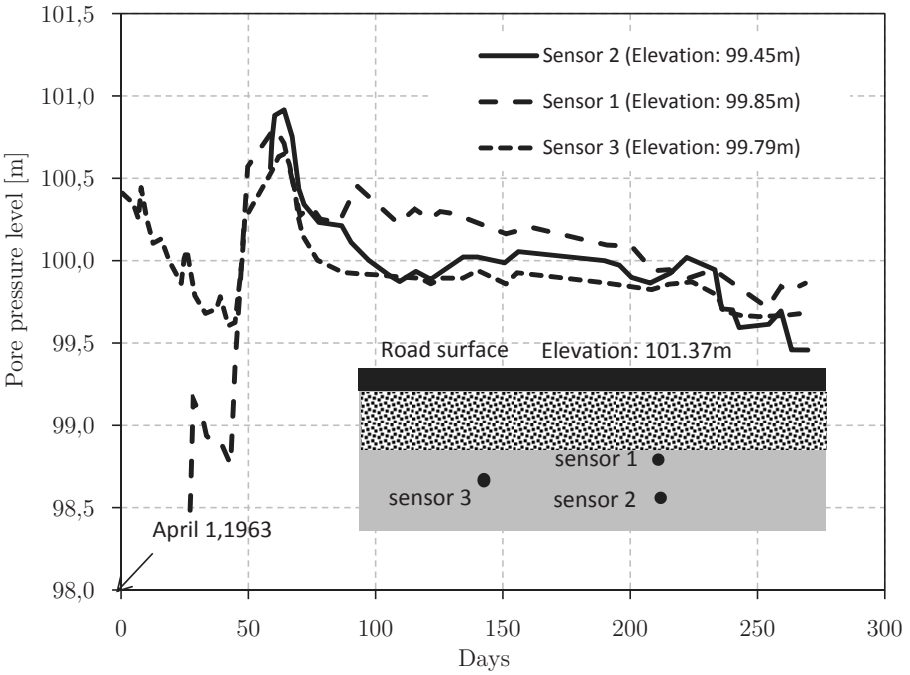

Figure 6.11: Field measurements of excess pore-water pressure during the Vormsund test road project. Adapted from Nordal & Hansen [79] (p. 34).

The numerical analysis (Figure 6.10) has shown the abrupt change of pore-water at the instant of release of the latent heat. The excess pore-water then diminishes depending on the differential expansion of the water relative to the pores in the soil. Interestingly, this kinds of response of excess pore-water pressure were observed from full scale field monitoring of thawing and freezing process during the Vormsund test road project, reported in Nordal & Hansen [79]. The prevailing results from the Vormsund test road are direct measurements of the pore-water pressure. Other field measurements [53],[99] (see Figure 6.12 as well) measured the change of volumetric water content instead of the pore-water pressure. The sudden rise and fall of the volumetric water content were consistent with the particular period at which the phase change of frozen water is expected.

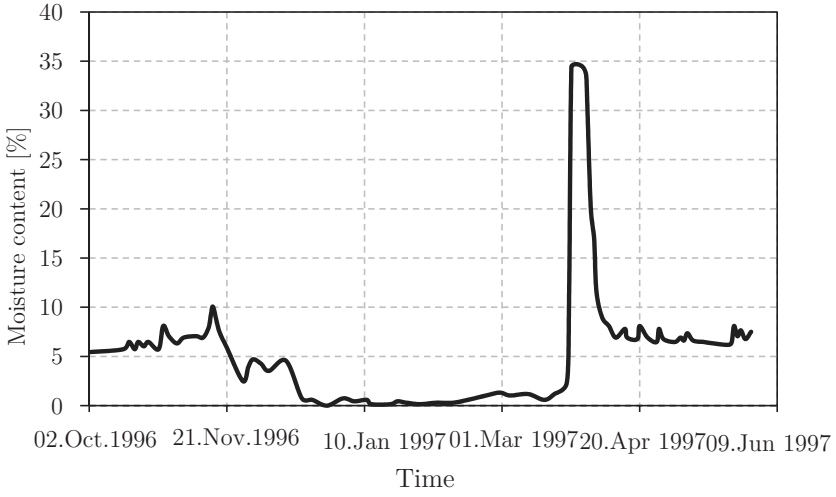

Figure 6.12: Unfrozen volumetric moisture content in the subgrade soil (AASHTO soil classification: A-2-4), measured at a depth of 584mm from the pavement surface. Adapted from Janoo & Shepherd [52].

In the study presented in this section, the finite element modelling techniques of the thawing process are well established. The prediction of rate of thawing has fairly been accurate enough. The excess pore-water prediction of neither the analytical method nor the coupled finite element analysis gives a conclusive solution.

In the following sections, FEM is mainly considered for actual field conditions of pavement structures. A multi-layer pavement structure is modelled and the

thermal and physical property of each layer is defined. Moreover, a varying surface temperature is used. The method of using actual temperature measurements (weather data) into FEM is explained in section 6.4.4.

6.4.4 Weather data and thermal properties of pavement layers

The variation of surface temperature is considered in the numerical analysis of the thaw advancement. The abrupt change of temperature creates numerical difficulties in the numerical simulation of the coupled analysis. Hence, the weather data is converted to a smooth periodic function using the Fourier transformation as shown in Appendix A.

Surface temperature variation undergoes approximately simple periodic fluctuations on both a daily and an annual cycle. In this study, the weather data from average daily temperatures have been used. The weather data from Katsøy station (in Sør-Trøndelag) is obtained from *www.senorge.no*. The meteorological data and the approximated periodic temperature variation are shown in Figure 6.13.

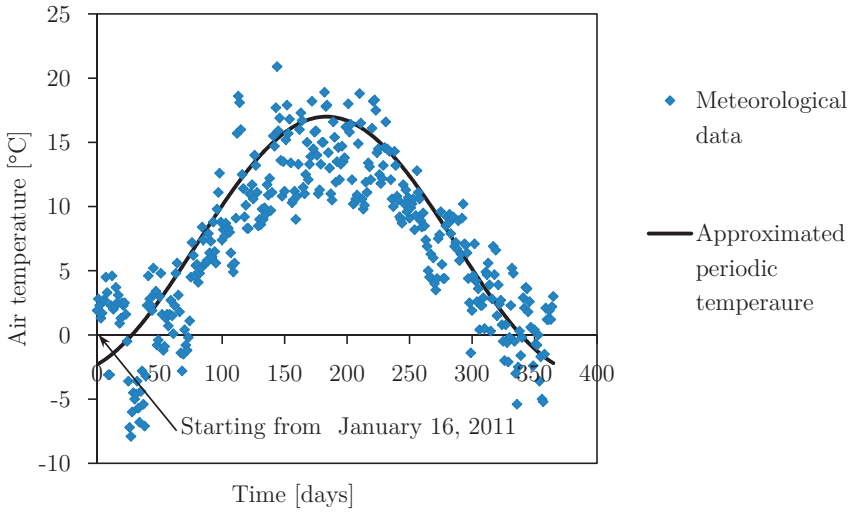

Figure 6.13: Varying surface temperature from actual weather data for the coupled finite element analysis.

A general hypothesis of the apparent sinusoidal curve is established in Equation [6.15].

$$F(t) = c_1 * \cos\left(\frac{w_n * \pi * t}{180} + c_2\right) + c_3 \qquad [6.15]$$

Where the coefficients c_1, c_2 and c_3 are calibrated to match with the sinusoidal curve.

The coefficients are then calibrated to obtain a good fit to the weather data as shown in Figure 6.13. Finally, the following values are obtained: $w_n = 0.00001$, $a = 10.0$; $b = 9.80$, and $c = 7.0$. It is noted that the designation of Fourier series (Equation [6.16]) in Abaqus is slightly different from what has been presented in are adjusted for the numerical input as shown in Table 6.6.

$$a = A_0 + \sum_{n=1}^{N} [A_n \cos n\omega(t - t_0) + B_n \sin n\omega(t - t_0)] \quad \text{for } t \geq t_0$$
$$a = A_0 \quad \text{for } t < t_0 \qquad [6.16]$$

Where t_0, N, ω, A_0, A_n, and B_n, $n = 1,2,\cdots,N$ are user-defined constants.

Table 6.6: Input parameters for varying surface temperature.

Parameters	Equations from Appendix A	Abaqus FEA Equation [6.16]
Period Angular frequency	$T = 36000000.0$	 $\omega = 1.7453 \times 10^{-7}$
Initial amplitude	$a_0 = 14.0$	$A_0 = 7$
Fourier coefficients	$a_1 = -9.304$	$A_1 = -9.304$
	$b_1 = 3.665$	$B_1 = 3.665$
	$a_2 = 0.0$	$A_2 = 0.0$
	$b_2 = 0.0$	$B_2 = 0.0$

6.4.5 Coupled finite element analysis for multi-layer system

Based on the modelling techniques obtained in section 6.4.2, a typical muli-layer pavement structure is developed as shown in Figure 6.14. The initial temperature of the asphalt, base/subbase and frozen subgrade is set to be -2.3°C. The thermal and physical properties of the subgrade soil are obtained from Tables 6.2 and 6.3. Table 6.7 presents the type of elements used for numerical simulation, and Table 6.8 summarises the thermal and physical parameters for asphalt and aggregates.

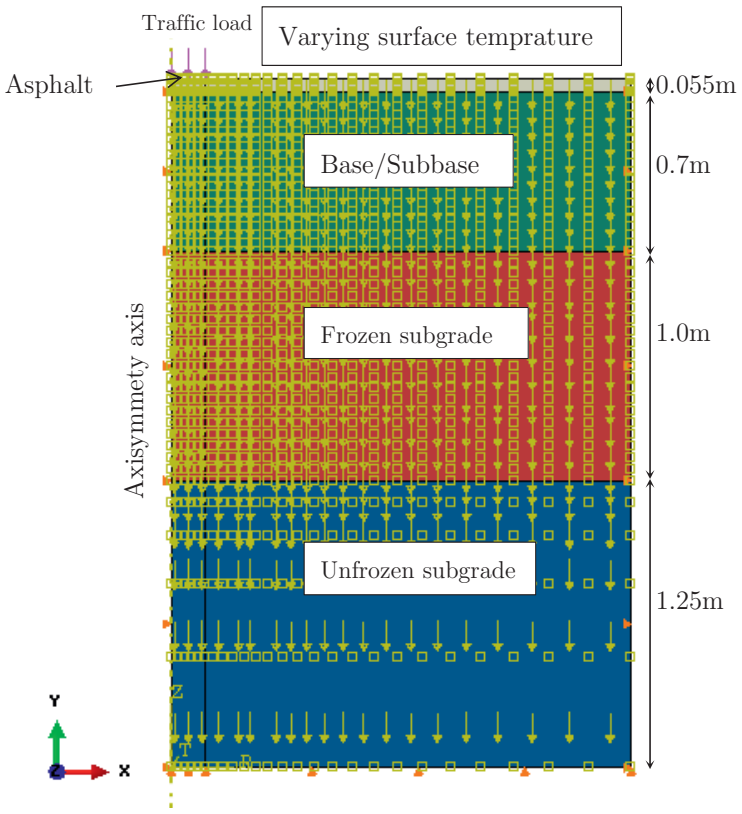

Figure 6.14: Finite element model with thermal and boundary conditions similar to a typical in situ pavement section.

Table 6.7: Element type used in finite element analysis.

Layer	Type of element	Abaqus FEA designation
Asphalt	Coupled temperature – displacement	CAXRT
Base/subbase	Coupled temperature – displacement	CAXRT
Frozen subgrade	Coupled pore pressure – temperature	CAX4RPT
Unfrozen subgrade	Coupled pore fluid/stress	CAX4P

Table 6.8: Thermal input parameters for asphalt and aggregates.

Parameters	Asphalt concrete	Aggregates
Thermal conductivity (J/m*s*°C)	1.5	1.3
Specific heat (kJ/kg*°C)	0.92	0.85
Coefficient of thermal expansion (°C)	4.0×10^{-5}	3.0×10^{-6}
Density (kg/m^3)	2100	1800
Stiffness E (MPa)	15000.0 for $T \leq 0$°C 10000 T = 5°C 8000 T = 10°C 6000 T = 20°C 3000 T = 30°C 1000 T = 40°C	300
Poisson's ratio (ν)	0.3	0.3

(Source: Typical values are selected based on the overview of Jumikis [54] (p.344-345), NCHRP [74](p. 2.3.14 -2.3.17), Doré & Zubeck [33](p. 225), Tayebali *et al.* [106] (p. 13).

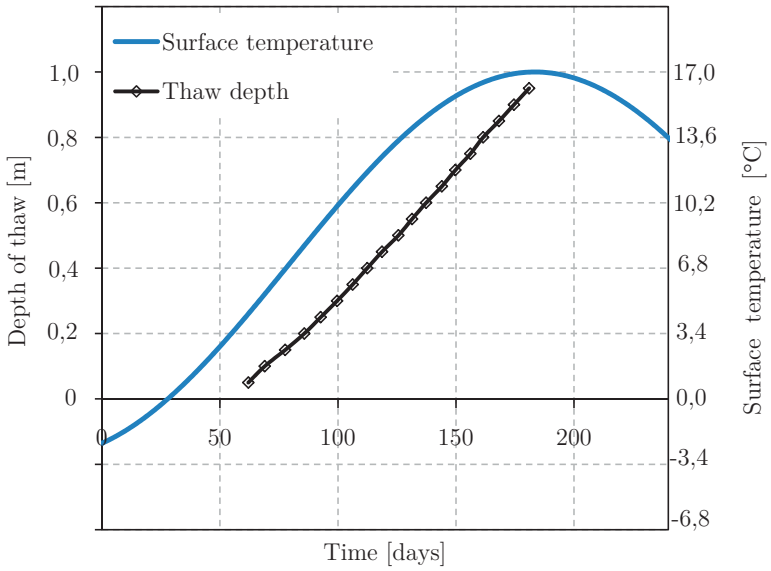

Figure 6.15: Rate of thawing of the frozen subgrade for field conditions.

Figure 6.15 shows the variation of the surface temperature and the rate of thawing in the frozen subgrade layer. In this particular case, it takes about 25 days for the thawing interface to reach the frozen subgrade layer after the surface temperature exceeds the freezing level. As it was discussed in section 6.2.1, the thaw depth is widely understood to be proportional to the square root of time. However, when the multi-layer heat transfer mechanism and varying surface temperature is considered, a linear relationship is obtained between the thaw depth and time. The main practical implications of this finding is that the thawing rate can easily be predicted depending on the available weather data — providing a better understanding of when the thaw starts and ends.

6.5 Chapter summary

The prediction of spring thawing in pavements was the main theme of this chapter. A finite element modelling technique was established and the results were verified using exact analytical solutions. The method is then extended to

model the thawing processes similar to field conditions. In the existing methods of thaw depth calculations, the Stephan's method is commonly used and the thaw depth is assumed to be proportional to the square root of time. This assumption is valid for constant surface temperature. The numerical simulation based on a sinusoidal surface temperature has shown that for the case of frozen subgrade layers in pavements, a constant rate of thawing is obtained.

Chapter 7

Conclusions and recommendations for future work

The characteristics of subgrade soils upon which the pavement structure is placed strongly affect the design and performance of flexible pavements. Subgrade soils have relatively weak strength compared to the upper pavement layers and are most prone to variation of environmental conditions. Despite this fact, the research emphasis has been majorly on the overlying layers, such as the asphalt layer and unbound aggregates. Besides, the accumulated knowledge in this regard is mainly from empirical experience. In recent years, there has been a development of mechanistic-empirical method for pavement design. This method has given the possibility to incorporate material models based on constitutive laws of geo-materials. In order to benefit from the effectiveness of mechanistic models, all pavement layers require constitutive models based on their behaviour for traffic loading and environmental factors.

The main objective of this study was to develop a constitutive model and finite element analysis method that account for the effect of subgrade soils on the overall pavement response. The emphasis of constitutive modelling, in this study, has mainly considered the nonlinear behaviour of resilient modulus and prediction of permanent deformation of fine-grained subgrade soils. Advanced modelling techniques have been also carried out to optimise the short-term and long-term performances of subgrade soils.

7.1 Conclusions on the research method

- The versatility of empirical methods in pavement design is very limited, and they appear appealing only for the materials that the models are derived from. On the other hand, theoretical models remain just a research interest in academia and the practical benefit is mostly limited. The fusion of empirical aspects and theoretical concepts has gained much popularity by the name "mechanistic-empirical" method. Some of the principles of mechanistic-empirical method are hypothetical, but considered to provide a better rational approach than empirical methods. This research aimed to use the key aspects of subgrade soils in mechanistic-empirical design concept, such as the resilient modulus, and the vertical elastic strain on the top of the subgrade layer.
- Apart from the common design methods, advanced finite element modelling techniques have been presented. Full-scale testing of ground conditions in pavements— particularly subgrade soils — is quite demanding. The methods of finite element modelling can be verified based on existing test data and analytical solutions and their application can be extended for different conditions. The improvement of advanced modelling features in finite element methods gives a wide range of possibility in material characterization, controlling boundary conditions, and coupled analysis. This helps us to understand the physical process in roads to provide optimised solutions in the evaluation of design and performance of roads.
- The characterization of subgrade soils is widely described in qualitative basis. In empirical design of roads, a major concern is ensuring the quality of road materials and the description of the extent of material deformation is not known. In this study, the quantitative prediction of the response of the pavement structure for the subsoil conditions is addressed.

7.2 Conclusions on the specific research contributions

7.2.1 Nonlinear resilient modulus of subgrade soils

In this thesis, numerical implementation of nonlinear resilient modulus for subgrade soils is presented. The existing practice in mechanistic-empirical design

methods is based on either the assumption of linear elastic model or simple nonlinear model that accounts only the effect of deviator stress.

- The method presented in this study is more versatile than the existing methods for characterization of fine-grained subgrade soils since it considers the effects of both confining and deviator stresses.
- The critical strain on the top of the subgrade has been compared for the nonlinear elastic and linear elastic methods. The assumption of linear elastic model for the subgrade layer overestimates the allowable number of load repetitions to limit rutting.
- The effect nonlinear behaviour of subgrade soils on the design strain criterion (i.e. vertical elastic strain) was observed to be more significant as the magnitude of the stress increases. In this case, the implications of nonlinear resilient modulus of subgrade soils are important aspects of design of low-traffic volume roads.

7.2.2 Long-term permanent deformation of subgrade soils

A constitutive model for the prediction of permanent deformation of fine-grained subgrade soils is developed. The main hypothesis of the model is based on experimental results available in the literature.

- The constitutive model is defined as a function of the plastic strain from the first loading cycle, and the proximity of the applied stress to static strength of the soil. The Drucker-Prager yield criterion with cohesion-controlled isotropic hardening mechanism is used to obtained deformation from the first load application at which the effects of soil parameters, namely friction angle and cohesion are incorporated.
- The model parameters are obtained from conventional triaxial tests which are commonly carried out in routine geotechnical investigation.
- The predicted results from the proposed model showed a good agreement with laboratory tests for deviator stress level up to 50% of the static strength of the soil. Normally in roads, the mobilization of the soil is always lower than 50% of the static strength of the soil. Hence, the proposed model in this study can be used effectively for the prediction of long-term deformation in subgrade soils.

7.2.3 Effective depth of compaction of fine-grained soils

Most of the optimization of soil compaction in the field has been majorly related to machine performance. In this regard, the new technology (for example Intelligent Compaction methods) enabled us to track on-time compaction performance in the field. Apparently, the optimization technique using the property of the soil has not been widely studied.

- Based on finite element modelling of soil compaction, the lift thickness has been observed to be defined as a function of cohesion and friction angle.
- The economical aspect of soil compaction in road construction is vital. This study suggested the optimisation technique of lift thickness depending on the strength parameters of soils.

7.2.4 Thaw prediction in frozen subgrade soils

The spring thawing is a major concern of pavement deterioration in cold climate regions. In this study, a finite element model is presented to predict the thawing process of frozen subgrade soils in roads.

- The analysis of the one dimensional thawing that has an exact analytical solution is compared with the results obtained from the finite element analysis where a good agreement is obtained.
- To overcome the shortcomings of analytical solutions, a finite element modelling technique is developed to include an actual surface temperature variation and the thermal and physical properties of all pavement layers.
- The existing knowledge of thaw depth for homogenous frozen layer and constant surface temperature is proportional of the square root of time. In this study, the thaw depth is observed to be linearly proportional to time for sinusoidal surface temperature variation and multi-layer coupled heat transfer system.
- Based on the study presented in this thesis, for different climatic regions, a thawing rate index for frozen subgrade soils can be established to optimise road management — particularly in countries that impose axle load restriction during the spring period.

7.3 Recommendations for future work

Characterization of subsoil conditions in pavements is very broad subject to deal with — since there are many factors affecting it. This thesis mainly addresses the aspects of behaviour of subgrade soils in response of the pavement system. The challenges observed in this research are outlined, and suggested future tasks are discussed as follows.

- The analysis of the pavement response using the nonlinear resilient modulus for the subgrade layer in this study is carried out based on the assumption of linear elastic model for the asphalt, base, and sub-base layers. The reason is that the scope of this study is mainly for subgrade soils. A further task is suggested to evaluate the pavement response considering the nonlinear behaviour of all pavement layers.
- The permanent deformation model in this study assumes cohesion hardening mechanism. This assumption is reasonable for cohesive fine-grained soils. However, the hardening mechanism of some soils is controlled by the friction angle. The modelling technique and hypothesis presented in this study can be extended for friction controlled hardening mechanism.
- The optimization of compaction of subgrade soils presented in this thesis is mainly based on numerical analysis. The constitutive model used for the analysis is well validated and commercially available. However, the optimization method suggested in this study requires validation from field studies. This can be an interesting future task.
- The prediction of spring thawing is carried out with the assumption of full saturation conditions. Additionally, it was assumed that all available water becomes ice when the soil is frozen. In reality, some amount of water remains unfrozen which ultimately influences the overall thawing process particularly for fine-grained soils. The finite element program used in this study provides the feature to account for the degree of saturation, but not the amount of unfrozen water. A better prediction model can be established by developing a constitutive model that considers unfrozen water content upon freezing.

7.4 Final remarks

Mechanistic analysis and design methods are nowadays gaining attention in road design in practice. One of the aims of mechanistic design is to account for the properties the subgrade layer as an integral part the pavement analysis — quantitative parameters that describe the behaviour of soils at different conditions are required. In order to advance the application of mechanistic design methods, we need material models capable of predicting the material response similar to field conditions. Finally, and perhaps most importantly, it is vital to ensure that the models are based on constitutive laws of soils so that they will have wide applicability to different types of soils.

References

[1] AASHTO (1993) AASHTO Guide for Design of Pavement Structures. Washington D.C.

[2] AASHTO (2007) Standard Method of Test for Determining the Resilient Modulus of Soils and Aggregate Materials. AASHTO Designation: T 307-99

[3] AASHTO (2011). Available online: http://www.darwinme.org/DARWin-ME/index.aspx [Accessed 6th May 2014].

[4] Aho, S. and T. Saarenketo (2006) Design and Repair of Roads Suffering Spring Thaw Weakening (Executive Summary). Roadex III Project.

[5] Andersland, O.B. and B. Ladanyi (2004) *Frozen Ground Engineering* (2nd ed.): The American Society of Civil Engineers & John Wiley & Sons, Inc.

[6] Andrei, D., M.W. Witczak, C.W. Schwartz, and J. Uzan (2004) Harmonized Resilient Modulus Test Method for Unbound Pavement Materials. *Transportation Research Record: Journal of the Transportation Research Board,* 1874, 29-37. doi: 10.3141/1874-04

[7] ASTM (2007) ASTM Standard D1556: Standard Test Method for Density and Unit Weight of Soil in Place by Sand-Cone Method. West Conshohocken, PA, 2007: ASTM International.

[8] ASTM (2010) ASTM Standard D6938: Standard Test Method for In-Place Density and Water Content of Soil and Soil-Aggregate by Nuclear Methods. West Conshohocken, PA, 2010: ASTM International.

[9] ASTM (2012) ASTM Standard D698: Standard Test Methods for Laboratory Compaction Characteristics of Soil Using Standard Effort. West Conshohocken, PA, 2012: ASTM International.

[10] ASTM (2012) ASTM Standard D1557: Standard Test Methods for Laboratory Compaction Characteristics of Soil Using Modified Effort. West Conshohocken, PA, 2012: ASTM International.

[11] ASTM (2008) ASTM Standard D2167: Standard Test Method for Density and Unit Weight of Soil in Place by the Rubber Balloon Method. West Conshohocken, PA, 2008: ASTM International.

[12] Becker, B.R., A. Misra, and B.A. Fricke (1992) Development of Correlations for Soil Thermal Conductivity. *International Communications in Heat and Mass Transfer,* 19(1), 59-68.

[13] Bonaquist, R. and M.W. Witczak (1996) Plasticity Modeling Applied to the Permanent Deformation Response of Granular Materials in Flexible Pavement Systems. *Transportation Research Record: Journal of the Transportation Research Board,* 1540, 7-14. doi: 10.3141/1540-02

[14] Briaud, J.-L. and J. Seo (2003) Intelligent Compaction: Overview and Research Needs. Texas A&M University.

[15] Brown, S.F., A.F. Lashine, and A.L. Hyde (1975) Repeated load triaxial testing of a silty clay. *Géotechnique,* 25(1), 95-114. doi: 10.1680/geot.1975.25.1.95

[16] Brown, S.F. (1996) Soil Mechanics in Pavement Engineering. *Géotechnique,* 46(3), 383-426. doi: 10.1680/geot.1996.46.3.383

[17] Brown, S.F. (2004) A Hollow Cylinder Apparatus to Study the Cyclic Loading Behaviour of Dry Granular Material. Advances in Geotechnical Engineering , The Skempton Conference. Thomas Telford, London.

[18] Burmister, D.M. (1945) The General Theory of Stresses and Displacements in Layerd Soil Systems. III. *Journal of Applied Physics,* 16(5), 296-302. doi: doi: 10.1063/1.1707590

[19] Burmister, D.M. (1945) The General Theory of Stresses and Displacements in Layerd Soil Systems. II. *Journal of Applied Physics,* 16(3), 126-127. doi: 10.1063/1.1707562

[20] Burmister, D.M. (1945) The General Theory of Stresses and Displacements in Layerd Soil Systems. I. *Journal of Applied Physics,* 16(2), 89-94. doi: 10.1063/1.1707558

[21] Carslaw, H.S. and J.C. Jaeger (1959) *Conduction of Heat in Solids* (2nd ed.): Oxford University Press.

[22] Chai, J.-C. and N. Miura (2002) Traffic-Load-Induced Permanent Deformation of Road on Soft Subsoil. *Journal of Geotechnical and Geoenvironmental Engineering,* 128(11), 907-916. doi: 10.1061/(ASCE)1090-0241(2002)128:11(907)

[23] Chan, F.W.K. (1990) Permanent deformation resistnace of granular layers in pavements. PhD Thesis, University of Nottingham, England.

[24] Chang, G., Q. Xu, J. Rutledge, B. Horan, L. Michael, D. White, and P. Vennapusa (2011) Accelerated Implementation of Intelligent Compaction Technology for Embankment Subgrade Soils, Aggregate Base, and Asphalt Pavement Materials (Final Report). Report No.: FHWA-IF-12-002.

[25] Chen, W.F. and D.J. Han (1988) *Plasticity for Structural Engineers*. New York: Springer-Verlag.

[26] Chiroux, R.C., W.A. Foster(Jr.), C.E. Johnson, S.A. Shoop, and R.L. Raper (2005) Three-dimensional finite element analysis of soil interaction with a rigid wheel. *Applied Mathematics and Computation,* 162(2), 707-722.

[27] Cook, R.D., D.S. Malkus, M.E. Plesha, and R.J. Witt (2002) *Concepts and Applications of Finite Element Analysis* (4th ed.): John Wiley & Sons, Inc.

[28] Daehyeon, K. and S.N. Zia (2006) Simplification of Resilient Modulus Testing for Subgrades, FHWA/IN/JTRP-2005/23. Indiana Department of Transportation.

[29] Dawson, A. and P. Kolisoja (2004) Permanent Deformation. Roadex II Project.

[30] Dawson, A. and P. Kolisoja (2006) Managing Rutting in Low Volume Roads (Executive Summary). Roadex III Project.

[31] de-Souza-Neto, E.A., D. Peric, and D.R.J. Owen (2008) *Computational Methods for Plasticity: Theory and Applications*. Chichester: John Wiley & Sons.

[32] Diaz-Rodriguez (1989) Behavior of Mexico City Clay subjected to undrained repeated loading. *Canadian Geotechnical Journal,* 26(1), 159-162. doi: 10.1139/t89-016

[33] Doré, G. and H.K. Zubeck (2009) *Cold Regions Pavement Engineering*: American Society of Civil Engineers.

[34] Drumm, E.C., Y. Boateng-Poku, and T.J. Pierce (1990) Estimation of Subgrade Resilient Modulus from Standard Tests. *Journal of Geotechnical Engineering,* 116(5), 774-789. doi: 10.1061/(ASCE)0733-9410(1990)116:5(774)

[35] Elliott, R.P., N.D. Dennis, and Y. Qiu (1998) Permanent Deformation of Subgrade Soils(A Test Protocol: MBTC FR-1069). Fayetteville: University of Arkansas.

[36] Elliott, R.P., N. Dennis, and Y. Qiu (1999) Permanent Deformation of Subgrade Soils, Phase II: Repeared Load Testing of Four Soils. National Technical Information Service, Springfiled, VA, Report No.: Report No. MBTC FR-1089 Final Report.

[37] Erlingsson, S. and F. Salour (2013) Thin Flexible Pavement Structures Behaviour during Spring Thaw. Workshop on Pavement Design in Cold Regions, Trondheim, Norway.

[38] Farouki, O.T. (1981) Thermal properties of soils (Monograph 81-1). Hanover, New Hampshire: Cold Regions Research and Engineering Laboratory.

[39] Hambleton, J.P. and A. Drescher (2008) Development of improved test rolling methods for roadway embankment construction. Minnesota Department of Transportation, Report No.: MN/RC 2008-08.

[40] Harichandran, R.S. and G.Y. Baladi (2000) MICHPAVE USER'S MANUAL (Version 1.2). Michigan State University.

[41] Helwany, S. (2007) *Applied Soil Mechancis with ABAQUS Applications*: John Willey & Sons, Inc.

[42] Hicks, R.G., S.B. Seeds, and D.G. Peshkin (2000) Selecting a Preventive Maintenance Treatement for Flexible Pavements. Federal Highway Administration, Washington DC, and Foundation for Pavement Preservation Report No.: FHWA-IF-00-027.

[43] Hight, D.W., A. Gens, and M.J. Symes (1983) The development of new hollow cylinder apparatus for investigating the effects of principal stress rotation in soils. *Géotechnique,* 33(4), 355-383.

[44] Hjelmstad, K. and E. Taciroglu (2000) Analysis and Implementation of Resilient Modulus Models for Granular Solids. *Journal of Engineering Mechanics,* 126(8), 821-830. doi: 10.1061/(ASCE)0733-9399(2000)126:8(821)

[45] Hoff, I. (1999) Material Properties of Unbound Aggregates for Pavement Structures. PhD Thesis, Norwegian University of Science and Technology, Trondheim.

[46] Holtz, R.D. and W.D. Kovacs (1981) *An Introduction to Geotechnical Engineering*: Prentice-Hall,Inc.

[47] Horvli, I. (1979) Dynamisk prøving av leire for dimensionering av veger (in Norwegian) [Dynamic testing of clay subgrades for pavement design]. PhD Thesis, Norwegian Institute of Technology, Trondheim.

[48] Houlsby, G.T. and H.J. Burd (1999) Understanding the behaviour of unpaved roads on soft clay. *12th European Conference on Soil Mechanics and Geotechnical Engineering - Geotechnical Engineering for Transportation Infrastructure*, 7-10 June 1999, Amsterdam. 31-44.

[49] Huang, Y.H. (2004) *Pavement Analysis and Design* (2nd ed.). Upper Saddle River: Pearson Prentice Hall.

[50] Hügel, H.M., S. Henke, and S. Kinzler (2008) High-performance Abaqus simulations in soil mechanics. Abaqus Users' Conference.

[51] Inam, A., T. Ishikawa, and S. Miura (2012) Effect of principal stress axis rotation on cyclic plastic deformation characterstics of unsaturated base course material. *Soils and Foundations,* 52(3), 465-480. doi: 10.1016/j.sandf.2012.05.006

[52] Janoo, V. and K. Shepherd (2000) Seasonal Variation of Moisure and Subsurface Layer Moduli. *Journal of transportation Research Board, Transport Research Record,* 1709, 98-107. doi: 10.3141/1709-12

[53] Janoo, V. and A. Greatorex (2002) Performance of Montana Highway Pavements during Spring Thaw. Federal Highway Administration and Montana Department of Transportation, Report No.: FHWA/MT-02-006/8155.

[54] Jumikis, A.R. (1977) *Thermal Geotechnics*. New Brunswick, New Jersey: Rutgers University Press.

[55] Kavanaugh, P.F. (1984) Engineering and design - Pavement criteria for seasonal frost conditions: Mobilization construction. U.S. Army Corps of Engineers.

[56] Kelm, M. and J. Grabe (2004) Numerical simulation of the compaction of granular soils with vibratory rollers. Cyclic Behaviour of Soils and Liquefaction Phenomena.

[57] Kesler, M.A., G.L. Kanek, and M.A. Truebe (2001) Evaluating Moisture Sensors and Monitoring Seasonal Moisture Variation in Low-Volume Roads. *Journal of transportation Research Board, Transport Research Record,* 1755, 97-107. doi: 10.3141/1755-11

[58] Kim, M., E. Tutumluer, and J. Kwon (2009) Nonlinear Pavement Foundation Modeling for Three-Dimensional Finite-Element Analysis of Flexible Pavements. *International Journal of Geomechanics,* 9(5), 195-208. doi: 10.1061/(ASCE)1532-3641(2009)9:5(195)

[59] Konrad, J.-M. (1999) Frost susceptibility related to soil index properties. *Canadian Geotechnical Journal* 36(3), 403-417. doi: 10.1139/t99-008

[60] Lay, M.G. (1992) *Ways of the World: A History of the World's Roads and of the Vehicles That Used Them*: Rutgers University Press.

[61] Lee, W., N.C. Bohra, A.G. Altschaeffl, and T.D. White (1997) Resilient modulus of cohesive soils. *Journal of Geotechnical and Geoenvironmental Engineering,* 123(2), 131-136. doi: 10.1061/(ASCE)1090-0241(1997)123:2(131)

[62] Lekarp, F. and A. Dawson (1998) Modelling permanent deformation behaviour of unbound granular materials. *Construction and Building Materials,* 12(1), 9-17. doi: 10.1016/S0950-0618(97)00078-0

[63] Lekarp, F., U. Isacsson, and A. Dawson (2000) State of the art. II: Permanent strain response of unbound aggregates. *Journal of Transportation Engineering,* 126(1), 76-83. doi: 10.1061/(ASCE)0733-947X(2000)126:1(76)

[64] Li, D. and E.T. Selig (1994) Resilient Modulus for Fine Grained Soils. *Journal of Geotechnical Engineering,* 120(6), 939-957. doi: 10.1061/(ASCE)0733-9410(1994)120:6(939)

[65] Li, D. and E.T. Selig (1996) Cumulative plastic deformation for fine-grained subgrade soils. *Journal of Geotechnical Engineering,* 122(2), 1006-1013. doi: 10.1061/(ASCE)0733-9410(1996)122:12(1006)

[66] Lytton, R.L. (1987) Concepts of pavement performance. 2nd North American Pavement Management Conference. Available: http://mail.tku.edu.tw/yinghaur/lee/pms/all-handouts/G.pdf,

[67] Manzari, M.T. and R. Prachathananukit (2001) On integration of a cyclic soil plasticity model. *International Journal for Numerical and Analytical Methods in Geomechanics,* 25(6), 525-549. doi: 10.1002/nag.140

[68] Mitchell, R.J. and R.D. King (1976) Cyclic loading of an Ottawa area Champlain Sea clay. *Canadian Geotechnical Journal,* 14(1), 52-63. doi: 10.1139/t77-004

[69] Mohammad, L.N., B. Huang, A.J. Puppala, and A. Allen (1999) Regression Model for Resilient Modulus of Subgrade Soils. *Transportation Research Record: Journal of the Transportation Research Board,* 1687, 47-54. doi: 10.3141/1687-06

[70] Monismith, C.L., N. Ogawa, and C.R. Freeme (1975) Permanent deformation characterstics of subgrade soils due to repeated loading. *Transportation Research Record 537*(1-17).

[71] Morgenstern, N.R. and J.F. Nixon (1971) One-dimensional consolidation of thawing soils. *Canadian Geotechnical Journal,* 8(4), 558-565. doi: 10.1139/t71-057

[72] Muhanna, A.S., M.S. Rahman, and P.C. Lambe (1998) Resilient modulus and permanent strain of subgrade soils. *Transportation Research Record 1619, Transportation Research Board*, 85-93. doi: 10.3141/1619-10

[73] NCHRP (2004) Guide for Mechanistic-Emirical Design of New and Rehabilitated Pavement Structures. Washington D.C.: Report No.: NCHRP 1-37A.

[74] NCHRP (2004) Guide for Mechanistic-Empirical Design of New and Rehabilitated Pavement Structures Final Report (Part 2: Design inputs, Chapter 3: Environmental Effects).

[75] NCHRP (2004) Laboratory Determination of Resilient Modulus for Flexible Pavement Design. National Cooperative Highway Research Program: Research Results Digest Number 285.

[76] NCHRP (2004) Guide for Mechanisstic-Empirical Design of New and Rehabilitated Pavement Structures. Appendix RR: Finite Element Procedures for Flexible Pavement Analysis.

[77] Nixon, J.F. (1973) Thaw-Consolidation of Some Layered Systems. *Canadian Geotechnical Journal,* 10(4), 617-631. doi: 10.1139/t73-057

[78] Nixon, J.F. and E.C. McRoberts (1973) A study of some factors affecting the thawing of frozen soils. *Canadian Geotechnical Journal,* 10(3), 439-452. doi: doi 10.1139/t73-037

[79] Nordal, R.S. and E.K. Hansen (1987) The Vormsund Test Report Part 4: Summary report. Norwegian Road Research Laboratory.

[80] Nordal, S. (2010) Soil Modeling (Lecture Notes for PhD Course). Trondheim: Norwegian University of Science and Technology.

[81] NPRA (1996) Håndbok 193: SKADEKATALOG for bituminøse vegdekker (in Norwegian) [Damage catalogue for bituminous pavements]. Norwegian Public Roads Adminstration.

[82] NPRA (1997) Håndbok 015: Feltundersøkelser (in Norwegian) [Field Investigation]. Norwegian Public Roads Adminstration.

[83] NPRA (2003) Håndbok 111:Standard for drift og vedlikehold(in Norwegian) [Standard for operation and maintenance of roads]. Norwegian Public Roads Adminstration.

[84] NPRA (2011) *Håndbok 018: Vegbygging Normaler (in Norwegian) [Road design and Construction Standards]*: Norwegian Public Roads Adminstration.

[85] Odermatt, N., V. Janoo, and R. Magnusson (1999) Analysis of Pavement Deformation in Subgrade Material Using a Heavy Vehicle Simulator. First International Conference on Accelerated Pavement Testing. 18th Oct - 20th Oct. 1999, Reno,Nev.

[86] Oloo, S.Y., D.G. Fredlund, and J.K.M. Gan (1997) Bearing capacity of unpaved roads. *Canadian Geotechnical Journal,* 34, 398-407. doi: 10.1139/t96-084

[87] PavementInteractive (2006) Frost Action. Available online: http://www.pavementinteractive.org/article/frost-action/ [Accessed 3rd January 2013].

[88] PavementInteractive (2007) Roghness. Available online: http://www.pavementinteractive.org/article/roughness/ [Accessed 11th December 2013].

[89] PavementInteractive (2009) Fatigue Cracking. Available online: http://www.pavementinteractive.org/article/fatigue-cracking/ [Accessed 11th December 2013].

[90] Penner, E. (1970) Thermal Conductivity of Frozen Soils. *Canadian Journal of Earth Science,* 7(3), 982-987.

[91] Penner, E., G.H. Johnston, and L.E. Goodrich (1975) Thermal Conductivity Laboratory Studies of Some Mackenzie Highway Soils. *Canadian Geotechnical Journal,* 12(3), 271-288.

[92] Petersen, D.L. (2005) Continuous Compaction Control MnRoad Demonstration Minnesota Department of Transportation, Report No.: MN/RC-2005-07.

[93] Pietzsch, D. and W. Poppy (1992) Simulation of Soil Compaction with Vibratory Rollers. *Journal of Terramechanics,* 29(6), 585-597.

[94] Proctor, R.R. (1933) Fundamental principles of soil compaction. *Engineering News-Record,* 111(9), 245-.

[95] Puppala, A.J., L.N. Mohammad, and A. Allen (1996) Engineering Behavior of Lime-Treated Louisiana Subgrade Soil. *Transportation Research Record 1546*, 24-31. doi: 10.3141/1546-03

[96] Puppala, A.J., L.N. Mohammad, and A. Allen (1999) Permanent deformation characterization of subgrade soils from RLT test. *Journal of Materials in Civil Engineering,* 11(4), 274-282.

[97] Puppala, A.J., S. Saride, and S. Chomtid (2009) Experimental and Modeling Studies of Permanent Strains of Subgrade Soils. *Journal of Geotechnical and Geoenvironmental Engineering,* 135(10), 1379-1389. doi: 10.1061/(ASCE)GT.1943-5606.0000163

[98] Rouainia, M. and D.M. Wood (2001) Implicit numerical integration for a kinematic hardening soil plasticity model. *International Journal for Numerical and Analytical Methods in Geomechanics,* 25(15), 1305-1325. doi: 10.1002/nag. 179

[99] Salour, F. and S. Erlingsson (2012) Pavement structural behaviour during spring thaw. Swedish National Road and Transport Research Institute (VTI), Report No.: 2009/0572-29.

[100] Sandström, Å. (1994) Numerical simulation of a vibratory roller on cohesionless soil. Geodynamik Report.

[101] Sayers, M.W. and S.M. Karamihas (1998) The Little Book of Profiling. University of Michigan.

[102] Simo, J.C. and T.J.R. Hughes (1998) *Computational Inelasticity*. New York: Springer-Verlag.

[103] Simonsen, E. and U. Isacsson (1999) Thaw weakening of pavement structures in cold regions. *Cold Regions Science and Technology,* 29(2), 135-151. doi: 10.1016/S0165-232X(99)00020-8

[104] Simulia (2011) Abaqus FEA, Dassault Systèmes. Dassault Systemes.

[105] Taciroglu, E. (1995) Constitutive Modeling of the Resilient Response of Granular Solids. PhD Thesis, University of Illinois at Urbana - Champaign, Urbana, Illinois,

[106] Tayebali, A.A., B.-w. Tsai, and C.L. Monismith (1994) Stiffness of Asphalt-Aggregate Mixes. Strategic Highway Research Program.

[107] Terzaghi, K., R.B. Peck, and G. Mesri (1996) *Soil Mechnanics in Engineering Practice* (3rd ed.): John Wiley & Sons.

[108] Thompson, M.R. and Q.L. Robnett (1979) Resilient properties of subgrade soils. Proceedings of ASCE, 105(TE1) [Online].

[109] Thompson, M.R. (1982) ILLI-PAVE Users Manual. University of Illinois, Urban-Champaign.

[110] Uzan, J. (2004) Permanent Deformation in Flexible Pavements. *Journal of Transportation Engineering,* 130(1), 6-13. doi: 10.1061/(ASCE)0733-947X(2004)130:1(6)

[111] Vejdirektoratet (2011) MMOPP Dimensioneringsprogram for Vejbefæstelser - Brugervejledning. The Danish Road Directorate.

[112] ViaTech ViaTech: Maintenance systems for road, rail and airport. Available online: http://www.viatech.no/ [Accessed 11th December 2013].

[113] Vägverket (2011) PMS Objekt version: 4.2.0.

[114] Williams, P.J. and M.W. Smith (1989) *The Frozen Earth: Fundamentals of Geocryology*. Cambridge: Cambridge University Press.

[115] Xia, K., A. Masud, and Z. You (2008) A large deformation finite element formulation for subgrade soil compaction. *Pavements and Materials*, 122-130.

[116] Xu, J., B. Abdalla, A. Eltaher, and P. Jukes (2009) Permafrost Thawing - Pipeline Interaction Advanced Finite Element Model. *Proceedings of the ASME 2009 28th International Conference on Ocean, Offshore and Arctic Engineering, OMAE2009*, Honolulu, Hawaii, USA.

[117] Yang, S.-R., H.-D. Lin, J.H.S. Kung, and W.-H. Huang (2008) Suction-controlled laboratory test on resilient modulus of unsaturated compacted subgrade soils. *Journal of Geotechnical and Geoenvironmental Engineering,* 134(9), 1375-1384. doi: 10.1061/(ASCE)1090-0241(2008)134:9(1375)

[118] Yesuf, G.Y., I. Hoff, and J. Vaslestad (2013) Optimization of Effective Depth of Compaction for Fine-Grained Soils. *Third International*

Conference on Geotechnique, Construction Materials and Environment, November 13-15, 2013, Nagoya, Japan. 333-338.

[119] Yesuf, G.Y., I. Hoff, and J. Vaslestad (2013) Development of excess pore-water pressure in thawing process of frozen subgrade soils : Based on analytical solutions and finite element method. *18th International Conference on Soil Mechanics and Geotechnical Engineering*, September 2-6, 2013, Paris, France. 857-860.

[120] Yesuf, G.Y. (2014) Implications of Nonlinear Behaviour of Subgrade Soils in Flexible Pavement Design. *International Journal of Pavement Engineering*, (Submitted).

[121] Yesuf, G.Y. and I. Hoff (2014) Finite Element Modeling for the Prediction of Permanent Deformation of Subgrade Soils *Road Materials and Pavement Design*, (under peer review).

[122] Ying, G., Z. Chengcheng, L. Hongjun, and S. Wei (2011) The Impact of Water Content and Compaction of The Soil on The Slope Protection by Vegetation. Third International Conference on Transportation Engineering. July 23-25, 2011, Chengdu, China.

Appendix A

The Fourier series may be used to represent periodic functions as a linear combination of sine and cosine functions. If $f(t)$ is a periodic function of period T, then under certain conditions its Fourier series is given in Equation [A.1] as shown below. A concise Matlab function is developed to determine the numerical values the Fourier coefficients for any periodical functions.

$$F(t) = \frac{a_0}{2} + \sum_{n=1}^{\infty} a_n \cos\frac{2n\pi t}{T} + \sum_{n=1}^{\infty} b_n \sin\frac{2n\pi t}{T} \qquad [A.1]$$

Where $n = 1,2,3\cdots$; T is the period of the function; and a_n and b_n are the Fourier coefficients obtained from Equations [A.2]–[A.4].

$$a_0 = \int_0^T F(t)dt \qquad [A.2]$$

$$a_n = \frac{2}{T}\int_0^T F(t)\cos\left(\frac{2n\pi t}{T}\right)dt \qquad [A.3]$$

$$b_n = \frac{2}{T}\int_0^T F(t)\sin\left(\frac{2n\pi t}{T}\right)dt \qquad [A.4]$$

The Matlab program is shown as follows.

```
%%%%%%%%%%%%%%%%%%%%%%%%%%%%%%%%%%%%%%%%%%%%%%%%%%%%%%%%%%%%%%%%
clear all, close all,  clc
%************************************************************
%** The following code calculates the Fourier coefficients **
%** for any functions that follow a periodic pattern.      **
%************************************************************

syms x;          % x is the variable for numerical integration
n =4;            % Number of coefficients to calculate
                 % n can be modified by the user
a = 10.;         % a, b, c, and d are coefficients for the curve
w_n = 0.00001;   %       to fit the curve or the discrete data.
b = 9.8;
c = 7.;
phi = 4*atan(1.0) % phi is a numerical value of pi with
                  %     high precision
y = a*(cos(w_n*x*phi/180. + b ))+c;  % where w_n = 2*pi*f
                  % T = 2*pi/w_n (seconds)
                  % w_n is the angular frequency(rad/s)
                  % f is the ordinary frequency (Hz)
T = 360. /w_n

%************************************************************
%** COMPUTE THE FOURIER COEFFICIENTS                       **
%**                  k=infinity                            **
%** F(x)=(a_0/2)+SUM[(a_i*cos(k*pi*x)/T)+(b_i*cos(k*pi*x)/T)]
%**                  k=1                                   **
%** Now determine  a_0, a_i, b_i  for  i > 0               **
%**  a_0 = (1/T)*Integral(F(x), x, 0, T)                   **
%**  a_i = (2/T)*Integral(F(x)*cos((2*pi*k*x)/0.5T),x,0,T)**
%**  b_i = (2/T)*Integral(F(x)*sin((2*pi*k*x)/0.5T),x,0,T)**
%************************************************************

% Start computing the Fourier coefficients in Matlab

a_0 = (2/T)*int(y, x, 0, T); %
a_coeff = [];                % Declaring an array
b_coeff = [];                % Declaring an array
fprintf('Fourier Coef:\ta_0 ==> %0.10f\n',double(a_0))

for k = 1 : n
    a_coeff = [a_coeff, (2/T)*int(y*cos(2*k*pi*x/T),x,0,T)];
    b_coeff = [b_coeff, (2/T)*int(y*sin(2*k*pi*x/T),x,0,T)];
    fprintf('Fourier Coef:\t');
    fprintf('a_%1.0f ==> %0.30f\t\t', k, double(a_coeff(k)));
    fprintf('b_%1.0f ==> %0.30f\n', k, double(b_coeff(k)));
end
% End computing the Fourier coefficients in Matlab
%
% Fourier terms
F_x = [];
First_term = a_0/2;
x_range = 0:1000000:60000000;  % Range of values for x
for i = 1 : length(x_range)
    a_sum = 0;
    b_sum = 0;
    for k = 1 : n
```

```
        a_sum = a_sum + a_coeff(k)*cos(2*phi*k*x_range(i)/T);
        b_sum = b_sum + b_coeff(k)*sin(2*phi*k*x_range(i)/T);
    end
    F_x = [F_x, First_term + a_sum + b_sum];
end
% PLOT
plot(x_range/(3600*24), F_x, ':bs');
legend('Temprature variation')
xlabel('Time [days]')
ylabel('Temprature [degree Celsius]')
grid on;
% END PLOTS
%************************************************************
%**  The following values are used in ABAQUS because        **
%**  Abaqus FEA has a different designation of the         **
%**  Fourier expression                                     **
%************************************************************
Wn_Abaqus = double(w_n*(phi/180.0))  % Wn is frequency
A_0_ABAQUS = double(0.5*a_0)         % A_0 is initial amplitude
%%%%%%%%%%%%%%%%%%%%%%%%%%%%%%%%%%%%%%%%%%%%%%%%%%%%%%%%%%%%%%
```

Appendix B

Published paper 1:

Development of excess pore-water pressure in thawing process of frozen subgrade soils: Based on analytical solutions and finite element method.

Proceedings of the 18th International Conference on Soil Mechanics and Geotechnical Engineering, September 2-6, 2013, Paris, France, Page 857-860.

Development of excess pore-water pressure in thawing process of frozen subgrade soils: Based on analytical solutions and finite element method.

Dégel des sols et variation de la pression d'eau interstitielle: application de méthodes analytiques et des éléments finis.

G.Y.Yesuf & I. Hoff
Norwegian University of Science and Technology, Trondheim, Norway

J. Vaslestad
Norwegian Public Roads Administration, Oslo, Norway

ABSTRACT: The spring thaw of a frozen soil is controlled by boundary conditions and soil thermal properties. Frozen soils have substantially reduced permeability and the melting water in the thaw front cannot drain through the still-frozen soil. Consequently, temporary excess pore-pressure is generated in the process which degrades the shear strength of the soil. This will ultimately reduce the bearing capacity in roads. In this paper, analytical solutions and a finite element method are used to estimate the thawing rate of frozen soils, in which a very good agreement is obtained for one-dimensional thawing. Axisymmertic geometry was used in Abaqus FEA to model the pavement layers with a sinusoidal surface temperature. From the numerical simulation, it was obtained that a constant rate of thawing can be assumed for frozen subgrade layers for one directional top-bottom thawing. The excess pore-water pressure largely depends on the initial ground temperature as well as on the magnitude of surface temperature.

RÉSUMÉ : Le mécanisme de dégel des sols est déterminé par les conditions limites et les propriétés thermiques des matériaux. Les sols gelés ont une perméabilité sensiblement réduite. De plus, lors du dégel, l'eau ne se draine pas toujours au même rythme que la fonte. Une fonte rapide entraine un excès de pression interstitielle, ce qui diminue la résistance au cisaillement et entraîne une diminution considérable de la portance des sols et des chaussées. Ce papier présente les résultats de l'estimation du taux de dégel des sols par des méthodes de résolution analytique et des éléments finis. Une très bonne corrélation est obtenue dans le cas de la simulation du dégel en une dimension. Les couches de chaussées ont été modélisées dans Abaqus FEA par géométrie asymétrique, en appliquant une courbe de température de surface sinusoïdale. Une simulation numérique a permis d'établir l'hypothèse d'un dégel unidirectionnel depuis la surface, à taux constant. L'excès de pression interstitielle dépend grandement de la température initiale du sol et de la température de surface.

KEYWORDS: FEM, pore-water pressure, temperature, thawing, thawing rate

1 INTRODUCTION

Climate condition is one of the factors that affect design and performance of pavements. Epecially in cold regions, seasonal freezing and thawing process may occur in subgrade soils. The extent of damage on the pavement surface due to freezing and subsequent thawing of subgrade soils depends on many factors such as the thermal gradient, availability of water in the sub-soil layers, frost susceptibility of the soil, consolidation coefficient, permeability and drainage conditions. If the rate of generation of water exceeds the discharge capacity of the soil, excess pore pressure will develop, which can lead to failure of foundations and slopes (Morgenstern and Nixon 1971). A pavement structure will be most susceptible to breakup during the period when excess water cannot drain downward through still-frozen soil. A major practical aspect of predicting the thawing mechanism can be for effective road management (especially for countries that imposed load restriction during spring thawing) and maintenance programs. When the bound layer of a road is thinner, the anticipated traffic load in the subgrade is high. Consequently, the excess pore-water pressure(in the short term) during thawing increases, partly due to the phase change from the ice state, and partly due to the additional load from the traffic. The cumulative effect can be severe and this has been true in many cases especially for low-traffic volume roads since maintenance budgets are relatively low and appropriate drainage is missing. Full scale tests conducted at the Vormsund test road (Nordal and Hansen 1987) showed that the excess pore-water pressure developed during the spring thaw was the primary reason for the reduced bearing capacity. Pore-water pressures of up to 0.90m above the drainage level was registered during thawing.

The problem of spring thawing has no exact solution. Analytical solutions for heat conduction are well known and are obtained from the Newmann's solution (Carslaw and Jaeger 1959). Nixon(1973) formulated an approximated analytical solution from the theory of consolidation and principle of heat conduction for the development of excess pore-water pressure following the thawing process. This analytical solution is valid for thawing of soils over thick ice layers. The impact of seasonal frost penetration on pavement has been widely studied, with considerably less focus on thaw weakening from thawing (Simonsen and Isacsson 1999).This paper discusses on the rate of thawing (thaw advancement) in the frozen soil layers in pavements and the subsequent excess pore-water pressure. The study is based on the existing analytical solutions and finite element method (FEM). The general FEM program, Abaqus FEA has been used to model the thawing process. The thawing process is widely understood qualitatively. For example, the types of subgrade soils that are frost susceptible are well known (Johnson et al. 1986; NPRA 2011) and some empirical correlations exist relating the depth of frost penetration to the Freezing Index (Andersland and Ladanyi 2004). The study presented here focuses on the quantitative explanation of the thawing process based on the thermal properties of pavement materials and thermal boundary conditions. With a better understanding of the thawing process, optimization process can be carried out during the design phase, operation and maintenance of roads.

1.1 Thermal properties of soils

The principle of heat transfer in frozen soils is governed by conduction. The effect of radiation is negligible. The heat transfer process by convection is also minimal for fine-grained soils with very low permeability. During freezing, some of the water film is removed and ice crystals partially fill the voids between soil particles. This reduces the conductivity path for soil with low moisture content. In the contrary, experimental tests at high moisture content and densities showed increased conductivities in the frozen state, since ice fills the pores completely (Becker et al. 1992, Penner et al. 1975). The thermal conductivity of ice is more than four times greater than that of water (Penner 1970). In the thawing process of frozen soils, the amount of water in the frozen state plays a significant role in the development of pore-water pressure. Some assumptions are made in the analyses in this paper such as the frozen soil is fully saturated, the heat transfer mechanism is only by conduction, and the thermal conductivity of the soil is isotropic.

2 ANALYTICAL AND NUMERICAL SOLUTIONS FOR THE THAWING PROCESS

Nixon and McRoberts (1973) studied on the thawing rate of homogeneous frozen soil subjected to a step increase in temperature from (T_g) in the ground to (T_s) at the surface. The analythical formulla relating the depth of thawing to the square root of time, based on Newmann's solution (Carslaw and Jaeger 1959) is shown in Eq. 1.

$$X = \alpha\sqrt{t} \tag{1}$$

Where X is the depth of thaw, t is the time and $\propto$ is a constant determined from Newman's rigorous equation. When the ground temperature is close to zero, the equation from Newmann is simplified as (Nixon and McRoberts 1973);

$$\frac{e^{-\frac{\alpha^2}{4\kappa_u}}}{\operatorname{erf}\left(\frac{\alpha}{2\sqrt{\kappa_u}}\right)} = \frac{L\sqrt{\pi}\alpha}{2\sqrt{\kappa_u}c_u T_s} \tag{2}$$

Where

α is the constant in Eq. 1.
κ_u is the diffusivity of the unfrozen soil (m^2/s).
K_u is thermal conductivity of the unfrozen soil ($J / ℃ \cdot m \cdot s$).
c_u is the volumetric heat capacity of the unfrozen soil ($J/℃ \cdot m^3$).
L is the volumetric latent heat of the soil(J/m^3).
T_s is the applied constant surface temperature (℃).
erf is the error function.

2.1 Finite element analysis

In the thawing process, temperature has a direct effect on the water flow field in saturated and unsaturated soils which undergo drainage and consolidation upon thawing. As a result of this, the heat flow and fluid flow equations are coupled mathematically through the phase change component and an optimization procedure is incorporated into the computational scheme (Harlen 1973). In a saturated soil, the latent heat absorbed/released on the thaw-freeze front has a major impact on the rate of thawing. In the numerical scheme, the latent heat can be defined in two ways (Xu et al., 2009). It can be included in the heat conduction equations or it can be defined by using temperature dependent specific heat as shown in Figure (1). To ensure the accuracy of this method, the time increments or the maximum temperature change in each increment should be limited to assure the energy balance and a uniform temperature field is defined as initial condition. In this analysis, the latent heat is assumed to be released between -0.1℃ and 0℃. Thermal properties of the soil, listed in Table (1) are used both for the analytical analysis and numerical simulation. For the numerical input, temperature dependent thermal properties are used for the frozen and thawed states. A frozen soil is almost impermeable and a very low permeability, $k = 1 \times 10^{-14}$ m/s, is used for the ground temperature less than zero degree Celsius.

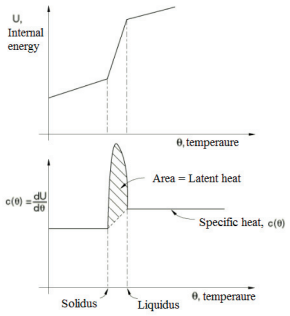

Figure 1. Specific heat, latent heat definition (Abaqus FEA, 2011).

Table 1. Input parameters.

Parameters	Unit	Value
Thaw conductivity	$J/m \cdot s \cdot ℃$	1.05
Consolidation coefficient(c_v)	m^2/s	1.1 x 10^{-6}
Permeability(k)	m/s	2.5 x 10^{-7}
Unit weight(γ)	kg/m^3	1820
Latent heat of soil(volumetric)	J/m^3	1.73 x 10^8
Latent heat of water	J/kg	3.34 x 10^5
Surface temperature	℃	12
Ground temperature	℃	0

The conductivity of the frozen soil is assumed to be twice that of the thawed soil. Similarly, the stiffness of the frozen soil is assumed to be 100 times that of the stiffness in the thawed state. The amount of frozen water is directly related to the moisture content. For fully saturated soils, a reasonable assumption of void ratio can be made from the following relationship.

$$e = \frac{w * G_S}{S} \tag{3}$$

Where e is the void ratio, w is the water content, G_s is the specific gravity of the soil, and S is the degree of saturation ($S = 1$ for fully saturated condition). In reality, the void ratio of soils varies greatly upon freezing and thawing. The permeability of the soil can be defined as a function of void ratio in the numerical simulation.

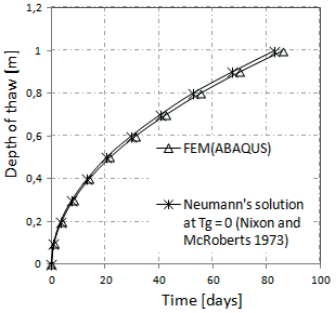

Figure 2. Comparison of analytical solution and numerical simulation.

The stiffness of the thawed soil in the numerical analysis is determined from Poisson's ratio and the modulus which is related to the coefficient of consolidation (Janbu 1970, Berntsen 1993). Some variables for "predefined fields" in Abaqus are defined. The initial pore-water pressure is set to zero. The initial temperature of the frozen soil (ground temperature) in assumed to be zero to compare the results with the simplified Neumann's solution in Eq. 2.The soil is also considered to be fully saturated prior to thawing. Detailed procedures for defining "predefined fields", "initial conditions", and thermal boundary conditions are available in the Abaqus FEA. The analytical solution from (Eq. 2) has been compared with the result obtained from a numerical analysis using axisymmetric geometry and coupled temperature-pore pressure elements in Abaqus. The thawing depth from the numerical simulation is obtained by plotting the time at which the temperature is changed from negative to positive(℃) at selected nodes in the frozen soil layer. A very good agreement is obtained from the analytical solution and numerical simulation (see Figure 2).

2.2 *Excess pore-water pressure*

One of the consequences of spring thawing is that the frozen water is melted upon thawing. Consequently, excess pore-water is generated depending on the overburden stress from the pavement layers and external loading from the traffic. In the case where a thick ice layer exists, an excess pore-water pressure can develop even from self-weight loading of the soil lying on the ice layer. This phenomenon was modeled analytically by Nixon(1973). The analysis is based on the principle of heat conduction and Terzaghi's one-dimensional consolidation theory. From the coupled numerical analysis (using Abaqus), it is possible to obtained excess-pore-water pressure. The amount of excess pore-water pressure is very sensitive the volumetric thermal expansion of pore-water in the voids of the frozen soil and the stiffness of the frozen soil. So, a direct consideration of the output from the numerical analysis may be misleading. Since we can accurately predict the advancement of thawing by using the numerical analysis, we can relate the development of excess pore-water to the thawing rate. A hydrostatic pore-water pressure can be assumed for a thawed soil if no additional loading exists. For example, for a frozen subgrade soil under a pavement, the excess pore-water pressure will be the total overburden pressure (asphalt, base and sub-base layers) including the loading from the traffic. This assumption is valid for undrained conditions. In many cases, subbase materials (aggregates) facilitate the dissipation of excess pore-water pressure. Then, post-thaw consolidation follows. Detail analysis of one-dimensional thaw consolidation is presented in Morgenstern and Nixon(1971).

2.3 *Modelling of thawing subgrades in pavements*

Most of the analytical solutions available in the literature for the thawing process are based on a one step temperature increment on the surface. In reality, the change of surface temperature is neither a step change nor constant. It is closer to a sinusoidal curve. An advantage is gained by using numerical analysis for different boundary conditions and pavement layers. An axisymmetric geometry is modeled in Abaqus as shown in Figure 3. This model (geometrically) is a reasonable approximation for isotropic behavior of pavement materials and an efficient computation time is obtained for the numerical thermal analysis. The assumed thermal properties of the asphalt materials and base course are listed in Table 2. The frozen subgrade is modeled in the same way described in section 2.1. A sinusoidal surface temperature is considered based on a local weather data in Norway (Figure 4). The sinusoidal equation for the temperature data is established. A Fourier transformation is used to obtain the Fourier coefficients which are used as input in Abaqus to provide a smooth increment of temperature for each time increment.

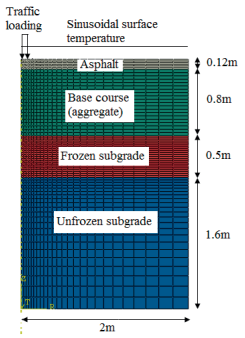

Figure 3. Geometry of the model (axisymmetric).

Table 2. Thermal properties of the asphalt and base layers.

Parameters	Unit	Value	
		Asphalt	Base-course
Conductivity	J/m.s.^{0}C	0.75	0.5
Specific heat	J/kg.^{0}C	920	850
Coefficient of expansion	/^{0}C	2.2 x 10^{-5}	3 x 10^{-6}

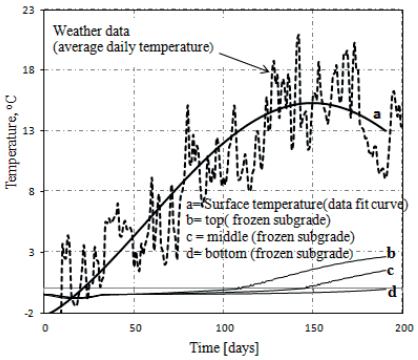

Figure 4. Temperature variation during spring thawing.

Assuming a uniform initial ground temperature Tg=-2^{0}C the temperature distribution in the frozen subgrade due to the change of surface temperature on the pavement surface is shown in Figure 4. It is noted that it takes about 90 days for the frozen layer to start thawing from the time since the surface temperature has been greater than 0℃. Full scale field tests (Nordal and Hansen 1987) showed a time period of 70 days for the temperature measurement at 1.93m below the pavement surface for the subgrade soil temperature to be changed from negative to positive temperature(in degree Celcius). Nordal and Hansen measured the temperature variations at at depth of 0.05m, 0.15m, 0.63m, 0.93m and 1.93m. The measurements showed that the surface temperature is higher than the data used in our numerical analysis. In accounting this fact, the approximation obtained from the numerical analysis can be accounted for practical case studies.

The analytical solutions for temperature distributions (for example Stephan's formula) relate the thawing depth to be

proportional to the square root of time of thawing. Based on the results from the FEM analysis, when sinusoidal surface temperature and thermal properties of pavement layers such as asphalt and base layers are considered, the thawing depth can be directly proportional to the rate time (see Figure 5).

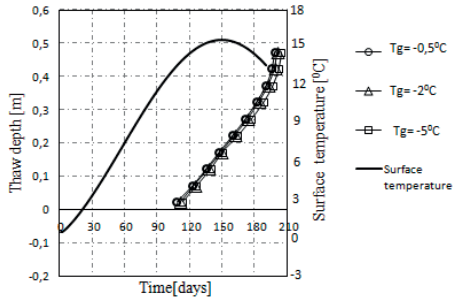

Figure 5. Thawing rate in frozen subgrade under a pavement.

An average of 90 days is required for the frozen layer to start thawing for the given thermal properties and boundary conditions assumed in this analysis. No significant difference is observed for the variation of the initial ground temperature on the thaw rate. Constant rate of thawing in subgrade soils (in terms of mm/day) has been observed in different field tests reported in Doré (2004).

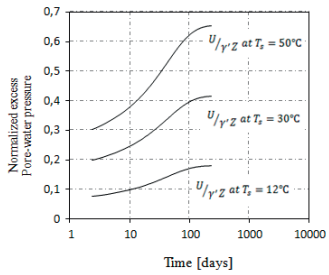

Figure 6. Excess pore pressure at soil-ice interface for a constant surface temperature. The curves are based on the analytical solution of Nixon(1973).

It can be observed (in Figure 6) from analytical solution of Nixon(1973) that the time required for the development of maximum excess pore-water pressure at the soil-ice interface (thawing period) is the same regardless of the temperature gradient . In the contrary, the maximum excess pore-water pressure generated when the surface temperature is 30°C, is twice the maximum excess pore pressure generated at a constant surface temperature of 10°C. This comparison is only for self-weight loading of the soil and the expected excess pore-water pressure can be very high depending on the overburden pressure from the pavements and traffic loading.

3 CONCLUSION

In the previous analytical methods of thaw depth calculations, the Stephan's method is commonly used and the thaw depth is assumed to be proportional to the square root of the thawing time. This assumption is valid for constant surface temperature. The numerical simulation based on a sinusoidal surface temperature has shown that for the case of frozen layers in pavements, a constant rate of thawing is obtained. A higher thawing rate in less permeable frozen soils results in high excess pore-water pressure. The late spring thawing can be predicted from the change in pavement temperature from available climatic data, and thermal and physical properties of the pavement materials. This has a significant importance in road design and maintenance planning in cold climate regions. The development of excess pore-water pressure highly depends on the temperature distribution in the pavement layers and traffic load and initial states. The excess pore-water pressure development is also largely dependent on the physical properties of the thawed soil such as the coefficient of consolidation and permeability.

4 *ACKNOWLEDGEMENTS*

The research is carried out at the Norwegian University of Science and Technology (NTNU) with the financial support from the Norwegian Public Roads Administration.

REFERENCES

Abaqus FEA, D S Simulia. 2011 Dassault Systèmes.

Andersland, O.B. and Ladanyi, B. 2004. Frozen Ground Engineering. 2nd ed. The American Society of Civil Engineers and John Wiley & Sons, Inc.

Becker, B.R., Misra, A. and Fricke, B.A. 1992. Development of Correlations for Soil Thermal Conductivity. *International Communications in Heat and Mass Transfer*, 19(1), 59-68.

Carslaw, H.S. and J.C. Jaeger 1959. Conduction of Heat in Solids. 2nd ed. Oxford University Press.

Berntsen, G. 1993. Reduction of bearing capacity during thawing(in Norwegian), Norwegian Institute of Technology: Trondheim, Norway.

Doré, G. 2004. Development and validation of the thaw-weakening index. *International Journal of Pavement Engineering*,. **5**(4), 185-192.

Harlan, R.L. 1973. Analysis of Coupled Heat - Fluid Transport in Partially Frozen Soil. Water Resources Research, **9**(5), 1314-1323.

Janbu, N. 1970. Grunnlag i geoteknikk(in Norwegian)., Trondheim: Tapir Forlag.

Johnson, T.C., R.L. Berg, E.J. Chamberlain,D.M. Cole. 1986. Frost Action Predictive Techniques for Roads and Airfields: A Comprehensive Survey of Research Findings. *Cold Regions Research and Engineering Laboratory CRREL report 86-18.*

Morgenstern, N.R. and Nixon, J.F. 1971. One-dimensional consolidation of thawing soils. *Canadian Geotechnical Journal*, 8(4), 558-565.

Nixon, J.F. 1973. Thaw-Consolidation of Some Layered Systems. *Canadian Geotechnical Journal*, 10(4), 617-631.

Nixon, J.F. and McRoberts, E.C. 1973. A study of some factors affecting the thawing of frozen soils. *Canadian Geotechnical Journal*, 10(3), 439-452.

NPRA. 2011. Håndbok 018: Road construction standards (in Norwegian). Norwegian Public Roads Adminstration.

Nordal, R.S. and Hansen, E.K. 1987. The Vormsund Test Road, Part 4: Summary report, Norwegian Road Research Laboratory.

Penner, E. 1970. Thermal Conductivity of Frozen Soils. *Canadian Journal of Earth Science*, 7(3), 982-987.

Penner, E., Johnston, G.H. and Goodrich, L.E. 1975. Thermal Conductivity Laboratory Studies of Some Mackenzie Highway Soils. *Canadian Geotechnical Journal*, 12(3), 271-288.

Simonsen, E. and Isacsson, U. 1999. Thaw weakening of pavement structures in cold regions. *Cold Regions Science and Technology*, 29(2), 135-151.

Xu, J., Abdella, B., Eltaher, A., and Jukes, P. 2009. Permafrost Thawing - Pipeline Interaction Advanced Finite Element Model. in *Proceedings of the ASME 2009 28th International Conference on Ocean, Offshore and Arctic Engineerin*g, OMAE2009. Honolulu, Hawaii, USA, 1-6.

Published paper 2:

Optimization of effective depth of compaction for fine-grained soils

Proceedings of the 3rd International Conference – GEOMATE 2013 Geotechnique, Construction materials and Environment, November 13-15 2013, Nagoya, Japan, Page 333-338.

Third International Conference on Geotechnique, Construction Materials and Environment, Nagoya, Japan, Nov. 13-15, 2013, ISBN: 978-4-9905958-2-1 C3051

OPTIMIZATION OF EFFECTIVE DEPTH OF COMPACTION FOR FINE-GRAINED SOILS

Girum Y. Yesuf[1], Inge Hoff[2] and Jan Vaslestad[3]
[1,2]Faculty of Engineering Science and Technology, Norwegian University of Science and Technology, Norway; [3] Norwegian Public Roads Administration, Norway

ABSTRACT

Soil compaction is an important phase during construction of roads. Its primary aim is to reduce the void ratio, in order to improve the strength of the soil. In this way, a good bearing capacity of pavement foundation is obtained. Consequently, long term deformation in the pavement layers can be substantially reduced. In this paper, a finite element method is used to study the rolling compaction of fine-grained soils. Since compaction is associated with volumetric plastic deformations, the modified Drucker-Prager Cap model, available in Abaqus FEA is used for numerical simulation. The soil-structure interaction of a rolling rigid body over a compressible soil mass is defined using Abaqus/Explicit. The weight of the roller, or the contact pressure, is directly related to the effective compaction depth and density of the soil. The evaluation of these factors has been optimized using the strength characteristics of soils, namely the cohesion and friction angle.

Keywords: Cap model, Compaction, Density, Optimization

INTRODUCTION

Pavement layers are compacted during road construction to maintain the long-term performance of roads. Insufficient compaction leads to distress in pavements such as premature pavement rutting, longitudinal unevenness and cracking. Hence, compaction of bound and unbound materials in roads is highly desired. The increase of vehicles with heavier axle loads demands a good subgrade support. A good bearing capacity of subgrade soils is often obtained by increasing the strength by means of compaction. Compaction increases also the stiffness of the pavement layers so that future settlements due to the traffic loads can be greatly reduced. To a lesser extent, the reduced permeability of soils may prevent undesirable frost heave problems. The common factors that control the extent of compaction are the compaction effort, the type of soil and its gradation, and the water content [1].

In the study presented in this paper, we mainly discuss on the effect of the compaction energy and the strength characteristics of soils for possible optimization techniques by using a Finite Element Method (FEM). The scope of modeling is limited to static roller compaction which is often applied to the fine-grained soils. Since the compaction process is highly dependent on the moisture content, the numerical modeling is more suitable for studying the soil-roller interaction. Moreover, the influence of moisture content in subgrade soils can be related to geotechnical soil parameters such as cohesion and friction angle. These parameters are not the inherent properties of soil; rather they describe the "condition" of the soil. For soils, the highest strength is frequently obtained by using greater compactive efforts with water contents somewhat below the optimum moisture content. Large scale tests [2] have shown that the confined compressive strength of clayey sand could be doubled by compaction, within the range of practical field compaction procedures.

Rollers with static load drums use the effective dead weight of the machine to apply pressure on the surface. Adequate compaction with static rollers is normally achieved only in the upper layers of the material because the effective depth of static compaction is limited [3]. In some cases, considerable compaction can also be obtained by proper routing of hauling equipment during construction [2]. Although the specifications of these compacting machines are different, the degree of compaction is highly dependent on the static weight of the roller. Road agencies provide regulations on the static load that must be used during compaction and the number of roller passes [4]. In this way, the quality of compaction is ensured or field tests are conducted to evaluate the degree of compaction.

With the advent of high computer speed and availability of advanced finite element modeling tools, the science of terra-mechanics is gaining popularity in the recent years for optimization of soil-structure problems [5]-[7]. Besides, appropriate soil models should be chosen for the specific practical problems. In this paper, the

theoretical formulations of the model used in our analysis is presented from literature [8],[9]. In the conventional elastoplastic soil models, such as the standard Drucker-Prager and Mohr-Coulomb models, the application of compressive hydrostatic pressure alone does not cause plastic flow. Plastic flow under compressive hydrostatic pressure may only be triggered with the superposition of shear stresses. When plastic compaction is relevant the standard Drucker-Prager or Mohr-Coulomb plasticity models are not able to capture the actual material behavior [10]. Instead, the Drucker-Prager Cap model is used for soil compaction.

The analysis presented in this paper is based on the assumption of monotonic loading conditions of static rollers during soil compaction. If the dynamic effect of the roller(i.e. rolling speed, vibration frequency) is to be evaluated, advanced rate-dependent models such as the hypoplastic model formulation must be considered for realistic simulation of the compaction process [11],[12]. Another important aspect of numerical simulation of soil compaction is the geometric and boundary modeling techniques. Such issues are addressed in this paper mainly based on the user manual of the FEM tool used for the numerical simulation [8].

FEM MODELLING

Finite element analysis has been widely used for modeling non-linear soil-structure interaction problems in recent years. The numerical simulation of soil-structure interaction needs the contact boundary conditions to be properly defined. In this study, the finite element program Abaqus FEA has been used for modeling of the roller compaction. The numerical simulations presented in this paper are carried out using Abaqus/Explicit. The explicit scheme provides stable solutions for contact problems, in contrast to the implicit scheme. In the longitudinal direction (direction of rolling), small elements are used to ensure a smooth interaction between the roller surface and the soil.

The objective of the FEM, in this study, is to obtain a relationship between the weight of the roller and the volumetric plastic strains (change in density). It is assumed that the change in density is due to the plastic deformations which do not reach a large deformation limit. The principle is more suitable for surface compaction of wet fine-grained soils in thin layer applications. When large deformation is encountered during compaction, objective stress rates must be considered in the numerical scheme [8]. This is not the scope of this paper.

The three-dimensional model that is used in this study is shown in Fig. 1. It consists of two distinct bodies: a soil bed and a rigid rotating roller.

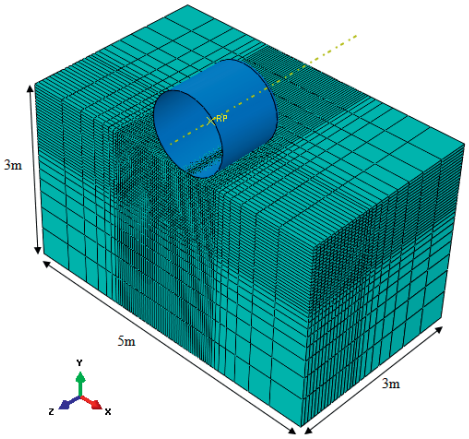

Fig. 1 Geometric model of the soil and roller.

Because of symmetry, only one-half of the geometry is modeled. To ensure the dynamic analysis with a very small inertial effect, a small mass (i.e. 100kg) is assigned for the roller. A point load, equivalent to the weight of the roller) is applied at the center of mass at the reference point. In the numerical model, the motion of the rigid body is controlled by the boundary and loading conditions applied at the reference point.

The Soil Model

The soil is modeled using the modified Drucker-Prager Cap model incorporated in Abaqus FEA. The Drucker-Prager constitutive model for pressure sensitive geo-materials was formulated in the 1950ies [9]. Though the original model is able to simulate a varying yield surface depending on the level of the mean stress, it cannot predict plastic volumetric strain or compaction of soil materials during hydrostatic loading. To alleviate this problem, the model was later modified with a convex end cap [13]. The Cap model provides a plastic hardening mechanism to account for plastic compaction and helps to control volume dilatancy when the material yields in shear. The generalized Drucker-Prager yield criterion is shown in Eq. (1) [8].

$$F_s = t - p\tan\beta - d \qquad (1)$$

Where β and d represent the angle of friction and the cohesion of the soil respectively. The deviatoric stress measure $_t$t is defined in Eq. (2).

$$t = \frac{1}{2}q\left[1 + \frac{1}{K} - \left(1 - \frac{1}{K}\right)\left(\frac{r}{q}\right)^3\right] \qquad (2)$$

Where $p = -\frac{1}{3} trace\ \sigma$

$$q = \left(\frac{3}{2} \sigma^{dev} : \sigma^{dev} \right)^{1/2}$$

$$r = \left(\frac{9}{2} \sigma^{dev} : \sigma^{dev} . \sigma^{dev} \right)^{1/3}$$

σ and σ^{dev} are the stress and its deviatoric component. K is the ratio of the yield stress in triaxial tension to the yield stress in triaxial compression. It can be understood from Eq. (2) that the value of K controls the shape of the yield surface.

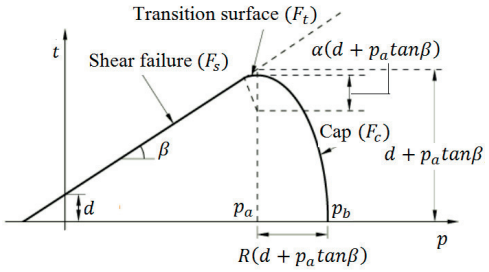

Fig. 2 Density dependent Drucker-Prager Cap model(2D representation) [5].

The cap yield surface includes dependence on the third stress invariant. The cap surface hardens or softens as a function of the volumetric plastic strain. The detail description of the shear failure surface (F_s) and transition surface (F_t) and the Cap surface (F_c) shown in Fig. 2 is available in [8]. The hardening or softening law is a user defined piecewise linear function relating the hydrostatic compression yield stress (p_b)p_b and the corresponding volumetric plastic strain (ε_{vol}^{p}). The current density (ρ)in reference to initial density (ρ_0) can be obtained from the relation with ε_{vol}^{p}, as shown in Eqn. (3) and the cap surface as a function of density is presented in Fig. 3.

$$\varepsilon_{vol}^{p} = ln\left(\rho / \rho_0 \right) \qquad (3)$$

The value of $d, \beta, R, \varepsilon_{vol,0}^{pl}, \alpha$ and K are used to define the shape of the yield surface. The elastic behavior of the soil is defined by its Young's modulus and the Poisson's ratio, and is combined with the Modified Drucker-Prager Cap model to model the overall soil behavior during compaction. For triaxial loading condition, the material cohesion (d) and friction angle (β)are obtained from the Mohr-Coulomb parameters, cohesion (c) and friction angle (ϕ) as shown in Eqs. (4) and (5) for the points where the Drucker-Prager yield surface coincides with the Mohr-Coulomb in triaxial compression.

$$tan\,\beta = \frac{6 * sin\,\phi}{3 - sin\,\phi} \qquad (4)$$

$$d = \frac{6 * c * cos\,\phi}{3 - sin\,\phi} \qquad (5)$$

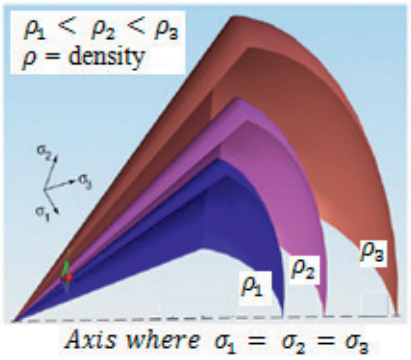

Fig. 3 Density dependent Drucker-Prager Cap model (3D view) [14].

Table 1 Input parameters for the Cap model.

Parameters	Unit	Value
Cap eccentricity parameter, R	[-]	0.2
Initial Cap yield surface position, $\varepsilon_{vol.0}^{pl}$	[-]	0
Transition surface radius parameter, α	[-]	0.01
Flow stress ratio, K	[-]	1.0
Density(initial), ρ_0 ρ_0	[kg / m^3]	1600

The Cap hardening parameters are determined, based on the ratio of compression index (λ) to swelling index (κ) ($\lambda/\kappa = 10$), where $\lambda = 0.2$ is considered. For the initial yield stress level, 60kPa is assumed. The elements selected for the soil were "C3D8R", a 3-dimensional, 8-node with reduced integration, solid elements. This element supports the three translation degrees of freedom in the x, y and z directions.

Roller

A roller with a diameter of 1.2m is used. For low rolling speed, the rotary inertia of the roller is not

considered in the model. The roller is simulated using analytical rigid shell. Analytical rigid surface is chosen for both accuracy and computational performance since analytical surfaces are not discretized in to finite elements [8]. A cylindrical shell with edge fillet of radius 0.07m is used to avoid numerical problems arising in the algorithm used to model contact surface between the roller and the soil.

Roller-Soil Interaction

The analytical surface of the roller is constrained to the reference point. An angular velocity of 1.85 rad/sec is applied on the reference point. Since the soil model used in this study is rate-independent, the rolling speed has not influence on the compaction process. The roller is modeled as an analytical rigid body and it is non-deformable in the analysis. A surface-to-surface contact is chosen and a penalty contact method is used in Abaqus/Explicit.

Two surfaces are defined to connect the roller surface. The friction coefficient between the roller and the soil surface is roughly approximated from the friction angle of the soil, i.e. $f = tan(\phi)$. To be more realistic, a slightly lower value of friction coefficient than the one computed from the friction angle is used. This is to account the fact that rolling friction is lower than sliding or static friction. For $\phi < 15^0$, a friction coefficient of 0.3 is considered to ensure rolling of the roller on the soil surface.

FEM RESULTS AND DISCUSSIONS

Figure 4 shows the result from a single roller pass. The density at the instance of roller loading is computed from the total volume change i.e. both the elastic and plastic volume change in the soil. After the roller is passed, the density is computed only from the plastic volume change. The elastic volumetric change recovers during unloading. The density profile for different weight of rollers is presented in Fig. 5. The relative density (RD) in this context is the density normalized by the maximum density. The stiffness of the soil in the analysis is 50MPa and the Mohr-Coulomb parameters are $c = 40\text{kPa}$ and $\phi = 20^0$. It is evident that the effective compaction depth increases as the weight of the roller increases.

Lift Height

During compaction of fine grained soils, the number of passes needed to achieve the desired compaction depends on the lift thickness, the contact pressure and soil moisture content. So, the depth of the soil layer (lift height) is an important factor that affects compaction cost and machine performance. In addition, the interaction between the soil and the roller affects the compaction efficiency.

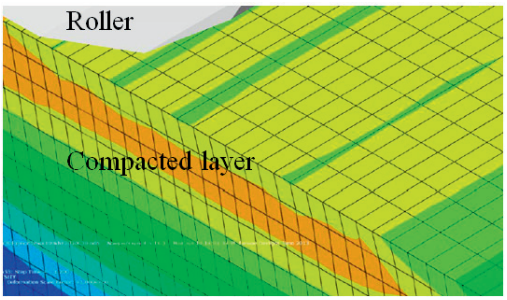

Fig. 4 View of the compaction profile.

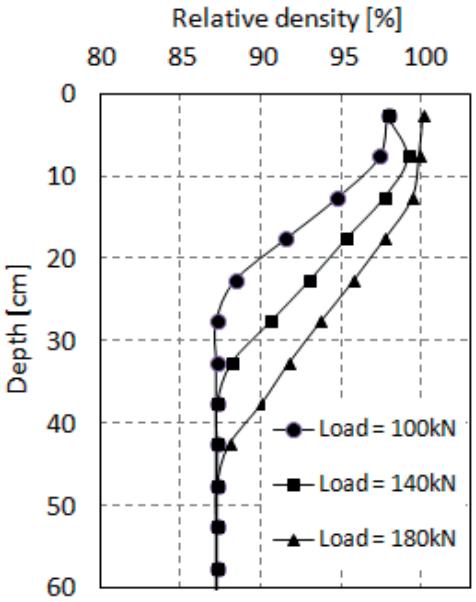

Fig. 5 Compaction density profile for different weight of roller.

Different road agencies have their own specification for the lift height. When different compacting equipment is available in the field, economical compacting effort can be carried out by proper planning. Figure 6 shows the principle of optimization techniques of the lift height for the minimum allowable relative density. The effect of friction angle on effective compaction depth for a roller weight of 10tonn is shown in Figs. 7 and 8. In the model, the cohesion value of the soil is 15kPa and the value of friction angle is varied.

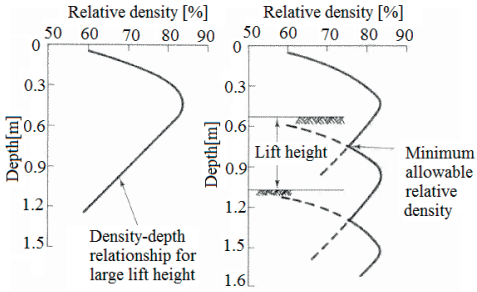

Fig. 6 Principle of an approximate method for determining lift height to achieve a minimum compacted relative density [2].

A critical height is noted at a depth of 0.3m above which soils with low friction angle are compacted to a lesser extent. The highest density is obtained for moderate friction angle and the density closer to the surface of compaction reduces for higher friction angle, possibly due to the effect of dilation. Dilation in soils is associated with increase in volume which consequently reduces the density.

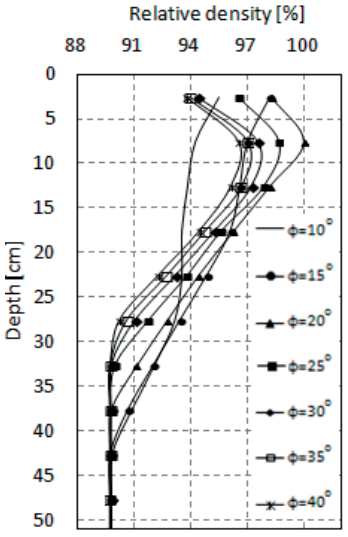

Fig. 7 The effect of friction angle on soil compaction

When the depth of compaction increases, there is no significant change for low friction angle since the compaction depth is controlled by cohesion. At higher values of friction angle, the change in effective compaction depth is small as the soil becomes strong enough and additional compaction effort is required.

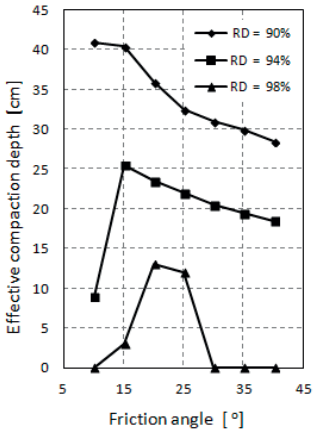

Fig. 8 Effective compaction depth at different relative densities based on friction angle.

The relationship between the relative density and cohesion for specific depths in the soil is presented in Figs. 9 and 10. In this case, the value of friction angle is kept constant ($\phi = 20^o$) and the cohesion is varied. The compacted density appears to be independent of the cohesion of the soil in the top 0,1m for high cohesion values. As the depth increases, the effect of cohesion is clearly shown. For the same load, the effective depth of compaction for highly cohesive soils is very limited and it increases as the cohesion decreases.

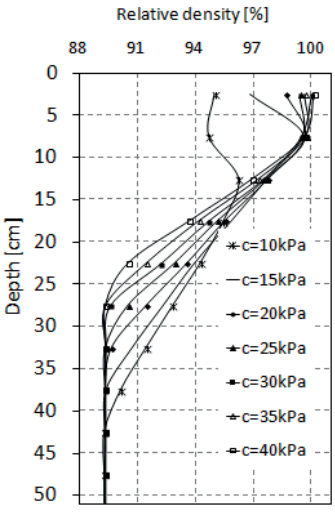

Fig. 9 The effect of cohesion on compaction.

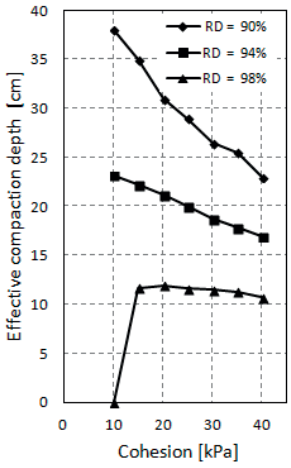

Fig. 10 Effective compaction depth at different relative densities based on cohesion.

CONCLUSION

The study presented in this paper is mainly for smooth wheel rollers. These types of rollers are commonly used when adequate compaction is obtained under relatively low pressure. The effect of soil strength parameters during the compaction process can be used as an input to optimize the compaction depth. The rule of thumb in practice is to use a specified lift height (the same thickness for a range of fine grained soils). Though the general understanding of soil parameters on the response of soil is well known, the quantitative understanding is yet to be investigated.

The numerical investigation shows that soil cohesion highly affects the effective compaction depth. Depending on the amount of stress induced from the roller and the relative density required, the lift height can be chosen as a function of the strength parameters. Based on the knowledge of the friction angle and cohesion of fine grained soils, the rolling strategy can be adjusted and the compaction practice can be improved.

ACKNOWLEDGEMENTS

This research is conducted at the Norwegian University of Science and Technology with the research fund support from the Norwegian Public Roads Administration.

REFERENCES

[1] Proctor, RR, Fundamental principles of soil compaction. Engineering News-Record, Vol.111, No.9, 1933, pp. 286-289.

[2] Holtz RD, and Kovacs WD, “Compaction”, An introduction to geotechnical engineering, Prentice-Hall, Inc.,1981, pp.109-165.

[3] Briaud JL, Seo J, Intelligent Compaction: Overview and Research needs, Texas A&M University, 2003, pp. 1-84.

[4] NPRA, Handbook 018: Road Design and Construction Guidelines (in Norwegian), Norwegian Public Roads Administration, 2011.

[5] Xia K., Masud A, You Z, A large deformation finite element formulation for subgrade soil compaction, Pavements and Materials, 2008, pp. 122-130.

[6] Chiroux RC, et al., Three-dimensional finite element analysis of soil interaction with a rigid wheel. Applied Mathematics and Computation, Vol. 162 ,No.2, 2005. pp. 707-722.

[7] Hambleton JP, Drescher A, Development of improved test rolling methods for roadway embankment construction. 2008, Minnesota Department of Transportation.

[8] Abaqus FEA, Simulia, Dassault Systèmes, 2011

[9] Drucker DC, Prager W, Soil mechanics and plastic analysis for limit design. Quarterly of Applied Mathematics, Vol.10,No.2,1952. pp. 157-165.

[10] Neto EDS, Peric D, Own DRJ, “Advanced Plasticity Models”, Computational Methods for Plasticity: Theory and Applications,John Wiley & Sons Ltd,2008, pp. 403-433.

[11] Hügel, H.M., S. Henke, and S. Kinzler, High-performance Abaqus simulations in soil mechanics, in Abaqus Users’ Conference. 2008.

[12] Kelm M. and Grabe J, Numerical simulation of the compaction of granular soils with vibratory rollers, in Cyclic Behavior of Soils and Liquefaction Phenomena, Taylor & Francis Group, 2004, pp. 661-664.

[13] Chen WF and Mizuno E, Nonlinear Analysis in Soil Mechanics - Theory and Implementation. Elsevier. 1990.

[14] Han LH, et al., A modified Drucker-Prager Cap model for die compaction simulation of pharmaceutical powders. International Journal of Solids and Structures, Vol.45, No.10, 2008, pp. 3088-3106.